

IDEA League

MASTER OF SCIENCE IN APPLIED EARTH SCIENCES



Delft University of Technology

MASTER OF SCIENCE IN CIVIL ENGINEERING

RESEARCH THESIS

Monitoring Backward Erosion Piping with Self-Potential Geophysics

Joost H. N. Gevaert

November 28, 2019

Monitoring Backward Erosion Piping with Self-Potential Geophysics

MASTER OF SCIENCE THESIS

for the degree of Master of Science in Applied Earth Sciences
and for the degree of Master of Science in Civil Engineering at
Delft University of Technology

by

Joost H. N. Gevaert

November 28, 2019



Delft University of Technology

Copyright © 2019 by IDEA League Joint Master's in Applied Earth Sciences:

Delft University of Technology

All rights reserved.

No part of the material protected by this copyright notice may be reproduced or utilized in any form or by any means, electronic or mechanical, including photocopying or by any information storage and retrieval system, without permission from this publisher.

Printed in The Netherlands

IDEA LEAGUE
JOINT MASTER'S IN APPLIED EARTH SCIENCES

Delft University of Technology, The Netherlands
ETH Zürich, Switzerland
RWTH Aachen, Germany

MASTER'S IN CIVIL ENGINEERING

Delft University of Technology, The Netherlands

Dated: *November 28, 2019*

Committee Members:

Prof. Dr. Ir. Evert C. Slob

Prof. Dr. Cristina Jommi

Dr. Ir. Dominique Ngan-Tillard

Prof. Dr. Florian Wellmann

Abstract

Backward erosion piping is a dike failure mechanism. It is the internal erosion process by which sand is eroded away from underneath a dike or levee by seepage flow. This erosion process progresses in the direction opposite to the direction of seepage flow and forms a small pipe directly beneath the dike. As erosion continues, this process can lead to dike failure. During this erosion process, the groundwater flow pattern is subject to continuous change, due to the growth of the pipe. Self-potential (SP) monitoring is sensitive to changes in the groundwater flow pattern, because of the electrokinetic coupling between fluid flow and the streaming potential. The SP field due to flow underneath a test dike was modeled with a FreeCAD → Gmsh → pyGIMLi workflow. This workflow can also be used to effectively resolve a wide range of standard and customizable geophysical modeling and inversion tasks. After modeling, field experiments were conducted, on the same test dike, to further assess the possibilities and limitations of SP monitoring to track the progress of backward erosion piping. Given that it is essential to have an accurate resistivity model in order to find the location of the SP source, an integrated electrical resistivity tomography (ERT) and SP monitoring system was designed. The electrodes used in this monitoring system were polarizable stainless steel stakes. The reliability of polarizable electrodes was greatly overestimated, as they turned out to give unstable SP measurements. The reason for the inferior reliability of polarizable compared to non-polarizable electrodes, was found through extensive literature research. The reason being that the largest potential in any electrode originates from the contact between the metal and the electrolytes in solution. The metal of polarizable electrodes is in direct contact with the electrolytes in the soil, which have variable concentrations. Therefore, the potential measured fluctuates together with the concentration of soil electrolytes in contact with the metal. The metal of non-polarizable electrodes, on the other hand, is in contact with a solution of its own salt, which has a constant concentration. Finally, piping is not expected to be measurable with SP monitoring, before a large sand boil is visible in the field. Once a positive SP anomaly develops at the sand boil, changes in the SP field due to the growth of the pipe are expected to be too small relative to the SP anomaly associated with water flow through the sand boil. Even though an integrated ERT and SP monitoring system is known to provide useful information about the hydrology of a dike, such a system is not sensitive enough to be able to monitor the development of a backward erosion pipe.

Table of Contents

Abstract	v
1 Introduction	1
2 Research Outline	3
2-1 Problem description	3
2-2 Proposed monitoring system	5
3 Theoretical Background	7
3-1 Backward Erosion Piping	7
3-1-1 Context	7
3-1-2 Backward erosion piping: the process	8
Prerequisites	9
Phase 1: seepage	9
Phase 2: backward erosion	9
Phase 3: widening of the pipe	10
Phase 4: failure	11
3-1-3 Piping in the field	11
3-1-4 Piping models	12
3-1-5 Pipe geometry and flow regime	13
3-2 Self-Potential	14
3-2-1 Literature	15
3-2-2 Streaming Potential in a microchannel	17
3-2-3 Streaming potential	20
3-2-4 Polarizable and non-polarizable electrodes	22

4	Modeling	25
4-1	Methodology	25
4-1-1	Software	25
4-1-2	Simulations	26
4-2	Results	29
4-2-1	Mesh refinement study	29
4-2-2	Influence of resistivity on SP	32
4-2-3	Influence of upstream head on SP	33
4-2-4	Influence of pipe length on SP	33
4-3	Discussion and Recommendations	35
5	Field Experiments	39
5-1	Description of the Test Site	39
5-2	Methodology	41
5-2-1	Piping experiment	41
5-2-2	Self-potential	41
	Polarizable and non-polarizable electrodes	42
	Electrical resistivity tomography	44
	Preliminary fieldwork	46
	SP monitoring during piping experiment	47
5-3	Results	48
5-3-1	Piping experiment	48
5-3-2	Self-potential	49
	Electrical resistivity tomography	49
	Preliminary fieldwork	51
	SP monitoring during piping experiment	55
	Environmental impact of copper(II) sulfate	59
5-4	Discussion and recommendations	60
6	Conclusions and recommendations	63
	References	65
A	Complementary figures and tables	69
A-1	Theoretical background	69
A-2	Fieldwork	70
B	Copper(II) sulfate environmental impact calculations	77
C	FreeCAD; Gmsh; pyGIMLi workflow	79
C-1	FreeCAD	80
C-2	Gmsh	81
C-3	pyGIMLi and pyBERT	83

Chapter 1

Introduction

When a human's heart is beating irregularly, an electrocardiogram is made in a hospital, in order to assess what could be the cause of the cardiac rhythm disturbance. Similarly, self-potential (SP) geophysics can be used on dikes and levees to assess groundwater flow patterns and to find leaks in dikes. Both electrocardiography and SP monitoring are based on the same measurement principles.

In electrocardiography, electrical potential is measured on the skin at several places around the heart. The electrical potential on the torso should change regularly every heartbeat as a consequence of de- and repolarization of the cardiac nerves and muscles. Abnormalities in the electrocardiogram therefore contain information about heart diseases, such as cardiac rhythm disturbances.

In self-potential geophysics on dikes and levees, the electrical potential is measured on the surface of the dike. This electrical potential occurs naturally, hence its name self-potential. It originates from the electrokinetic coupling between groundwater flow and the electrical potential. Simply put, groundwater transports slightly more positive ions than negative ions. This net transport of positive charge acts as an electric current, which induces an electrical potential field, that can be measured at the surface when strong enough. Hence, the self-potential field contains information about the groundwater flow and therefore also about leaks in dikes.

Backward erosion piping is an internal erosion process, by which sand is eroded away from underneath a dike or levee by seepage flow. This erosion process progresses in the direction opposite to the direction of seepage flow and forms a small pipe directly beneath the dike. Hence its name backward erosion piping. As erosion continues, this process can lead to dike failure. During this erosion process, the groundwater flow pattern is subject to continuous change, due to the growth of the pipe. The continuous change in the groundwater flow pattern during piping was the motivation for investigating how SP geophysics could aid in monitoring backward erosion piping.

This master thesis starts with the research outline in [Chapter 2](#). In that chapter, backward piping erosion and self-potential monitoring are briefly introduced. Also, the principal idea behind applying time-lapse self-potential measurements to monitor backward erosion piping is explained. [Chapter 3](#) describes the theoretical background of both phenomena in greater detail and an intuitive example of self-potential in a single microchannel is given. The last section of [Chapter 3](#) then gives a solid, literature based, justification for using non-polarizable electrodes, instead of polarizable electrodes, for self-potential measurements. Subsequently, [Chapter 4](#) describes how the self-potential was modeled on test dike. The test dike is a small dike built for large scale backward erosion piping experiments. [Chapter 5](#) describes the methodology and results of self-potential monitoring on the test dike. Both the modeling and field experiment chapters are concluded with a discussion and recommendations section. The final chapter of this thesis sums up the conclusions and recommendations.

Chapter 2

Research Outline

In this chapter backward erosion piping is shortly described, along with how it can be prevented, how it can be detected and what can be done against it when it is detected in an early stage. Afterwards follows an explanation of what a monitoring system would provide and the basic principle of the proposed monitoring system, which is based on measuring self-potentials. More detailed descriptions of backward erosion piping and the self-potential method are given in [Chapter 3](#).

2-1 Problem description

”De Veiligheid van Nederland in Kaart” ([VNK, 2014](#)), or in English: mapping the safety of the Netherlands, is a report about flood risk in the Netherlands. Along large stretches of dike, piping is the dominant failure mode. [Figure 2-1](#) is a schematic representation of the process of backward erosion piping. Phase 1 starts when the low permeability blanket layer on top of the sand ruptures. This rupture can be formed by uplift due to an increase in water level on the upstream side of the dike. The rupture then acts as a preferential flow path in the impermeable blanket layer. Consequently water starts seeping from the river, through the sand and up through the rupture, i.e. exit hole.

When the flow velocities around the exit hole are high, sand is dragged along with the water, forming a sand boil, i.e. a small sand volcano, around the exit hole. This is the start of phase 2: backward erosion. At first the sand is eroded away close to the exit hole and a small cavity forms directly underneath the blanket layer. Subsequently this cavity grows larger and larger as more and more sand is eroded away. If the local head gradient stays high enough, this cavity will eventually grow into the direction of the river, forming a pipe. Finally the pipe will grow to connect the river directly with the hinterland. At that point phase 3 is reached. The complete pipe means low flow resistance for the water. Therefore the eroding power of the water increases, causing the pipe to widen. This is a self-perpetuating process that can eventually lead to dike failure and finally to a dike breach.

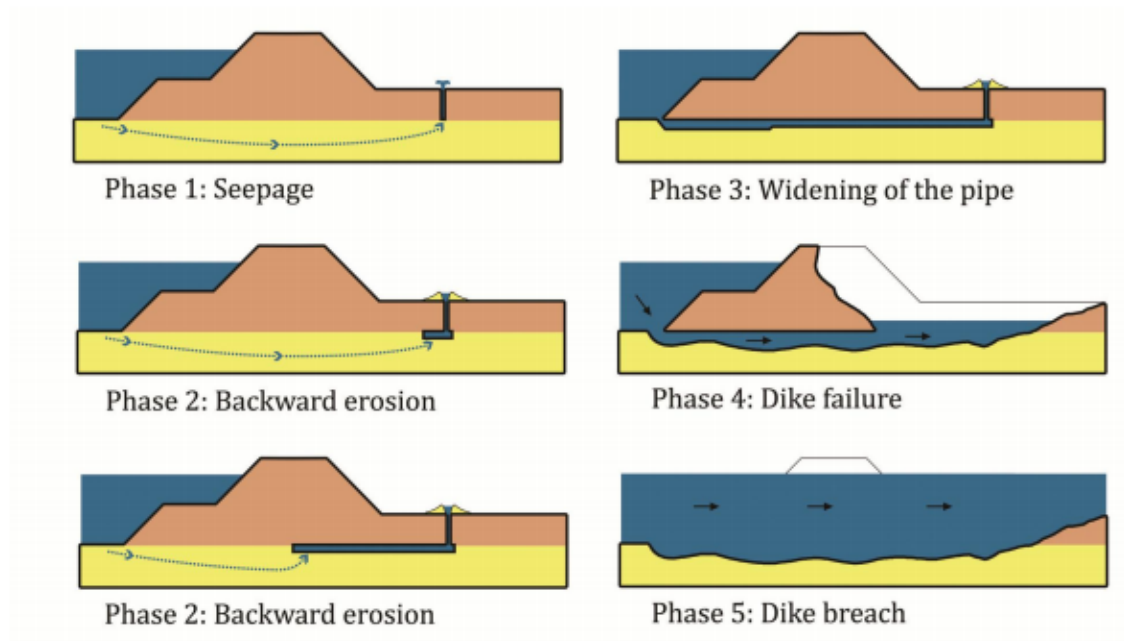


Figure 2-1: Schematic presentation of backward erosion process, leading to failure. The yellow layer is a permeable sand layer, the brown cover layer and dike on top are made of an impermeable, cohesive material mostly clay. Source: [Van Beek \(2015\)](#)

The initiation of backward erosion piping is most commonly prevented in either of the following two ways:

1. Load the cover blanket to prevent it from rupturing.
2. Install some type of barrier.

The extra load is mostly applied by simply putting a sand berm in place against the dike, on top of the impermeable cover blanket. The barrier can either be an impermeable barrier, such as a sheet pile wall. Or a permeable barrier such as a vertical geotextile or a course sand barrier, which does let water through but prevents further sand erosion once the barrier is reached ([Koelewijn et al., 2014](#)).

In case piping did initiate, it can be recognized in the field as a sand boil. At this point further erosion of sand can be prevented by building a ring dam around the sand boil. Therefore the dikes are patrolled during high water events to locate sand boils and adequate action is taken when spotted. The ring dam is usually constructed from sand bags and serves the purpose of reducing the head difference across the dike. This, in turn reduces the head gradient at the tip of the pipe, thereby preventing further erosion. Note that water flow is possible without sand transport. Furthermore note that the erosion process can also come to a standstill naturally, without building a ring dam around the exit hole.

Putting extra load on the cover blanket, or installing sheet pile walls everywhere where there is a risk of piping, is not an option due to the high costs. Additionally, when only a small of sand is eroded away from underneath the cover layer and the backward erosion process comes to a stand still, this does not immediately pose a threat to the integrity of the dike. Moreover the pipe does not necessarily grow straight in the direction of the river. Consequently sand

can be eroded away from underneath the cover layer, also without posing an immediate threat to the integrity of the dike.

Pol, Kanning, and Jonkman (2019) observed pipe growth rates of approximately 8 m/day during recent large scale piping experiments. This growth rate matches growth rates in laboratory experiments and implies that it would take a week for a pipe to fully progress underneath a dike with a 50 m seepage length. Therefore, if widely applicable, the temporal aspects of piping would have significant impact on dike safety assessment, emergency response planning and prioritization of monitoring along dike sections that are known to be critical.

Concluding, there is great interest in monitoring backward erosion piping. The following questions still remain nowadays:

1. When does piping initiate?
2. In what direction is the pipe growing? In other words, where is the sand coming from?
3. How fast is the pipe growing?
4. Do pipes reopen in consecutive high water events? And if so, how quickly do they reopen and continue to grow further?

Being able to answer these questions would greatly aid in being able to respond quickly during high water events, assessing the dike safety during as well as after a high water event and help to get a better understanding of backward erosion piping. On top of that the effectiveness of permeable barriers could also be studied more accurately.

2-2 Proposed monitoring system

The proposed monitoring system makes use of spontaneous- or self-potentials. These are electrical potentials that occur in the ground naturally. Many subsurface processes can be the source of this naturally occurring potential. One of these is the streaming current. Streaming currents exist because water that flows through a porous medium drags along more positive ions, i.e. cations than negative ions, i.e. anions. The excess of positive charge in the pore water is caused by negative charge on the grain surface. The negatively charged grain surface attracts positive ions that form a so-called electrical double layer. There is a net surplus of positive ions in this double layer, that is dragged along with the pore water as it flows through a porous medium. The flow of positive charge is called the streaming current and acts as a current source. The current source is in turn directly related to the electrical potential through the electrical conductivity, as described by Ohm's law. In summary, the groundwater flow field is related to the electrical potential. Thus, measuring the electrical potential at the earth's surface gives information about the groundwater flow field.

In backward erosion piping the groundwater flow field is subject to continuous change, as schematized in Figure 2-2. (a) represents the base situation, where water slowly flows from the river, underneath the levee, i.e. dike, to the ditch. (b) represents phase 1, the cover blanket was ruptured and seepage started. Flow rates are considerably higher in situation (b) compared to (a). Phase 2: backward erosion developed a growing pipe, see (c). (d) represents phase 3, at this stage most flow occurs through the pipe that broke through to the river.

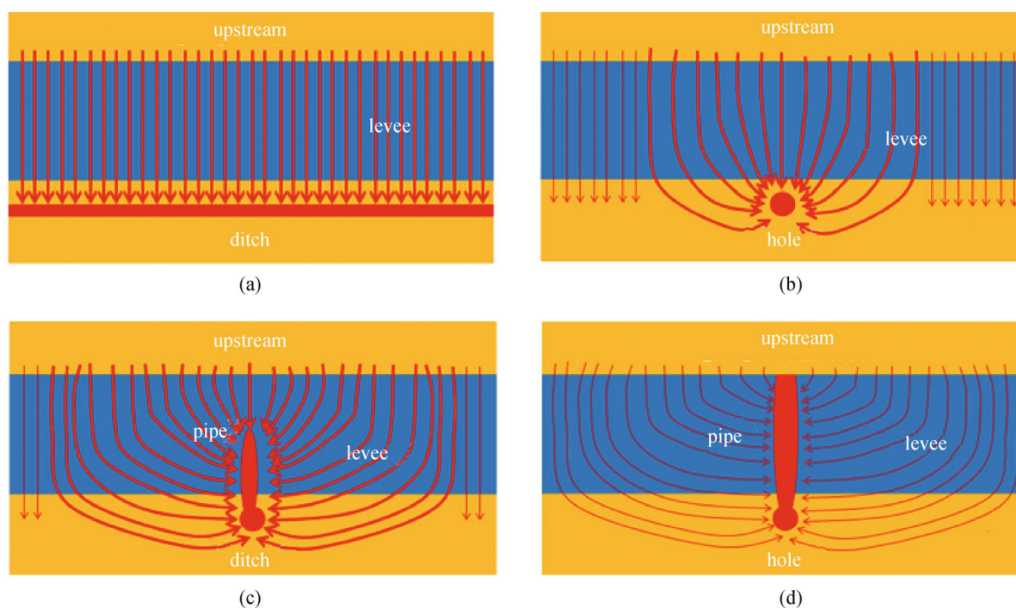


Figure 2-2: Schematic representation of the groundwater flow field during backward erosion piping. (a) base situation, no piping, water slowly flows towards the ditch. (b) Phase 1: seepage. (c) Phase 2: backward erosion. (d) Phase 3: the pipe broke through and is widening. Source: [Vandenboer et al. \(2014\)](#)

Concluding, the groundwater flow field is subject to continuous change at the initiation and during the process of backward erosion piping. Due to the phenomenon of streaming potentials the electrical potential changes together with the groundwater flow field. Therefore it was proposed to investigate if the process of backward erosion piping can be monitored by doing time-lapse measurements of the self-potential at the surface.

In order to determine correctly where the streaming current density originated from and hence where the pipe was growing towards, the electrical resistivity of the subsurface had to be determined as well. Therefore the proposed monitoring system consisted of a combination of electrical resistivity tomography (ERT) and self-potential monitoring. To make the system as simple as possible it was investigated if it was possible to use the same instrument and electrodes for both ERT and SP measurements. When integrated into a long term monitoring system the SP would be measured continuously and an ERT survey would be performed from time to time, to investigate changes in medium resistivity.

The research question of this master thesis is:

What are the possibilities and limitations of monitoring backward erosion piping with time-lapse measurements of the self-potential at the surface of a dike?

With the following sub-questions:

1. What is the expected SP signal during piping based on modeling?
2. What is the sensitivity of the proposed monitoring system?
3. Are there limitations to using the same instrument and electrodes for measuring both ERT and SP?

Theoretical Background

Chapter 2 gave a short overview of how a self-potential monitoring system could aid in tracking backward erosion piping. As well as a short description of backward erosion piping and self-potentials. This chapter goes more in depth about the theoretical background of both phenomena.

3-1 Backward Erosion Piping

Backward erosion piping is the internal erosion process by which sand is eroded away from underneath a dike or levee by seepage flow. This erosion process progresses in the direction opposite to the direction of seepage flow and forms a small pipe directly beneath the dike. Hence its name backward erosion piping, or piping for short. In this section the most important aspects of this phenomenon are described from the perspective of a coastal, deltaic environment.

3-1-1 Context

”De Veiligheid van Nederland in Kaart” (VNK, 2014), or in English: mapping the safety of the Netherlands, is a report about flood risk in the Netherlands. Four important failure mechanisms were identified, see [Figure 3-1](#).

1. Overtopping, waves or overflow cause erosion of the downstream slope.
2. Sliding failure of the downstream slope.
3. Erosion of the upstream slope protection due to high wave loads.
4. Backward erosion piping.

Overtopping can occur anywhere, when a dike is not high enough. Erosion of the upstream slope occurs where there are high waves, such as along the coast. Sliding failure of the downstream slope is the dominant mechanism when the dike is built on weak soil, such as

peat or soft clay. Backward erosion piping is the dominant failure mechanism when a well sorted sand is overlain by a cohesive cover. The probabilities of dike failure due to backward erosion piping turned out unexpectedly high. These failure probabilities were calculated using the J. B. Sellmeijer (1988) model. Van Beek (2015) and references therein write that the failure probabilities calculated in VNK (2014) depict a realistic dike safety and that backward erosion piping is therefore the dominant failure mechanism for many dikes in the Netherlands. Moreover, piping is not only a risk emerging from models and calculations. The most recent, well documented dike breaches due to backward erosion piping in the Netherlands occurred at the Zalk, 08-01-1926; Tholen, 30-12-1894; Nieuwkuijk, 28-12-1880 (Vrijling et al., 2010). Piping is not only a risk in the Netherlands. Within the last three decades, several dike breaches along the Yangtze and Nenjiang rivers in China and along the Mississippi river in Louisiana, USA were also caused by backward erosion piping (Van Beek, 2015).

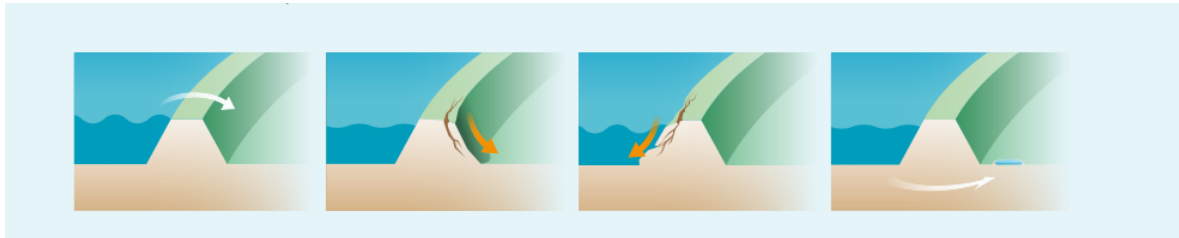


Figure 3-1: Failure mechanisms investigated in VNK (2014) for dikes. From left to right: overtopping, slide failure of the downstream slope, erosion of the slope protection, backward erosion piping.

3-1-2 Backward erosion piping: the process

The processes involved in backward erosion piping are described exhaustively in the dissertation of Van Beek (2015). These processes were described on the basis of observations from lab- and field-scale experiments. The results of the experiments aided in getting a better understanding of backward erosion piping and how to predict it.

Piping is a type of internal erosion. In total there are four internal erosion mechanisms:

1. Backward erosion piping
2. Suffusion: occurs in gap-graded soils. The small grains are eroded from between the coarser matrix.
3. Contact erosion: water that seeps along the surface between a coarse and a fine layer, erodes the finer particles into the coarse layer.
4. Concentrated leak erosion: material in an already existing crack is eroded away.

In coastal and deltaic environments soils are well sorted, i.e. uniformly-graded and therefore suffusion and contact erosion are not likely to cause problems. Concentrated leak erosion could occur. However other failure mechanisms, such as sliding failure of the downstream slope or backward erosion pose a larger threat. Concentrated leak erosion is more notorious for causing failure of embankment dams, where the head difference across the water retaining structure is higher than in deltaic areas. Thus, in coastal and deltaic environments backward erosion

pipng is the only type of internal erosion that would be the dominant failure mechanism (Van Beek, 2015).

Prerequisites

In order for backward erosion piping to initiate and progress to failure, there are a four environmental prerequisites that need to be satisfied:

1. There must be a sand layer underneath the dike and the hinterland, that is connected to the water in the river, see [Figure 2-1](#).
2. The permeable layer must be overlain by an impermeable, cohesive layer that does not collapse into the pipe once it starts forming.
3. There must be an unfiltered exit in the impermeable blanket layer that allows water to seep downstream through the permeable layer.
4. The water level on the upstream side needs to exceed a certain critical level to initiate piping and cause the pipe to progress all the way upstream. The critical head can be estimated using the Sellmeijer model (J. B. Sellmeijer, 1988).

The shallow subsurface near rivers is mostly dominated by fluvial deposits, which are laterally variable in nature. Therefore, the aforementioned piping prerequisite 1 is not a given. An old river channel could cross the bedding of a river in one place, making that location sensitive to backward erosion piping. However, a few hundred meters away, the old river channel is not present directly underneath the current river bed, and thus piping cannot occur there.

Phase 1: seepage

Backward erosion piping comprises four phases, see [Figure 2-1](#); 1 seepage; 2 backward erosion; 3 widening of the pipe and 4 dike failure. In order for phase 1: seepage to start, the blanket layer has to rupture, such that an unfiltered exit forms, thereby fulfilling prerequisite 3. Such a rupture can be formed due to uplift during a high water event.

Phase 2: backward erosion

[Figure 3-2](#) gives a schematic representation of the processes that must occur simultaneously in order for the pipe to grow. The backward erosion process can be split into two stages; (a) a regressive or equilibrium stage and (b) a progressive stage. For both stages, the head gradient must reach a certain critical value at the tip of the pipe, such that the sand fluidizes. Then the sand can come into suspension and can be transported. At the beginning, this means that the sand will be pushed into the exit hole. At this point, a steady state situation can occur. In such a situation only water flows out. When the head upstream increases, the higher flow velocity will push sand out of the exit hole. Hence forming a sand boil and a small cavity underneath the cover blanket that develops into a pipe.

Equilibrium can occur again when the pipe is short in length. At short pipe lengths, the local head gradient decreases when the pipe grows, because groundwater flow converges to a larger and larger pipe. In that case, the head upstream needs to increase again for backward

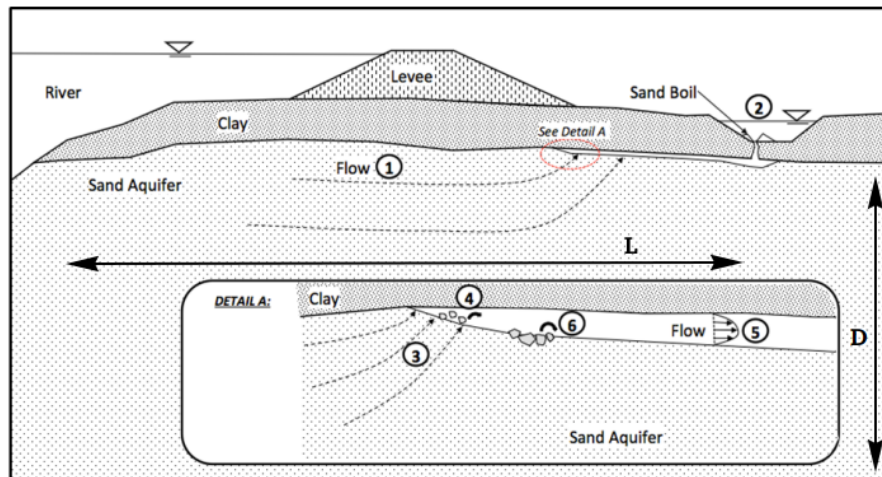


Figure 3-2: Processes involved in backward erosion piping: 1 seepage; 2 or (H) head difference between river and hinterland; 3 convergence of flow towards the pipe, causing a high local head gradient; 4 sand fluidization and primary erosion; 5 laminar flow conditions that allow for; 6 sand transport and secondary erosion; (L) seepage length; (D) thickness of sand layer. Source: Robbins and van Beek (2015)

erosion to continue. However, once the pipe grows to $1/3$ to $1/2$ of the seepage length, the local head gradient at the pipe tip will start increasing as the pipe grows further towards the river. This pipe length is the so-called critical seepage length. When the critical pipe length is reached the backward erosion progress transitions from (a) the equilibrium stage to (b) the progressive stage.

The head at which the pipe grows to its critical length is called the critical head. The critical head depends on many soil and geometrical parameters and therefore differs from dike to dike (see below). The situation in Figure 3-2 is in the equilibrium stage, because the critical pipe length is not $1/3$ of the seepage length. However, if the head as depicted exceeds the critical head, the pipe will grow nonetheless.

The erosion inside the pipe can be split up into two categories. Primary erosion, which occurs at the tip of the pipe, as indicated with number 4 in Figure 3-2, and secondary erosion, which occurs behind the tip of the pipe, as indicated with number 6 in Figure 3-2. Primary erosion, at the tip of the pipe, makes the pipe grow longer, or in a different direction. As mentioned above, primary erosion is governed by the local head gradient at the tip of the pipe. Secondary erosion causes the widening and deepening of the pipe behind the tip and is governed by the flow velocity in the pipe. Both processes have to occur simultaneously. As the pipe grows, the sand needs to be transported away and the pipe has to grow wider and deeper such that the pipe resistance reduces and the gradient at the tip stays high enough for primary erosion.

Phase 3: widening of the pipe

As soon as the pipe connects to the river, the flow resistance in the pipe suddenly decreases greatly, leading to a sudden increase in flow that erodes sand at the upstream inlet. The eroded sand then clogs the pipe and is removed through a new process of backward erosion.

This process then repeats itself and thereby widening the pipe in the same direction as the direction of flow. When the pipe is still widening, the flow and sand transport rates do not increase significantly compared to flow and transport rates during phase 2.

Once the pipe widens over its entire length, the flow capacity of the pipe greatly increases. At which point the sand boil turns into a mud fountain. [Van Dam and Beijersbergen \(1981\)](#) reports on such a mud fountain observed at the 1926 dike breach at Zalk. As translated by [Van Beek \(2015\)](#) the report states:

”When we turned round, we saw a man-sized fountain of mud where the boil had been. It soon became clear that no steps would avail and so the fire bell was sounded in all haste and bicycle relays were dispatched to warn the populace in the hinterland.”

Phase 4: failure

The drastic increase in flow rate in the pipe leads to further scour of the sand and cover blanket. At some point causing cracks to form in the dike body. Subsequently, two things can happen. 1 the dike could fail completely. The cracks in the dike lead to loss of stability, causing sliding failure. Alternatively, the dike could fail when the dike settles into the large pipe and the remaining dike is washed away by a combination of overtopping and internal erosion. 2 the dike could remain in place when the dike settles into the pipe and subsequently does not fail due to overtopping. ([Van Beek, 2015](#)).

3-1-3 Piping in the field

During high water events the dikes are patrolled, in the Netherlands by volunteers of ”het dijkleger”, literally translated to English: the dike army. They inspect the dike for signs of all failure modes (see [Figure 3-1](#)) and alarm dike board when necessary. As mentioned above piping can be first observed in the field as a sand boil. [Figure 3-3](#) shows two examples of sand boils. Often sand boils form underwater, such as in a ditch (b), where the cover blanket is thinner. Areas that are sensitive to sand boiling are usually known from experience.

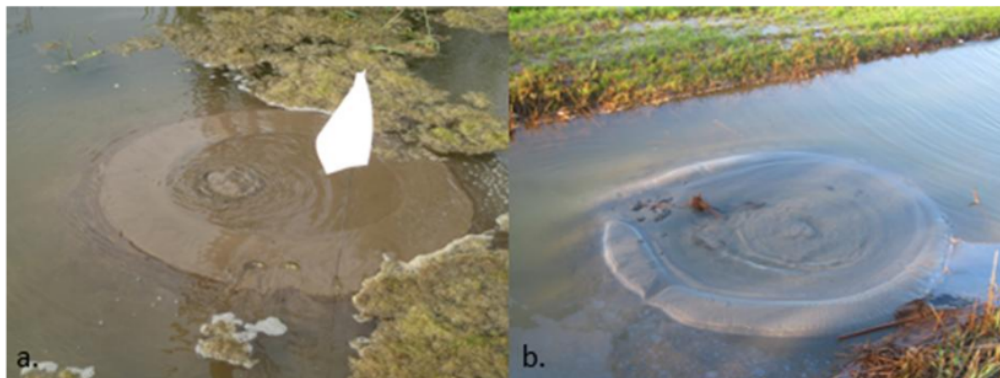


Figure 3-3: Typical sand boils (a) Mississippi river, USA; (b) Waal, Netherlands. Source: [Robbins and van Beek \(2015\)](#)

When a sand boil is located, a ring dam of sand bags is built around the sand boil. [Figure 3-4](#) is a picture of a ring dam around a sand boil along the river Waal in the Netherlands. With the ring dam in place the water level on top of the sand boil raises. Therefore, the head difference across the dike is smaller. If the head difference is reduced enough, the erosion will stop. When the water level in the river goes back to a normal level again, the ring dam can be removed again. Extra load can be applied on the cover blanket or a barrier can be installed in the dike to prevent sand boiling from happening again (see [Chapter 2](#)).



Figure 3-4: Ring dam around a sand boil at the river Waal, Netherlands. A ring dam serves the purpose to decrease the head across the dike and thereby stop further erosion. Source: J.C. Pol

3-1-4 Piping models

Currently, the most advanced model for predicting backward erosion piping is the Sellmeijer model. It is a semi-theoretical model that gives the critical head for a 2D dike or levee, taking geometry and soil parameters of the sand into account. The Sellmeijer model applies to uniform sands. The model was first developed by [J. B. Sellmeijer \(1988\)](#) and was later extended and updated based on lab experiments performed by [Van Beek \(2015\)](#). A form of the Sellmeijer model that is commonly used in the Netherlands is given by:

$$\frac{H_c}{L} = \alpha c \frac{\gamma'_p}{\gamma_w} \tan \theta (0.68 - 0.1 \ln c) \quad \alpha = \left(\frac{D}{L} \right) \frac{\left(\frac{D}{L} \right)^{0.28}}{\left(\frac{D}{L} \right)^{2.8} - 1} \quad (3-1)$$

$$c = \eta \frac{d_{70}}{(\kappa L)^{1/3}}$$

where:

H_c	critical head [m]	γ'_p	submerged unit weight of grains [N/m ³]
L	seepage length [m]	γ_w	unit weight of water [N/m ³]
D	thickness of sand bed [m]	θ	angle of repose [°]
η	White's coefficient [-]	κ	intrinsic permeability [m ²]
d_{70}	70% mass percentile grain diameter [m]		

White's coefficient represents the relative area of the grains over which the shear stress, exerted by the flow of water, is distributed. [Van Beek \(2015\)](#) used a conservative value of 0.25, where values can range up to 0.40. The reader who is familiar with the Sellmeijer model might know the angle of repose as the bedding angle. The use of the word bedding angle was intentionally avoided, given that it is not related to the term bedding from sedimentology.

The thickness of the cover blanket is accounted for in the Sellmeijer model by $H_c - 0.3 \times$ (thickness of cover blanket). The logic behind this is as follows: The rupture in the cover blanket is filled with sand, that was eroded out of the sand layer underneath. This sand inside the exit hole causes a head drop over the length of the hole, that decreases the total head drop by approximately $0.3 \times$ (thickness cover blanket).

Later adaptations of the Sellmeijer model were aimed at including the influence of relative density, sand uniformity and grain angularity. The influence of these additional parameters was derived from lab and large scale experiments and subsequent multi-variate regression analysis ([H. Sellmeijer, de la Cruz, van Beek, & Knoeff, 2011](#)). [Van Beek \(2015\)](#) confirmed the model for 2D geometries with additional lab experiments. In a 2D geometry the exit hole resembles a ditch, rather than a single point. Such a single point exit type, the Sellmeijer model overestimated the critical head by up to a factor 2 in uniform fine sands. On the other hand, variable particle sizes have a positive effect on the critical head measured in lab experiments (see also [Figure 3-5](#)). The nature of fluvial sand deposits ensures a variable particle size, due to sedimentary features such as cross bedding.

3-1-5 Pipe geometry and flow regime

As mentioned before, [Van Beek \(2015\)](#) did many lab experiments to get a better understanding of backward erosion piping. One of the things investigated was the geometry of the pipe. [Figure 3-5](#) shows a top view photo of one of the small scale experiments. It is clear that the pipe does not grow in upstream direction along the shortest path and that a layer of coarser sand can cause the pipe to diverge.

The depth of the pipe was analyzed using a laser. At the exit hole the depth was 1.8 mm and away from the exit hole approximately 1 mm. A few mm before the pipe tip the pipe depth decreases to 0.6 mm and then rapidly decreases to 0 mm. [Bersan, Jommi, Koelewijn, and Simonini \(2013\)](#) modeled a pipe in COMSOL Multiphysics, using a depth of 1.8 mm and a width of 10 mm and assuming a cuboid shape. During full scale experiments [Pol et al. \(2019\)](#) expected similar pipe dimensions, but found that the amount of sand eroded suggested a 70 cm ellipsoid shallow cavity around the exit hole and a pipe depth and width up to 4 times as large.

[Van Beek \(2015\)](#) also determined the flow regime in a pipe, by calculating the Reynolds number (Re [-]) for different pipe cross sections. Reynolds number expresses the ratio between inertial to viscous forces in the Navier-Stokes equation. At low seepage velocities, Reynolds

numbers are small (below 1 in porous media) flow is viscous laminar. Inertial forces can be neglected and Darcy's law applies. As Re goes up, inertial forces can no longer be neglected. At these Re 's the flow regime is called inertial laminar. At even higher Re 's the flow becomes turbulent. In porous media Re has to exceed at least 100 and Re has to be well above 400 in a pipe formed by backward erosion, for flow to become turbulent.

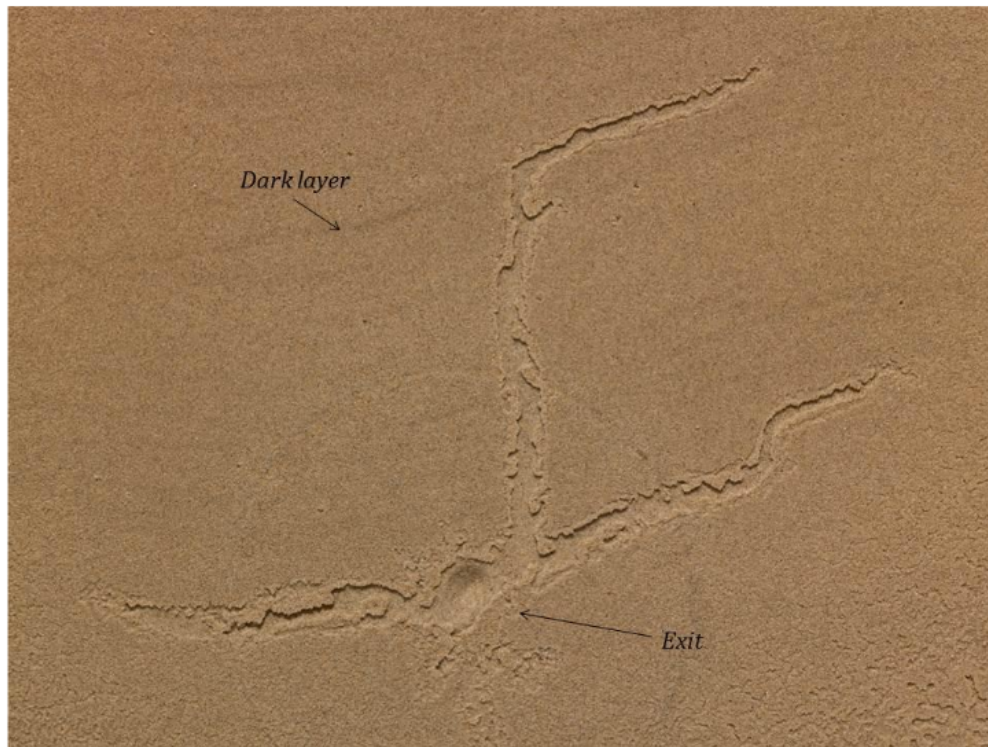


Figure 3-5: Geometry of a pipe formed in a small scale experiment performed by [Van Beek \(2015\)](#). The width of the photo is 30cm and the top is upstream. The pipe is approximately 1.8 mm deep at the exit hole and 1 mm away from the exit. Note how the pipe grew in multiple directions and changed direction when a coarser sand layer was reached, indicated with "dark layer" in the photo.

3-2 Self-Potential

Self-potential is synonymous with spontaneous potential, often abbreviated with SP. SP might also refer to streaming potential, which is a type of self-potential when streaming current is the source of the electrical potential field. However, in this thesis SP stands for self-potential. As the name already suggests, self-potential geophysics belongs to the family of potential field techniques, e.g. gravity and magnetic methods. In an SP survey, the electrical potential is measured in the field with respect to a reference electrode.

The measurement principle in self-potential geophysics is the same as in medical electrographical methods such as electrocardiography (ECG) and electroencephalography (EEG). In electrocardiography, spontaneous electrical potential is measured on the skin at several places around the heart. The electrical potential on the torso should change regularly every

heartbeat as a consequence of de- and repolarization of the cardiac nerves and muscles. Abnormalities in the electrocardiogram therefore contain information about heart diseases, such as cardiac rhythm disturbances. Similarly the potential measured on the scalp in EEG contains information about the electrical activity in the brain. In the same way, measuring the self-potential at the earth's surface or in a borehole gives information about electrical activity in the earth, which indirectly contains information about other processes in the earth, given the coupling between electric, fluid, heat, solute diffusion fluxes and redox processes.

3-2-1 Literature

Minsley (2007, chap. 2) gave a clear and complete description of self-potential phenomena. The following topics were discussed: coupling of electric, hydraulic, chemical and heat fluxes; generation of self-potentials from hydraulic and solute diffusion primary flows as well as self-potentials associated with redox processes; relation between the streaming and conductive current and how the medium resistivity influences this.

Since Sill (1983) it is common practice to describe SP and the secondary electric current as a consequence of primary flows. Where secondary current is the conductive current and the primary flows are hydraulic, heat, chemical and/or other fluxes, which act as electrical current sources through primary flow-electric coupling.

The multiplicity of self-potential sources gives rise to a wide range of SP applications. Many of its early applications concerned mineral exploration. In SP surveys for mineral exploration, the passively measured potentials are mostly of electrochemical nature, related to redox processes in and around the ore body. SP also finds applications in the characterization and monitoring of volcanic and geothermal systems and was used for delineating coal seam fires. Where the source of the electrical potential field is assumed to be the heat flux or a combination of heat and hydraulic fluxes. Additionally, SP is also applied in fracking, mapping aquifer properties and tracking contaminant plumes or groundwater flow patterns, e.g. in vadose zone hydrology, landslides and earth dams. In most of these cases the hydraulic flux is assumed to be the only source of the measured potential field. (Minsley, 2007; Soueid Ahmed et al., 2019, and references therein). Conversely, the multiplicity of sources can also lead to ambiguity or incorrect interpretation as to what is the source of the measured self-potentials.

Streaming current is the only relevant source of self-potential when tracking groundwater flow patterns in and underneath dikes. Other sources of SP are assumed negligible. Streaming current originates from the viscous drag of excess charge in the diffuse layer of the electrical double layer (EDL). See 3-2-2 for a more elaborate explanation of the EDL and streaming current in a single pore, i.e. microchannel and refer to Section 3-2-3 for a concise derivation of the equations governing streaming current in porous media.

Minsley (2007) showed, on the basis of a few intuitive examples, how the SP field looks for simple geometries. A negative anomaly appears at the source of the flow and a positive anomaly appears at the sink. It was also illustrated that the streaming current is a local current source, that is balanced by the conductive current in the entire domain. Consequently, the lower the electrical resistivity of the domain the lower the self-potential.

Bolève, Crespy, Revil, Janod, and Mattiuzzo (2007) extended the streaming potential formulation to include Reynolds number (Re [-]). Lab experiments showed that the SP decreases

when in the inertial laminar flow regime, so when the Reynolds number becomes higher than 1. Additionally the lab results justified the use of the excess charge in the diffuse layer per unit volume (Q_v [Coulomb/m³]) to quantify the streaming potential coupling coefficient. Instead of using the zeta potential. The lab experiments also showed that the the SP goes down as the fluid salinity goes up. Bolève, Vandemeulebrouck, and Grangeon (2012); Jardani et al. (2007) later formulated and refined an empirical relationship between Q_v and the hydraulic permeability (k [m⁻²]), Equation (3-11). See Figure A-1 for the experimental setup and the regression analysis that form the basis of the empirical relationship.

Bolève, Revil, Janod, Mattiuzzo, and Fry (2009); Jardani et al. (2007) showed how Richards equation for unsaturated flow can be incorporated in the streaming potential formulation, for the application to an infiltration test and for localizing preferential flow paths in dams and embankments respectively. The methodology described by Bolève et al. (2009) is exhaustive, coherent and generally applicable. The proposed methodology consists of the following steps:

1. SP forward modeling based on medium parameters known from dam construction, previous investigations or a well educated guess.
2. SP and electrical resistivity tomography (ERT) surveys.
3. ERT inversion.
4. SP tomography: inversion for streaming current density, using the ERT result as the resistivity model. The SP forward model was taken as an initial guess to overcome the non-uniqueness of potential field methods.
5. Measurement of in-situ permeability, e.g. Lefranc test, slug test, direct push permeameter.
6. Create Q_v model based on k measurements and the $Q_v - k$ empirical relationship, Equation (3-11).
7. Calculation of seepage velocities from the streaming current density and the Q_v model.
8. Quantification of uncertainty in obtained seepage velocities.

A synthetic case study was performed to validate the proposed SP inversion method. A field experiment on a leaking dike along the river Rhône was carried out to verify the methodology. ERT surveys were performed along 2D lines and SP was acquired on a 3D grid. The SP inversion and leakage calculation was performed along a 2D line where the SP anomaly and thus leakage was largest. The resulting seepage velocity distribution showed an outflow at the toe of the dike of 3 liter/s per meter dike (2D) with a relatively large methodological uncertainty of 1 l/s. The found outflow did match however with the outflow observed in the field which ranged from 1 to 10 l/s. As a recommendation, Bolève et al. (2009) suggested doing SP monitoring, rather than SP tomography, because monitoring gives a better signal to noise ratio.

Koelewijn et al. (2014) described piping experiments on the Ijkdijk (meaning "calibration dike"), aimed at examining the effectiveness of controlled drainage, a coarse sand barrier and vertical geotextile as measures to prevent piping. During the tests on the geotextile, Rittgers, Revil, Planes, Mooney, and Koelewijn (2014) combined passive acoustic and self-potential monitoring to image the development of seepage underneath the Ijkdijk. ERT and pressure wave (P-wave) seismic refraction tomography (SRT) were performed, such that the source

location of the passive acoustic and SP signals could be inverted for. The acoustic emission sources were expected to coincide with the flow of water and transport of sand. Therefore, the SP inversion was constrained based on the location of the acoustic emission sources. Here also in order to overcome the non-uniqueness of potential field methods. The measured SP anomaly ranged from -1 mV at the top of the dike to 3 mV where the water came from underneath the dike. These SP anomalies showed up after 100 hours into the test, while prominent sand boils were visible after 90 hours into the test.

In self-potential surveys and monitoring, it is common practice to use so-called non-polarizable electrodes. Most of these electrodes consist of a metallic wire in direct contact with an electrolyte solution of its own salt. The most well known non-polarizable electrode is the silver-silver chloride (Ag-AgCl) electrode, which is used in medical applications and in the lab. For SP measurements in the field, the most commonly used electrodes are the [Petiau \(2000\)](#) lead-lead chloride (Pb-PbCl₂) and copper-copper(II) sulfate (Cu-CuSO₄) electrodes. These electrodes are called non-polarizable, because the metal-electrolyte interface does not polarize when a direct electrical current passes through it. See [Section 3-2-4](#) for a more extensive discussion about polarizable and non-polarizable electrodes.

3-2-2 Streaming Potential in a microchannel

[Figure 3-6](#) shows a schematic representation of a microchannel connected to two reservoirs and a zoom in on the top microchannel wall and electrical double layer (EDL). This setup is commonly used in the lab to determine the zeta potential ([Glawdel & Ren, 2015](#)). There are two methods to measure the zeta potential with this setup. One possibility is by applying an electrical potential difference across the channel and measuring the flow rate, in which case the fluid flow is caused by electro-osmosis. The other relies on applying a pressure difference across the channel and measuring the electrical potential across the channel. The measured potential difference is the streaming potential.

Both of these electrokinetic effects are related to the surface potential of the microchannel. Soil particles get a negative surface charge when they come in contact with water. Thus when the microchannel is seen as a pore, the surface of the pore is negatively charged. The negative surface charge is compensated by an excess of positive charge in the EDL.

Over the years the model that describes the EDL has developed considerably. In many fields of study there consensus to describe the EDL according to the Gouy-Chapman-Stern model ([Glawdel & Ren, 2015](#)). According to this model, the positive ions are strongly bound to the mineral surface in the Stern layer, which extends from the mineral surface to the shear plane. The water and ions in the Stern layer are practically immobile. The potential away from the mineral surface drops linearly from the surface potential (Ψ_s) to the Stern potential (Ψ_d) at the Stern plane, see [Figure 3-6](#). The distance from the mineral surface to the Stern plane is approximately 1 ion radius. Away from the Stern plane the potential decays with 1/distance. The shear plane is the interface between the Stern and diffuse layers. The positive ions within the diffuse layer experience a weaker electrostatic attraction from the surface. Water and ions in the diffuse layer are therefore mobile and the ions are also not exclusively positively charged. There is however still a considerable amount of excess positive charge in the diffuse layer.

The zeta potential and thickness of the diffuse layer depend on several factors, including pH, temperature, surface potential, positive ion concentration and valence. With a higher

valence and concentration of positive ions the zeta potential and diffuse layer thickness go down. Therefore, the diffuse layer thickness go down as the salinity and thus as the fluid conductivity go up.

The excess positive charge in the diffuse layer gives rise to electro-osmosis and streaming current.

- Streaming current: net movement of charge through a porous medium or microchannel, caused by the viscous drag of the excess charge in the diffuse layer under the influence of an externally applied pressure gradient.
- Electro-osmosis: fluid flow through a porous medium or microchannel, due to viscous drag of excess charge in the diffuse layer under the influence of an externally applied electrical field.

In a microchannel both eletrokinetic phenomena are well defined. The Helmholtz-Smoluchowski equation describes the relation between the pressure and electrical potential differences across the microchannel and reads:

$$\Delta\varphi = \frac{\varepsilon_f \zeta}{\mu \sigma_f} \Delta p, \quad (3-2)$$

$$C = \left(\frac{\partial \varphi}{\partial p} \right)_{\mathbf{j}_{tot}=0} = \frac{\varepsilon_f \zeta}{\mu \sigma_f} \quad (3-3)$$

where:

Δp	pressure difference across channel [Pa]	$\Delta\varphi$	streaming potential [V]
ε_f	electric permittivity of the fluid [F/m]	ζ	zeta potential [V]
μ	fluid dynamic viscosity [Pa s]	σ_f	fluid conductivity [S/m]
C	streaming potential coupling coefficient [V/Pa]		

$\mathbf{j}_{tot} = 0$ refers to a total current density of zero A/m². The streaming current and conductive current counter balance each other, as is explained below.

Considering the case as shown in [Figure 3-6](#), in which a pressure difference is applied, a streaming current is generated and the streaming potential is measured. When no pressure gradient is applied yet, both reservoirs and the microchannel as a whole are electrically neutral. In other words, the sum of all charge equals 0. However the water inside the pore contains a net excess of positive charge, such that the negative surface charge of the microchannel is compensated.

Once the pressure is applied, a streaming current is generated in the microchannel. There is a net flow of positive charge from the microchannel into the reservoir on the right and a net flow of positive charge from the reservoir on the left into the microchannel. The difference in amount of charge between the left and right reservoirs can be measured as the streaming potential.

However, at steady state there cannot be a net inflow of positive charge on the right and a net outflow of positive charge on the left. Therefore, the streaming current is compensated by an equal and opposite conductive current. The conductive current flows by means of ionic

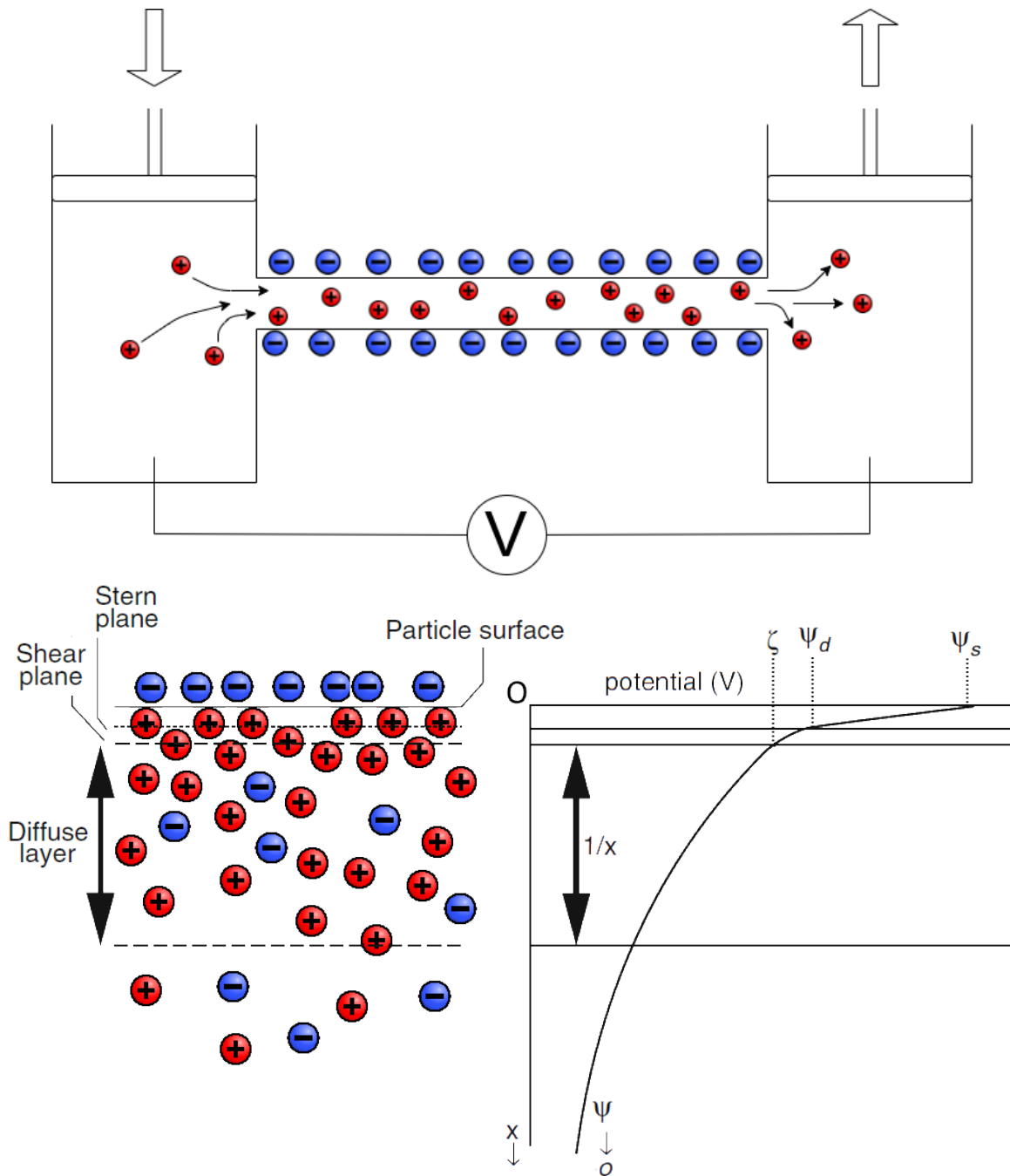


Figure 3-6: Top: microchannel with negative surface charge, connected to two reservoirs. A pressure is applied across the channel to enforce fluid flow, as a consequence a streaming potential is generated. Bottom: a zoom in on the top wall of the microchannel and the EDL. The negative potential of the surface (Ψ_s) is compensated in the Stern and diffuse layers. The potential away from the surface develops linearly to the Stern layer potential (Ψ_d) at the Stern plane. Then decays with $1/\text{distance}$. The zeta potential (ζ) is the potential at the shear plane, the boundary between the Stern and diffuse layers. Adapted from: [Glawdel and Ren \(2015\)](#)

conduction in the Stern layer, diffuse layer and bulk fluid. The conductive current flowing in the diffuse layer hinders fluid flow forced by the pressure difference due to electro-osmosis.

When the pressure gradient across the microchannel is removed, pressure driven fluid flow stops. The conductive current keeps flowing until the original situation is restored. The left and right reservoirs and the microchannel as a whole are electrically neutral again and the streaming potential is zero volt.

The above described phenomena, which give rise to streaming potentials in a microchannel, are largely analogous to what happens when water flows through a porous medium. During piping a negative SP anomaly is expected where the water flows from the river into the sand bed underneath the dike. A positive SP anomaly is expected where the water boils up to the surface. The conductive current is, however, not opposite and equal to the streaming current everywhere. The reason being that the streaming current should be seen as a local current source that coincides with the fluid flow domain. Whereas conductive current can flow in the entire domain, e.g. also far above the capillary fringe, where there is practically no fluid flow. As a consequence the SP measured at the surface heavily depends on the medium resistivity.

Another pitfall of the analogy between a microchannel and a porous medium, is that it is an obvious oversimplification. In order for the Helmholtz-Smoluchowski equation to hold several assumptions need to be satisfied, that are violated in porous media. Therefore, the streaming potential is not related directly to the zeta potential, but rather to the excess positive charge per unit volume Q_v [C/m³], as discussed in [Section 3-2-3](#) below.

3-2-3 Streaming potential

As explained above in [Section 3-2-1](#), SP signals measured in geophysics can originate from a wide variety of sources. Electric, hydraulic, heat and solute diffusion fluxes are all coupled, see [Figure A-2](#) for a complete overview of the coupling mechanisms. The coupling between electric current and the fluid flow in microchannels and porous media is caused by 2 electrokinetic effects, namely streaming current and electro-osmosis. Taking these coupling mechanisms into account, the transport equations for electrical current and fluid flow can be written as:

$$\mathbf{j}_{tot} = -\sigma \nabla \varphi - L(\nabla p - \rho_f \mathbf{g}), \quad (3-4)$$

$$\mathbf{u} = -L \nabla \varphi - \frac{k}{\mu} (\nabla p - \rho_f \mathbf{g}), \quad (3-5)$$

$$C = \left(\frac{\partial \varphi}{\partial p} \right)_{\mathbf{j}_{tot}=0} = -\frac{L}{\sigma}, \quad (3-6)$$

where:

\mathbf{j}_{tot}	total current density [A/m ²]	\mathbf{u}	Darcy flux [m/s]
φ	electrical potential [V]	h	hydraulic head [m]
σ	electrical conductivity of the medium [S/m]	k	intrinsic permeability [m ²]
ρ_f	fluid density [kg/m ³]	\mathbf{g}	gravitational acceleration [m/s ²]
L	streaming current and electro-osmotic coupling coefficient [m ² /Vs]		

and \mathbf{j}_{tot} means that there is no current injection. Bold symbols indicate vector fields, the other symbols are scalar field or medium parameter tensors. This symbol convention is

used consistently throughout the rest of this thesis. The Helmholtz-Smoluchowski equation (Equation (3-3)) relates the electrical potential across a microchannel to the applied pressure difference. According to this equation the coupling coefficient C is related to the zeta potential. This relationship only holds however under the following assumptions (Minsley, 2007, p. 46):

- Flow is laminar.
- Pore radius is large compared to the double layer thickness.
- Tortuosity is small.
- The surface conductivity, which is the electrical conductivity of the whole EDL (Stern and diffuse layers), can be neglected.

These assumptions do not hold for porous media, because the microstructure of the porous medium is not taken into account. Consequently, the zeta potential cannot be used to adequately describe the coupling between the streaming current and pressure gradient. Therefore, the excess charge per unit volume Q_v [C/m³] was introduced by Bolève et al. (2007), as also mentioned in Section 3-2-1. The excess charge per unit volume Q_v represents the net amount of charge, that flows along with the fluid. It can be measured using the measurement setup in Figure A-1 and was empirically related to the permeability (Bolève et al., 2012, and references therein). Using Q_v as the coupling coefficient also allows to rewrite the transport equations in terms of Darcy flux. Besides the introduction of Q_v , the influence of the electro-osmotic effect on the Darcy flux can be neglected for all practical SP applications. When neglecting the electro-osmotic effect, Equation (3-5) becomes:

$$\mathbf{u} = -\frac{k}{\mu}(\nabla p - \rho_f \mathbf{g}). \quad (3-7)$$

Substituting this expression and the expression for C (Equation (3-6)) into the transport equation for the total current density, Equation (3-4) gives:

$$\mathbf{j}_{tot} = -\sigma \nabla \varphi + \frac{L\mu}{k} \mathbf{u}, \quad (3-8)$$

$$\mathbf{j}_{tot} = -\sigma \nabla \varphi - \frac{C\sigma\mu}{k} \mathbf{u}, \quad (3-9)$$

$$Q_v = -\frac{C\sigma\mu}{k}, \quad (3-10)$$

$$\log(Q_v) = -9.9956 - 0.9022 \log(k). \quad (3-11)$$

Rewriting Equation (3-7) in terms of hydraulic head h [m] and hydraulic conductivity K [m/s] gives the final form of the two transport equations describing groundwater flow and electric current density:

$$\mathbf{j}_{tot} = -\sigma \nabla \varphi + Q_v \mathbf{u}, \quad (3-12)$$

$$\mathbf{u} = -K \nabla h, \quad (3-13)$$

where the hydraulic conductivity can be written in terms of intrinsic permeability as:

$$K = \frac{k\rho_f g}{\mu}. \quad (3-14)$$

The total current density can also be written as the sum of the conductive current density \mathbf{j}_c and the streaming current density \mathbf{j}_s where:

$$\mathbf{j}_{tot} = \mathbf{j}_c + \mathbf{j}_s, \quad (3-15)$$

$$\mathbf{j}_c = -\sigma \nabla \varphi, \quad (3-16)$$

$$\mathbf{j}_s = Q_v \mathbf{u}. \quad (3-17)$$

Finally, the continuity equations describing the conservation of electrical charge without current sources and the conservation of mass of the pore water, are given by:

$$\nabla \cdot \mathbf{j}_{tot} = 0, \quad (3-18)$$

$$S \frac{\partial h}{\partial t} = \nabla \cdot (K \nabla h), \quad (3-19)$$

where S is the storativity of the medium [-]. Given the final form of the transport equations describing the total current density (Equation (3-12)) and groundwater flow (Equation (3-13)), it is possible to solve for the hydraulic head first, separately from solving for the electrical potential. This because the effect of electro-osmosis on fluid flow was assumed negligible. Also note that the equations above only hold under saturated, viscous laminar flow conditions.

To summarize, in geohydrological applications of self-potential geophysics, there is no current injection and groundwater flow is the only primary flow that indirectly generates a potential field. Therefore, the divergence of the total current density equals 0 and streaming current density can be seen as a local current source, which is balanced by a conductive current in the entire medium.

The self-potential is usually measured at the surface. Subsequently, the streaming current density is inverted for. When doing this, it is important to have a good resistivity model of the subsurface, such that the magnitude and location of the streaming current can be estimated correctly. Furthermore, it is important to be able to adequately constrain the streaming current density in the inversion, given that the inverse problem is non-unique. As is also the case for other potential field methods.

3-2-4 Polarizable and non-polarizable electrodes

An electrode is the transducer that converts metallic current, i.e. the flow of electrons, in a metal wire to ionic current in an electrolyte and vice versa. At the anode (+) an oxidation reaction happens, that takes electrons from the metal and donates them to the electrolyte. At the cathode (-) a reduction reaction happens, that donates electrons to the metal and takes them from the electrolyte.

Non-polarizable electrodes do not hinder oxidation and reduction reactions from happening, thereby allowing for easy electrode transfer. Under direct current conditions an ideally non-polarizable electrode therefore acts as a resistor. On the other hand no electrode transfer is possible at the metal-electrolyte interface of an ideally polarizable electrode. Therefore, when applying a DC potential difference across the interface, charge accumulates at this interface. Hence, the ideally polarizable electrode behaves like a capacitor.

A platinum electrode in a NaCl solution is a common textbook example of a polarizable electrode. As long as the DC potential difference is low enough, such that no hydrolysis

occurs, there will be no current flow. The only thing that happens due to the application of the DC potential difference, is that electrode interface will become charged, i.e. becomes polarized. However, the ease with which electrodes are transferred does not only depend on the electrode material, but also on the electrolyte solution. If, for example, the surface of the platinum electrode were saturated with hydrogen gas, a redox system would be created (H/H^+). Consequently, electrode transfer were possible and the platinum electrode would become a non-polarizable electrode (Martinsen & Grimnes, 2011, [p. 49]).

Under field conditions, stainless steel stakes, which are commonly used for geophysical applications, are considered polarizable electrodes. They are however not ideally polarizable, given that they are used to inject current during ERT experiments. It is however necessary to correct for the polarization effect of the electrodes, which is done by injecting current at least twice with opposite injection polarities for every ERT quadruple. An ERT quadruple is a combination of 2 current injection electrodes (denoted A and B, or C_1 and C_2) and 2 potential measurement electrodes (denoted M and N, or P_1 and P_2).

As mentioned above in Section 3-2-1 it is common practice to use non-polarizable electrodes for SP surveys. Non-polarizable electrodes mostly consist of a metal wire submerged in an electrolyte solution of its own salt, the electrode electrolyte. Petiau and Dupis (1980) showed that Ag-AgCl electrodes are least noise sensitive. Pb-PbCl₂ electrodes followed very closely, but had better long term stability and were considerably less sensitive to temperature variations and therefore considered superior for geophysical field applications. Petiau (2000) described an optimized version of the Pb-PbCl₂ electrode, see Figure A-4. Copper-copper(II) sulfate (Cu-CuSO₄) electrodes is another type of non-polarizable electrode that is commonly used in geophysics. With the latter, current injection is possible, because the copper rod is submerged in a CuSO₄ solution. On the other hand the lead wire in the Petiau electrodes sticks in lead chloride saturated kaolinite. When injecting current with such an electrode the Pb²⁺ will either be depleted (+), or the concentration will become too high (-) in the direct vicinity of the wire. The low permeability of the kaolinite prevents diffusion of Pb²⁺ that can keep up with the required redox reaction rates necessary when injecting current, thereby breaking the electrode.

Petiau and Dupis (1980) also compared polarizable and non-polarizable electrodes for SP geophysics. Non-polarizable electrodes were found to be less noise sensitive. The reason given for this being the following. For non-polarizable electrodes the contact between soil and metal occurs in two steps. First there is the contact between the metal and the electrolyte solution of its own salt inside the electrode. The metal-electrolyte contact produces significant potentials ranging from 0.1 to 1 V. For non-polarizable electrodes this contact potential is stable, given the fixed concentration of the electrode electrolyte. The second contact is the contact between the electrode electrolyte and the electrolytes in the soil. This contact will generate diffusion potentials of a few mV.

For polarizable electrodes, the soil electrolytes are in direct contact with the metal. This causes several complications when surveying or monitoring the self-potential field. Given that the composition and concentration of soil electrolytes are variable from one place to another, the potential associated with the metal-soil electrolyte contact is variable in space. Hence polarizable electrodes are not suitable for SP surveys, because one would mainly measure the metal-soil electrolyte potential at every location, rather than the SP field.

Additionally, polarizable electrodes also suffer from larger time dependent potential fluctu-

ations than non-polarizable electrodes, because of the difference in electrode-soil coupling. When an electrode is introduced, the electrochemical equilibrium is disturbed locally. The electrolyte concentrations and charge distribution in the vicinity of the electrode will therefore change in order to compensate the disturbance. These changes in electrolyte concentration in the vicinity of the electrode have a larger effect on the potential measured with polarizable electrodes, because the largest potentials measured are associated with the metal-electrolyte contact. Additionally the electric field associated with the self-potential field also causes further polarization of the metal-soil electrolyte contact. Also these changes in the electrolyte concentrations at the metal-soil electrolyte contact have a relatively large impact on the measured potential, because of the aforementioned reason.

This different charge distribution in the vicinity of the electrode, i.e. polarization, can also cause artifacts when the electrode is moved. If the electrode is moved, the distribution of soil electrolytes around the electrode will change, which will induce a voltage in the electrode, that will in turn be measured (Neuman, 2000, chap. 48.1).

Furthermore, factors that are not of interest, such as temperature fluctuations or interaction of the soil electrolytes with the atmosphere or vegetation, have a larger effect on the potential measured with polarizable electrodes, compared to potentials measured with non-polarizable electrodes. Finally note that these temporal fluctuations, which are not of interest, also differ from one place to another.

In summary the contact between the metal and the electrolyte causes the largest potentials in the measurement system. For non-polarizable electrodes the potentials associated with this contact are constant and known, because the metal is in contact with a electrolyte solution of its salt. On the other hand the metal-soil electrolyte contact of polarizable electrodes is not constant, nor known.

Chapter 4

Modeling

The modeling described in this chapter served as a first estimate of what SP field was to be expected in the field during the full scale piping experiment performed on the test dike. A description of the test dike and experimental setup can be found in [Chapter 5](#). [Figure 5-2](#) gives a schematic representation of the dike geometry, a larger version is included in [Figure A-3](#) in the appendix.

4-1 Methodology

4-1-1 Software

The self-potential in the dike was modeled in 3D in the following 4 steps:

1. Geometry created using computer aided design (CAD) in *FreeCAD*
2. Mesh generation, local and global mesh refinement and quality checking in Gmsh ([Geuzaine & Remacle, 2009](#))
3. Finite element analysis of self-potential in pyGIMLi ([Rücker, Günther, & Wagner, 2017](#))
4. Visualization in ParaView ([Ayachit, 2015](#))

All of the above mentioned software are free and open-source. The workflow is generally applicable to geophysical modeling and inversion problems. FreeCAD is a parametric CAD program that reads many open file formats and supports Python scripting. Both FreeCAD and Gmsh use OpenCascade technology, which is an open source 3D CAD development platform. This allows complicated geometries created in FreeCAD to be correctly imported and meshed in Gmsh.

Gmsh is a versatile meshing program built to be computationally inexpensive and user friendly. It is the most widely used open-source mesh generator. By default the mesh is generated using the Tetgen algorithm, optionally the Netgen algorithm or other algorithms

can be used, some of which are still in development. By default Gmsh generates an unstructured mesh with linear triangular (2D) or tetrahedral (3D) elements. Optionally the elements can be (locally) recombined to form quadrangles (2D) or hexahedra, prisms and pyramids (3D). Besides using linear shape, i.e. basis, i.e. interpolation functions, it is also possible to generate meshes with quadratic or cubic shape functions. Gmsh also has a toolbox for visualizing mesh quality.

For meshing the test dike an unstructured tetrahedral mesh with linear elements was generated. Using the Gmsh scripting language and the graphical user interface (GUI), the unstructured mesh was locally refined around the inlet, pipe and exit hole. Quality checking was done on the basis of visual inspection and a mesh refinement study. Consequently regions and boundaries were marked, such that medium properties and boundary conditions could be set appropriately in pyGIMLi.

pyGIMLi is written in Python on top of a C++ core library, combining flexible, straight forward scripting and numerical efficiency. It provides several build in modules for e.g. seismic refraction tomography, gravimetry and spectral induced polarization. The electrical resistivity tomography module in pyGIMLi is relatively minimalistic, however highly compatible with the more versatile BERT software package (Günther, Rücker, & Spitzer, 2006; Rücker, Günther, & Spitzer, 2006, Boundless Electrical Resistivity Tomography). Apart from these modules pyGIMLi also offers a general modeling and inversion framework, not specific to a geophysical method. For solving partial differential equations, pyGIMLi offers general finite element and finite volume solvers. That solve for a scalar field given a mesh with linear or quadratic shape functions and boundary conditions. The inversion framework solves the minimization problem with a Gauss-Newton algorithm and can be used to write problem specific inversion routines, such as time-lapse or joint inversions. The self-potential in the dike was modeled in two steps using the finite element solver. 1 solve for the groundwater flow and calculate the streaming current density. 2 solve for the self-potential field, with the streaming current density from 1 as the current source. The result was then exported as in .vtk format and visualized in ParaView.

In case interested in the the FreeCAD \rightarrow Gmsh \rightarrow pyGIMLi workflow, it is highly recommended to consult the pyGIMLi documentation after the release of version 1.1. FreeCAD and Gmsh are general purpose software and therefore some tips and tricks can be very useful when making a mesh for pyGIMLi. Things to consider: correctly modeling the geometry in FreeCAD and importing to Gmsh; local mesh refinement; including sensors (e.g. electrodes) in the mesh; correctly labeling regions, boundaries and sensors in Gmsh such that they can be used in pyGIMLi; importing the mesh in pyGIMLi, setting boundary conditions and modeling. For now, before the release of pyGIMLi version 1.1, BERT is not yet integrated into pyGIMLi and a ERT modeling and inversion example showing the mentioned workflow with BERT can be found in [Appendix C](#).

4-1-2 Simulations

[Figure A-3](#) shows the geometry of the test dike and [Section 5-1](#) gives an extensive description of the test dike. Relevant for SP modeling is that fluid flow was assumed to only occur in the sand channel underneath the dike under saturated conditions and that flow through the core of the dike would be prevented by the clay cover on the top of the dike. To further simplify

SP modeling, flow was assumed viscous laminar, also in the pipe. The flow regime in a pipe is, however, most likely inertial laminar, see [Section 3-1-5](#) and [Section 3-2-1](#).

The SP was modeled in 2 separate steps for several steady state situations with different pipe lengths. First, the fluid flow was modeled on a mesh that comprised only the sand channel underneath the test dike, see [Figure 4-1](#). The streaming current density was also calculated on this mesh. As a second step, the streaming current density was interpolated onto the SP mesh and the SP field was calculated with the divergence of the streaming current density as the source term. The finite element solver in pyGIMLi solves the following general partial differential equation:

$$\frac{\partial u}{\partial t} = \nabla \cdot (a\nabla u) + bu + s(\mathbf{r}, t), \quad (4-1)$$

where $u(\mathbf{r}, t)$ is the scalar field that is solved for; $a(\mathbf{r})$ is the medium diffusivity; $b(\mathbf{r})$ is a damping term; $s(\mathbf{r}, t)$ is the source term. Implementing fluid flow and SP simulation in pyGIMLi then results in the following equations:

Fluid flow & streaming current	Self-potential
$0 = \nabla \cdot (K\nabla h)$	$0 = \nabla \cdot (\sigma\nabla\varphi) + s(\mathbf{r})$ (4-2)
$\mathbf{u} = -K\nabla h$	$s(\mathbf{r}) = -\nabla \cdot \mathbf{j}_s$ (4-3)
$\mathbf{j}_s = Q_v(K)\mathbf{u}$	(4-4)

Note that the excess charge per unit volume Q_v is a function of the permeability according to the empirical relationship in [Equation \(3-11\)](#). The hydraulic conductivity K , in turn, is a function of the permeability k ([Equation \(3-14\)](#)). Hence the excess charge per unit volume is a function of the hydraulic conductivity $Q_v(K)$.

As boundary conditions for the fluid flow, the upstream head was set as a Dirichlet boundary condition on the inlet area. The inlet area, see the top of [Figure 4-1](#), had the size of the infiltration box that was attached to the end of the entry pipe. The top of the exit hole had a $h = 0$ boundary condition imposed on it. No flow Neumann boundary conditions were applied everywhere else. The hydraulic conductivity of the sand channel was 8×10^{-5} m/s, which was determined in the lab ([Pol et al., 2019](#)). [Table A-1](#) lists the permeability and other properties of the sand. The pipe was modeled as 10 mm wide and 1.8 mm deep corresponding to dimensions reported by [Van Beek \(2015\)](#) and the modeling efforts of [Bersan et al. \(2013\)](#). The permeability of the pipe and exit hole were estimated at 5×10^{-3} m/s. This was an equivalent hydraulic conductivity calculated under Hagen-Poiseuille flow conditions in a pipe, following the approach suggested by [Bersan et al. \(2013\)](#).

The SP mesh comprises of a region of interest which resembles the test dike. A 20 m wide dike with cross sectional dimensions as shown in [Figure A-3](#). The domain around the region of interest was also modeled, such that the electrical potential could be set to 0 at the outer boundaries of the model, without influencing the SP field. Setting $\varphi = 0$ at the outer boundary corresponds with the definition that the electrical potential approaches 0 at infinity. A no flow Neumann boundary condition was applied to the earth's surface.

The meshes were locally refined around areas with small geometrical features and where gradients were high. Mainly at the inlet, exit hole and pipe. Further outward elements were allowed to become bigger, in order to reduce the total number of elements and thus the computational cost. The flow and SP meshes in [Figure 4-1](#) with a 25 cm long pipe

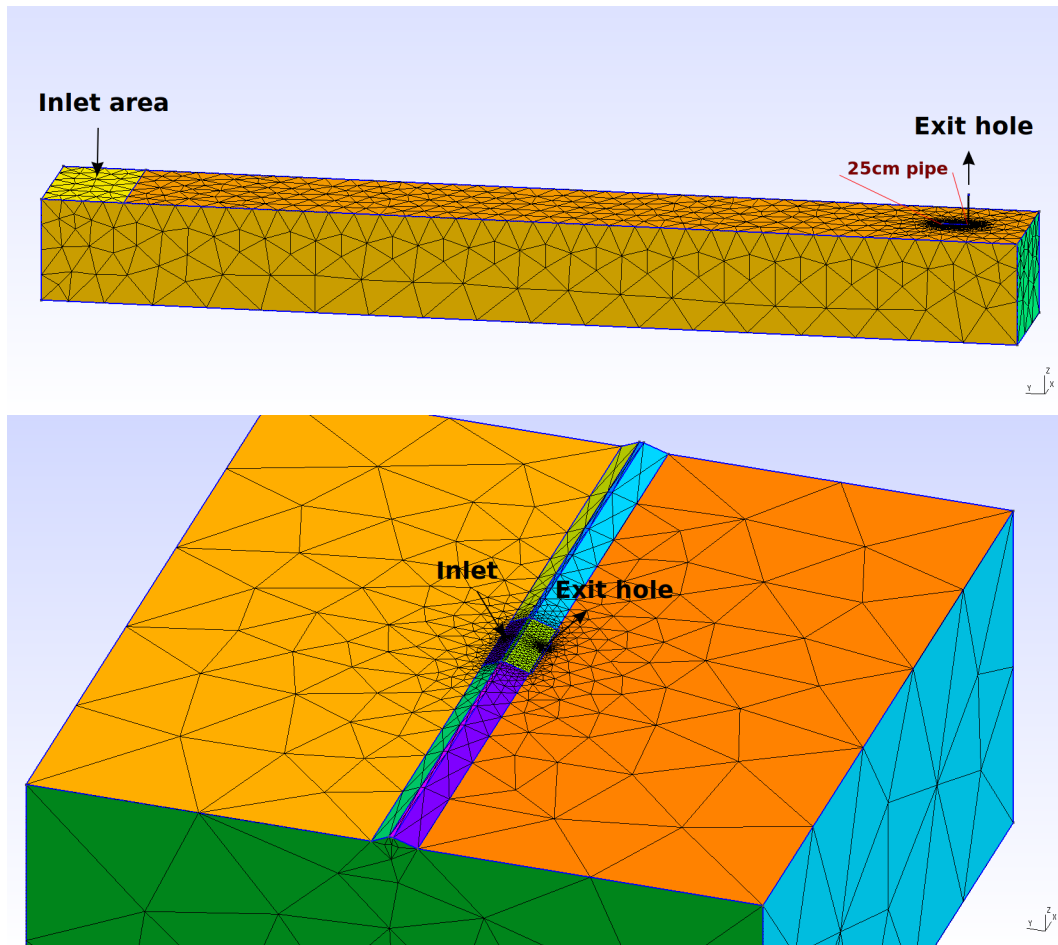


Figure 4-1: Top: flow mesh of 1.2 m wide, 1 m deep, 9.5 m long sand channel, with a 25 cm long pipe and 30 cm high exit hole. The exit hole is the rupture in the cover blanket and has a 13 mm diameter. BC's: upstream head on inlet area; $h = 0$ on the top of the exit hole; no flow Neumann boundary conditions everywhere else. Bottom: SP mesh. The middle part of the domain is 20 m wide, which is the width of the crest of the test dike. Outer domain is big enough such that $\varphi = 0$ BC does not influence the SP field in the region of interest. No flow Neumann BC at the earth's surface.

were used for several numerical simulations. First a mesh refinement study was performed to ensure numerical accuracy of the model. For this mesh refinement study, an upstream head of 1.5 m and homogeneous resistivity of 200 Ωm were used. Subsequently, the influence of the resistivity was investigated with an upstream head of 1.5 m. And the influence of the upstream head was investigated with a resistivity model obtained from an ERT survey on the test dike. Finally, the SP response without a pipe and with a 5 cm; 25 cm; 1 m and 4 m long pipe were modeled to get an indication of the expected development of the SP response during the field experiment. In summary:

1. Mesh refinement study on the flow mesh with 1.5 m upstream head.
2. Mesh refinement study on the SP mesh with a homogeneous resistivity of 200 Ωm .
3. Influence of resistivity on the SP response by varying the homogeneous resistivity and

by using the resistivity model obtained from an ERT survey on the test dike.

4. Influence of head/flow rate on the SP response with the ERT resistivity model.
5. Pipe length on the SP response with the ERT resistivity model and 1.5 m upstream head.

4-2 Results

As explained above, the fluid flow and SP were modeled separately on the two meshes shown in [Figure 4-1](#). In [Figure 4-2](#) above the SP field in the test dike was clipped at $x = 11.5$ m, such that the fluid flow results could be superimposing in the same visualization. The negative SP anomaly was found at the inlet and the positive anomaly at the exit hole. The result visualized was modeled with an upstream head of 1.5 m and using the resistivity model resulting from the inversion of ERT data obtained prior to the piping experiment. This ERT resistivity model is shown in [Figure 5-8](#) and [Figure 5-9](#). The ERT acquisition design, inversion and results are described in [Section 5-2-2](#) and [Section 5-3-2](#). In the rest of this section, the results of the mesh refinement study, the influence of the resistivity and flow rate on the SP and the pipe length are discussed.

4-2-1 Mesh refinement study

The results of the mesh refinement studies on the flow mesh and SP mesh with a 25 cm long pipe, 1.5 m upstream head and a homogeneous resistivity of $200 \Omega\text{m}$ are shown in [Figure 4-3](#) and [Figure 4-4](#) respectively. For the mesh refinement study on the flow mesh, the outflow at the exit hole was chosen as the parameter that had to converge. The mesh selected in the flow mesh refinement study was then used to do the SP mesh refinement study. For the SP mesh refinement study, the SP at the exit hole and at a point 3.5 m up the dike were plotted as a function of the number of elements.

The red dot in [Figure 4-3](#) corresponds to the mesh that was considered to have a good trade off between accuracy and computational cost. The selected mesh had an element size factor of 0.4, which means that the element edges are 0.4 times the length of those in the mesh in [Figure 4-1](#).

The convergence of the SP mesh is less smooth. The reason being that the streaming current density is interpolated from the flow mesh onto the SP mesh, which introduces numerical errors, especially exactly at the exit hole. There the SP value does not converge within the investigated number of elements. However, further away from the exit hole, the SP does stay relatively constant for an increasing number of elements. Therefore the meshes indicated with the red dots were considered a fair trade of between computational cost and accuracy. The selected mesh had an element size factor of 0.6, thus the edges of the selected mesh are 0.6 times the length of the element edges in [Figure 4-1](#).

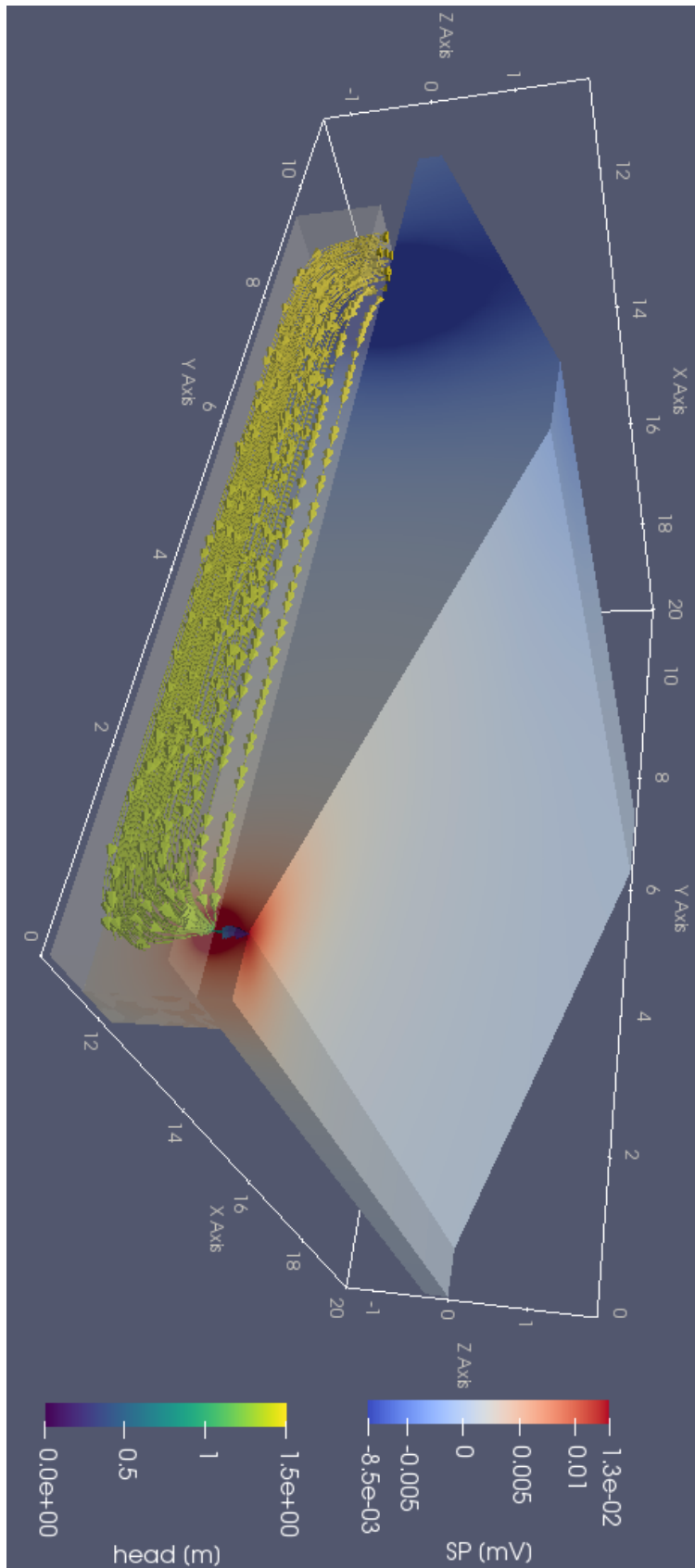


Figure 4-2: SP field in the test dike, dipped at $x = 11.5\text{ m}$, such that the fluid flow in the sand channel could be visualized with streamlines. The negative SP anomaly can be seen at the inlet area. The positive SP anomaly is visible at the 13 mm diameter exit hole. Upstream head: 1.5 m. Resistivity model: ERT inversion result of data acquired prior to the piping experiment.

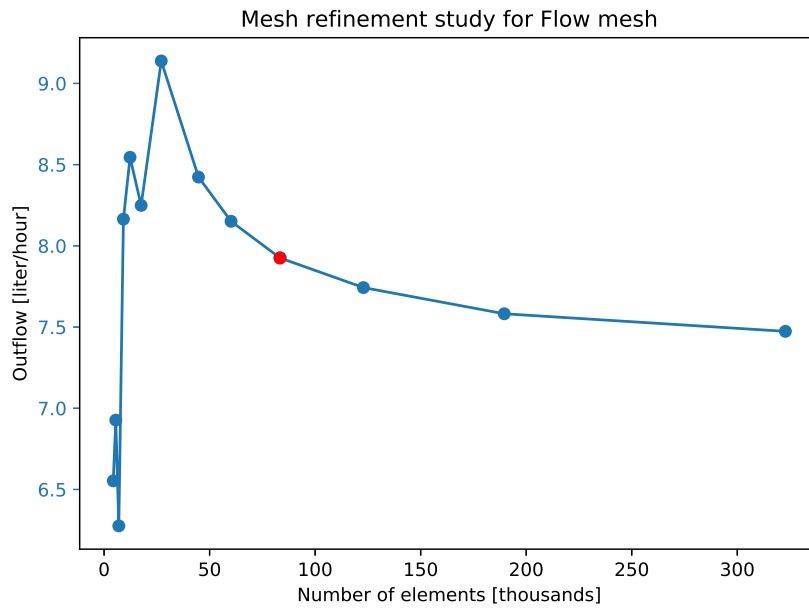


Figure 4-3: Mesh refinement study for flow mesh with a 25 cm pipe length and an upstream head of 1.5 m. The red dot indicates the flow mesh selected for further SP, which corresponds to the mesh in Figure 4-1 with an element size factor of 0.4.

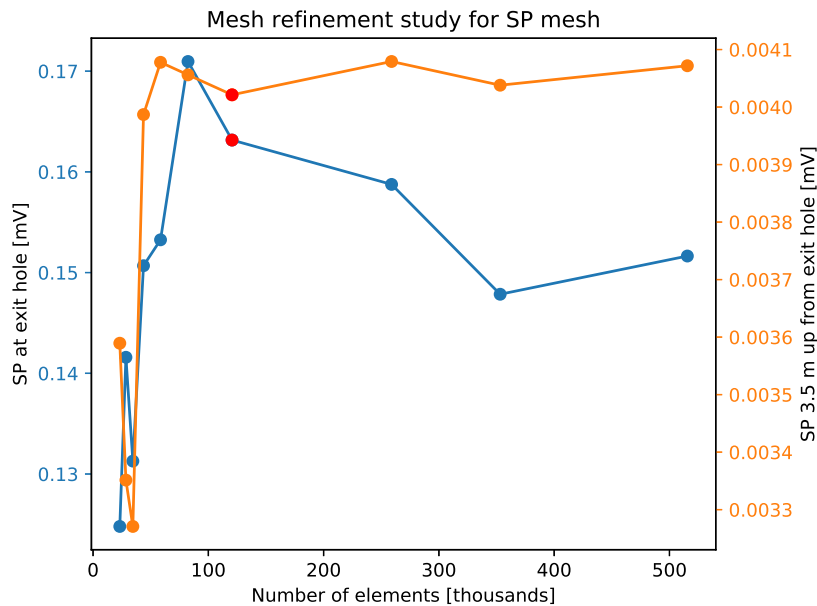


Figure 4-4: Mesh refinement study for SP mesh based on the selected mesh from the flow mesh refinement study and a homogeneous resistivity of 200 Ω m. The red dots indicate the SP mesh selected for further SP modeling, which corresponds to the mesh in Figure 4-1 with an element size factor of 0.6.

4-2-2 Influence of resistivity on SP

The influence of the medium resistivity on the SP response was investigated using the meshes with a 25 cm pipe length, selected in the mesh refinement study. The upstream head was 1.5 m. Figure 4-5 shows the linear relationship between the homogeneous medium resistivity and SP. The higher the medium resistivity the higher the SP signal, which is a simple consequence of the linearity of the governing equations.

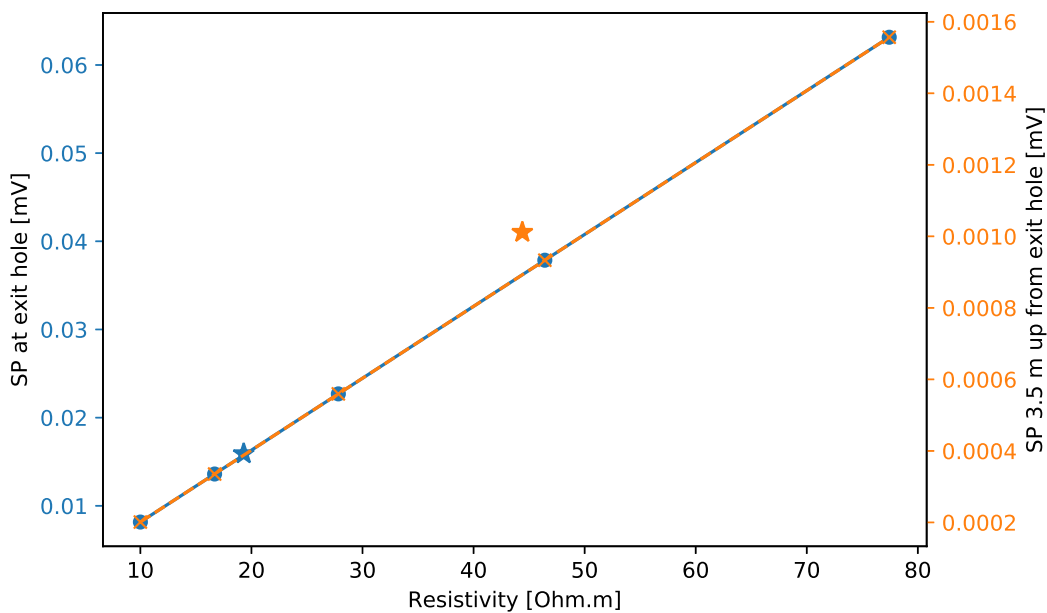


Figure 4-5: SP response at the exit hole and 3.5 up the dike from the exit hole as a function of homogeneous medium resistivity. Stars indicate the SP response when the ERT resistivity model was used. The resistivities at which the stars are plotted correspond to their local resistivities in the ERT resistivity model.

When using 3D resistivity model obtained from inversion of ERT field data, the SP distribution in the 20 m wide dike looks as displayed in Figure 4-2 and Figure 4-6. Visually the SP response with a homogeneous resistivity model and the SP response with the ERT resistivity model do not differ much. In both cases, the SP field has a dipolar signature with the positive anomaly at the exit hole and the negative anomaly at the inlet. Both the positive and negative anomalies had a circular shape. The negative anomaly was spread out over a larger area on the surface, because the inlet area is larger than the exit hole and because the inlet area is not at the surface.

The stars in Figure 4-5 are the SP signals at the exit hole and at 3.5 m above the exit hole, when using the ERT resistivity model to model the SP. The stars are plotted at their corresponding resistivities in the ERT resistivity model. So the resistivity at the exit hole was 20 Ωm and the resistivity 3.5 m up the dike from the exit hole was 45 Ωm . The fact that the stars are close to the linear line is not supposed to suggest that the SP is a function of the local resistivity. It does however motivate clearly that it is important to have a good resistivity model of the entire domain when modeling SP. To clarify, a homogeneous resistivity model of 20 Ωm (blue star) would result in an incorrect SP 3.5 up from the exit hole. Similarly, a

homogeneous model of $45 \Omega\text{m}$ would result in an incorrect SP at the exit hole. And to a lesser extent, the SP 3.5 m up from the exit hole would also be incorrect when using a homogeneous resistivity model of $45 \Omega\text{m}$.

4-2-3 Influence of upstream head on SP

With an upstream head of 1.5 m and a 25 cm long pipe, the outflow through the exit hole is 7.9 liter per hour and the SP at the exit hole is 0.016 mV, see blue star in [Figure 4-5](#). As dictated by the governing equations for fluid flow and SP, both the outflow and SP are linearly dependent on the upstream head. If the upstream head doubles, both the outflow and SP double.

4-2-4 Influence of pipe length on SP

In total 5 simulations were performed. One simulation without a pipe and four simulations with a 5 cm; 25 cm; 1 m and 4 m long pipe respectively. [Figure 4-6](#) displays the SP signal on the dike when there is no pipe (top) and when there is a 25 cm long pipe (bottom). The largest difference was observed between the model without a pipe and the models with a pipe. The flow rate increased by about 1 liter per hour and the SP signal increased in magnitude, by about 0.002 mV at the exit hole. However, neither the outflow, nor the SP signal changed as the pipe length was increased. The reason for this was that an increase in pipe length did not significantly influence the fluid flow, as is explained below.

The fluid flow pattern in the sand channel without a pipe is visualized in [Figure 4-7](#). At the far end, the water flows in through the inlet area, where a 1.5 m head was applied. The water flows through the sand channel to the exit hole and then up and out as shown by the streamlines. From the color of the streamlines, which indicate the hydraulic head, it is clear that the largest head drop occurs right below and inside the exit hole. The flow converges toward the tiny 13 mm wide exit hole, which is the bottle neck in this flow system. A high flow resistance is associated with high gradients and backward erosion occurs where the hydraulic gradient is high.

The pipe was modeled as a 1.8 mm deep, 10 mm wide cuboid of different lengths with a very high permeability. [Figure 4-8](#) shows a close up of flow towards the exit hole without a pipe in the top and a close up of flow towards a 25 cm long pipe in the bottom. Looking at the bottom image, it is clear that water flows towards the pipe. Especially close to the exit hole. However, not many streamlines run toward the tip of the pipe. The reason for this being that the pipe close to the exit hole is too small, i.e. causes too much flow resistance, for the high pressures to be displaced to the tip of the pipe. In other words, the pressure gradients are still highest close to the exit hole, because the exit hole and small pipe are still the bottle neck of the flow system. The dimensions of the pipe close to the exit hole would have to grow, before the bottle neck of the system would move to the tip of the pipe.

The bottom image in [Figure 4-8](#) shows that very little water flows towards the tip of the 25 cm long pipe. Similarly, very little water flowed towards the tip of the 1 m and 4 m pipes. Hence, the flow did not change when the length of the pipe changed. The main difference was observed between models with and without a pipe. Given that the SP field is directly related

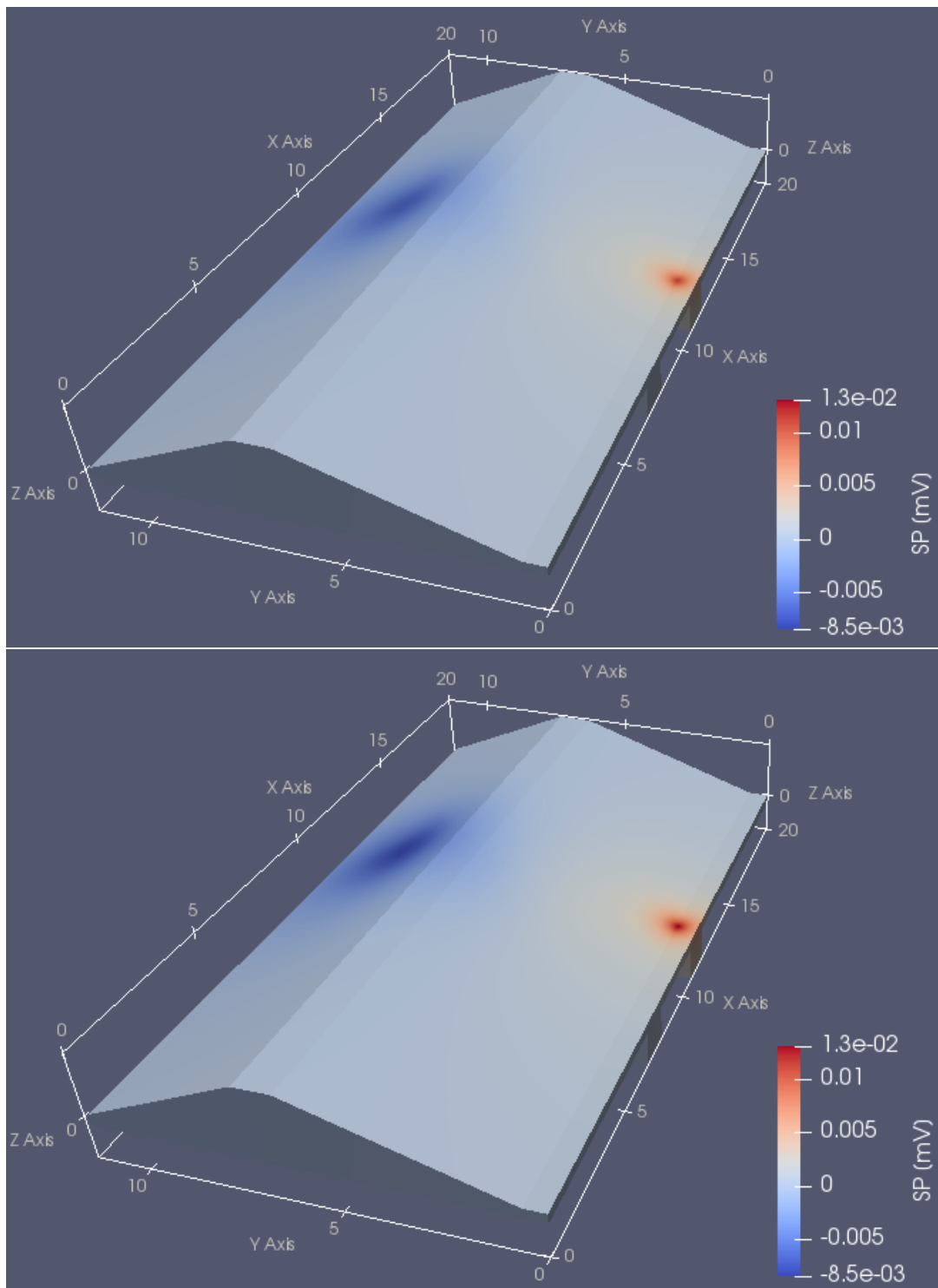


Figure 4-6: SP in the region of interest, with 1.5 m upstream head and ERT resistivity model. The SP in the outer domain is not visualized. Top: SP without a pipe. Bottom: SP with a 25 cm pipe.

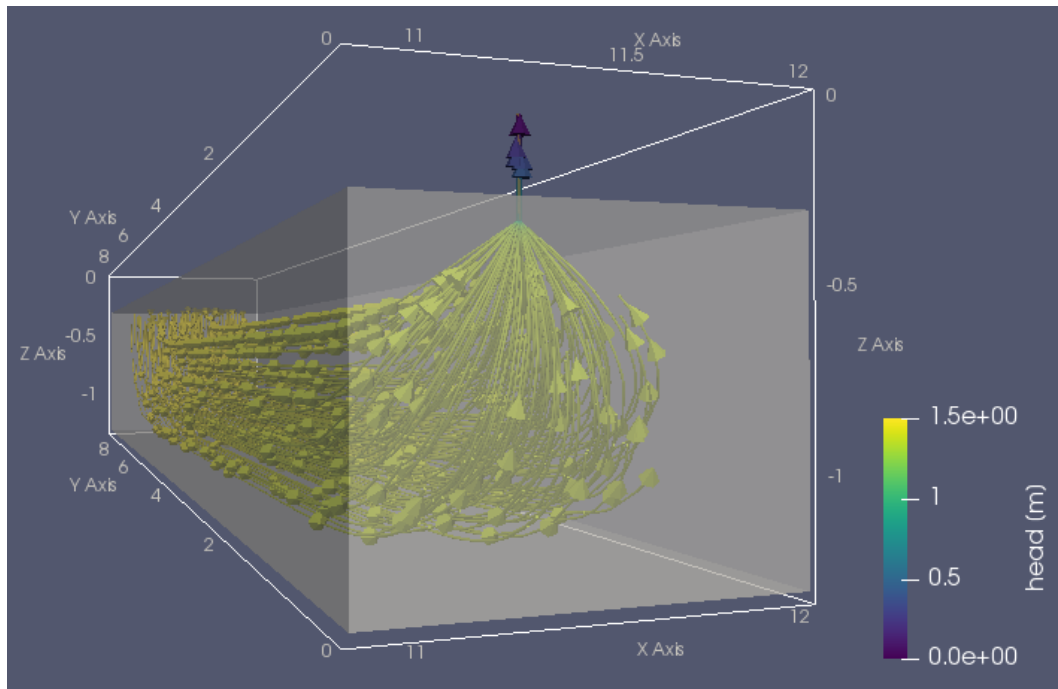


Figure 4-7: Fluid flow in sand channel without pipe, from the inlet area at the far through the sand bed and then converging towards the exit hole. The color of the streamlines indicates the hydraulic head. Largest head gradients close to and in the exit hole.

to the flow, the main differences in the SP were observed between models with and without a pipe.

The flow towards a pipe described above shows that widening and deepening of the pipe away from the tip has to occur, in order for the pressure gradient at the tip of the pipe to stay high. In reality, this is also the case, see [Section 3-1](#). The pipe is deeper and wider away from the tip of the pipe. Widening and deepening of the pipe is caused by secondary erosion. Which ensures that the gradient stays high at the tip of the pipe, which is a requirement for primary erosion, i.e. growth of the pipe at the tip.

4-3 Discussion and Recommendations

The presented FreeCAD → Gmsh → pyGIMLi workflow is incredibly versatile, but might take some time to get acquainted with. Therefore please consult the pyGIMLi documentation or [Appendix C](#) in case interested. The workflow allows for the creation and meshing of complicated geometries with the graphical user interfaces of FreeCAD and Gmsh. The mesh can then be used in pyGIMLi for modeling and inversion of several standard and customized geophysical problems.

This developed workflow was then applied to model SP in the test dike, to get a first estimate of what to expect in the field. The modeling was done in 2 separate steps. 1. flow and streaming current density modeling under saturated conditions in the sand channel underneath the dike. 2. modeling of the SP field, using the divergence of the streaming current

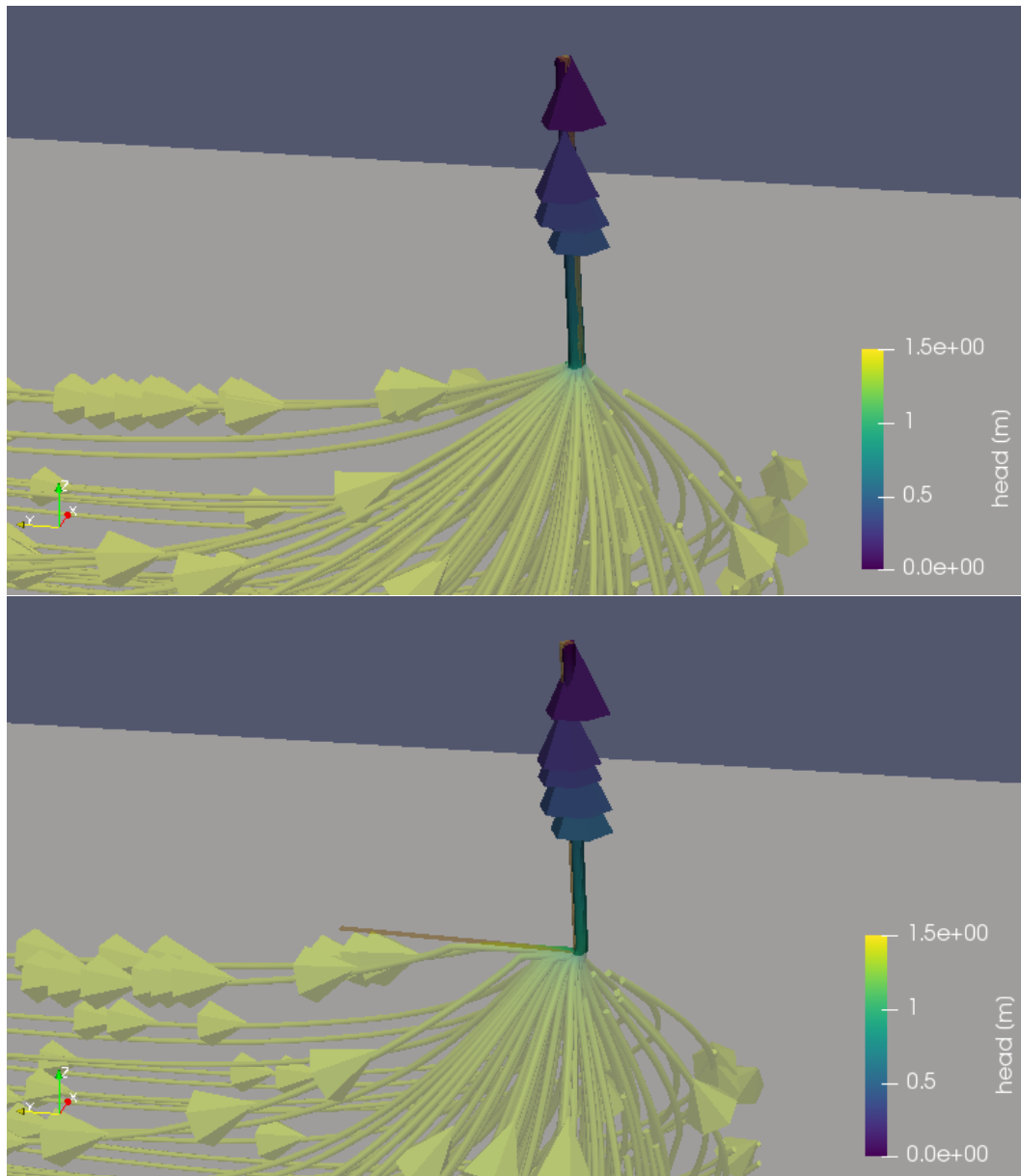


Figure 4-8: Close up on how fluid flow converges towards the exit hole (top) and pipe and exit hole (bottom). The flow converges to the pipe close to the exit hole, not to the pipe tip.

density calculated in 1. as the source.

With this modeling approach several simulations were performed. First, a mesh refinement study was done to ensure an acceptable trade off between numerical accuracy and computational cost. Using a more powerful computer is advised for future modeling efforts however. A more powerful computer would have allowed to pick finer meshes as flow mesh and SP mesh. With a finer flow mesh and the possibility to investigate finer SP meshes, the convergence of the SP mesh would likely have been more smooth. Subsequently, meshes could have been picked that guaranteed numerical accuracy, rather than the meshes that offered a fair trade

off between numerical accuracy and computational efficiency used here.

After the mesh refinement study, it was confirmed that the SP signal in the model is indeed linearly dependent on the homogeneous medium resistivity and the flow rate. Furthermore, it was demonstrated that an good resistivity model is a requirement when accurately modeling SP. Finally, the influence of the length of the pipe on the SP signal was investigated.

It turned out that the magnitude of the modeled SP signal is very small. The maximum SP signal in the most realistic scenarios, see [Figure 4-6](#), was no higher than 0.013 mV. And more importantly, the difference in SP signal between simulations with and without pipe were even smaller. Therefore, it was not likely that an SP signal would be measured in the field that could be related to the growth of a pipe. This was, however, not known prior to going to the field.

The main reason that the SP signal turned out so small, was that the flow rates were very small in the test dike. Examples of SP surveys and monitoring efforts performed for localizing leakages in dams reported much higher flow volumes and hence measurable SP signals of 3 to 15 mV ([Bolève et al., 2009](#); [Koelewijn et al., 2014](#), see also SP literature review [Section 3-2-1](#)).

The simulations with different pipe lengths showed that widening and deepening of the pipe due to secondary erosion has to be taken into account. Not modeling secondary erosion was an oversimplification, because very little water flowed towards the tip of the pipe, resulting in an unrealistic flow field. Moreover, a pipe with the modeled tiny cross section over the entire length of the pipe could not exist in reality, because gradients at the tip of such a pipe are too low for the pipe to grow to such a length.

The SP field is a direct consequence of the fluid flow field. Hence, future research in modeling the development of the SP field during backward erosion piping should be directed towards accurately modeling the change in flow field as the pipe grows. Additionally, Richard's equation for unsaturated flow could be incorporated. This to also take into account the influence of the SP that is the consequence of unsaturated flow in the core of the dike. In modeling the SP field on the test dike, unsaturated flow through its core was assumed to be negligible, because of the short duration of the experiment. However, even though the flow velocities through a clay dike are low, the excess charge per unit volume Q_v is much higher in clay than in sand. Therefore unsaturated flow in the core of the dike is expected to have a considerable impact on the total SP field.

Chapter 5

Field Experiments

This chapter motivates the methodology applied during the SP measurements in the field and also describes the methodology followed for the piping experiment on the test dike briefly. Afterwards the results of the field experiments are presented and discussed.

5-1 Description of the Test Site

The test dike is located close to the campus of the Delft University of Technology on the Flood Proof Holland testing facility. The dike was built in one of the basins with the aim of overflow, flood damage and backward erosion piping tests. The piping experiments conducted on this test dike were aimed at measuring piping progression rates in a large scale setup. This was done to validate lab scale experiments and transient numerical piping models.

Figure 5-1 shows areal photos of the Flood Proof Holland testing facility on the left. With the test basin indicated with the red square. The basin is 1.8 m deep and lined with concrete slabs. The right photo shows the basin with the dike in place. For the construction of the dike, the concrete slabs in the middle of the basin were removed. Then 2 channels were dug out in the weak organic clay and peat base below the basin. A HDPE (high-density polyethylene) foil was installed on all sides of the channels, to prevent undesired seepage. Then the channels were filled with fine, well sorted sand, the sand was compacted and the dike was built on top. The upstream basin can be filled from the storage basin. Water that enters the downstream side of the dike can be pumped away.

The geometry of the test dike and the 2 sand channels, in which piping was to form, are shown in Figure 5-2. A larger version of Figure 5-2 has been included in Figure A-3 in the appendix. The sand channels are connected to the upstream basin with an entry pipe and infiltration box. Given the maximum head drop of 1.8 m, the Sellmeijer model predicted that the critical head would not have been exceeded, if the seepage length had been the entire length of the dike. By installing the entry pipe, the seepage length was reduced from 10 to 7.2 m. Thereby the critical head reached 1.4 m and piping could progress completely.



Figure 5-1: Left: an areal photo of the Flood Proof Holland test facility. The red square indicates the basin in which the test dike was constructed. Right: areal photo of the test dike. The upstream basin can be filled from the storage basin. The yellow lines indicate the geometry of the dike and upstream basin. Source: Pol et al. (2019)

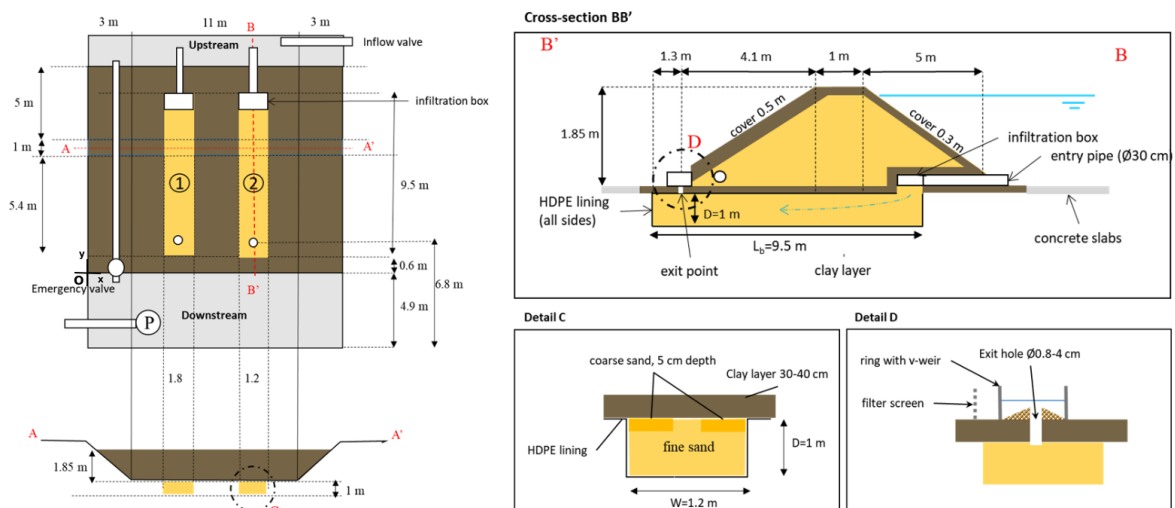


Figure 5-2: Schematic drawing of the test dike. Note that the drawings are not to scale and that cross section BB' is a view in negative x direction. Source: Pol et al. (2019)

The channels were filled with fine sand and compacted. In the top 5 cm of the channels, strips of coarse sand were introduced to guide the pipe through the middle of the sand channel, see Detail C of Figure 5-2. d_{50} of fine and coarse sands are approximately 200 and 400 μm respectively. More sand properties are listed in Table A-1. The coarser sand is less sensitive to erosion, therefore the pipe will stay in the middle of the channel. The sand channel was covered by a 30 cm thick clay layer. A series of 13 piezometers was installed between the exit hole and the infiltration box at the interface. With the readings from these piezometers the location of the pipe tip can be inferred. A sand core was built on top of the blanket layer, which was then covered. On the upstream side of the dike the cover is a 30 cm thick clay layer. On the downstream side, the cover is 50 cm thick and is made of three 3 m wide strips of clay, sand and loam. These different covers were created for the overflow tests. As a last step the whole dike was covered with grass sods.

Given that the test dike was built on weak organic clay and peat, the dike settled. That is the reason that the entry pipes were slanted upward, see the right photo in [Figure 5-3](#). The side of the pipe that was attached to the infiltration box settled together with the dike. While the side in the upstream basin did not settle, because it rested on a concrete slab.

In total the piping experiment was successfully performed twice on channel ②. Piping never developed in channel ①. Because backward erosion did not occur, even at the maximum 1.8 m head. 17 December 2018 the first successful piping experiment on channel ② was conducted. The results of the first piping experiments are described in "Temporal Development of Backward Erosion Piping in a Large Scale Experiment" by [Pol et al. \(2019\)](#). The second piping experiment was started at 9:45 in the morning on 3 September 2019.

5-2 Methodology

This section describes the procedures followed during the piping experiment and how the SP monitoring system on the test dike was designed. A short motivation for the geometry of the test dike was already given above.

5-2-1 Piping experiment

In short the piping experiments went as follows. The water level in the upstream basin was raised stepwise ([Figure 5-3](#)), until the progressive stage of backward erosion was initiated. Then the water level was kept constant and the pipe was allowed to grow. Finally the experiment was terminated when the pipe fully progressed upstream. This was done by opening the emergency valve, see [Figure 5-2](#).

The position of the pipe tip could be inferred from the piezometer readings. When the pipe tip is growing towards a piezometer, the pressure will first increase. And as soon as the pipe had reached the piezometer the pressure would drop again. When the backward erosion process reached an equilibrium, ground water flow reached a steady state. Therefore pressure stabilized. Such stabilization occurred during the equilibrium stage of backward erosion. It signaled that the water level needed to be increased, such that the progressive stage of backward erosion could be initiated. During the whole experiment the flow of water was monitored by reading the v-weir, see [Figure 5-3](#). Additionally, the amount of eroded sand was measured by collecting the sand at the exit hole with a kitchen spoon.

The aim of the second experiment was to investigate how much the pipe healed during the 8 months between the two experiments. In order to determine this the 2 following things were looked at:

1. Is the critical head the same or lower than during the first experiment?
2. Does the progressive stage of backward erosion take less time during the second experiment?

5-2-2 Self-potential

As explained in the research outline in [chapter 2](#), the monitoring principle was as follows. As piping initiates and progresses, the groundwater flow field changes. Due to the coupling of



Figure 5-3: Left: ring (bucket without bottom) around the exit hole with a v-weir and measure tape. Right: upstream basin being filled at the start of the experiment. Entry pipes are slanted upward because of settlement of the dike.

groundwater flow and the electrical potential field, the change of the potential field contains information about the progression of the pipe. To measure this effect self-potential field experiment had the following outline:

1. Electrical resistivity tomography (ERT)
2. 24 hr SP null-measurement
3. SP monitoring during the piping experiment

The ERT surveys were conducted to estimate the resistivity of the dike. As was shown in [chapter 4](#), the resistivity has to be known accurately when modeling SP. Similarly, the resistivity of the subsurface has to be known, such that the location of the streaming current density can be inferred from SP data. Most of the electrodes used in the ERT surveys were later also used during SP monitoring. Both ERT and SP measurements were performed with an IRIS Instruments Syscal Pro. The 24 hr null-measurement before the piping experiment was done to determine the SP signal when there was no piping.

Several weeks before the piping experiments a preliminary fieldwork was conducted, with the aim to make sure that everything would go according to plan during the piping experiment. Additionally, it allowed to test the sensitivity of the measurement setup and to develop a strategy for drift compensation. Where drift is the time dependent variation of the measured voltage, unrelated to the SP. During the preliminary fieldwork the upstream basin was not filled with water. The streaming current was simulated by injecting DC current between the inlet and exit hole of the test dike. The photo in [Figure 5-4](#) shows the SP measurement setup during both field experiments.

Polarizable and non-polarizable electrodes

During preliminary fieldwork as well as during the piping experiment the following electrodes were used: 143 stainless steel field electrodes; 1 copper-copper(II) sulfate field electrode; 1



Figure 5-4: Photo of SP monitoring setup on the downstream side of the dike, during the piping experiment. The orange cables connected the 144 field electrodes to the IRIS instruments Syscal Pro inside the tent. Wooden poles were in place for overtopping experiments and had nothing to do with the SP monitoring system.

stainless steel reference electrode; 1 copper-copper(II) sulfate reference electrode. Photos of the used electrodes can be found in the appendix [Figure A-4](#). That figure also shows the Petiau electrode, which is another type of non-polarizable electrode that is often used in SP geophysics.

The stainless steel electrodes were 30 or 40 cm long, 2 cm thick stakes. These electrodes are polarizable. The copper-copper(II) sulfate electrodes were made of a 20cm long, 4 cm diameter porous pot with a plastic screw cap. The porous pot was filled with 70 ml of copper(II) sulfate solution with a concentration of 350 g/l. A copper rod goes through the plastic screw cap and is submerged into the CuSO_4 solution in the porous pot. These electrodes are non-polarizable electrodes.

One of the main reasons for using polarizable electrodes was their ease of use. The stainless steel stakes could simply be hammered into the ground. Whereas, in order to install the non-polarizable electrodes, a small hole needed to be bored. The hole was slightly larger than the electrode, so the electrode needed to be installed in the hole with additional clay, such that good coupling was ensured. The porous pot then had to be carefully filled up with copper(II) sulfate solution, which is acidic. The non-polarizable electrodes also had to be serviced during the experiment, because the copper sulfate solution leaked out within 24 hr. If too much copper sulfate leaks into the ground, this might also have a negative impact on the environment, see environmental impact of copper(II) sulfate in [section 5-3-2](#).

Installing Petiau lead-lead chloride electrodes is also labor intensive. They also must be installed in a hole with clay. However once installed they do not need servicing. The reason for not using Petiau electrodes was that they cannot be used for injecting current, which

conflicted the ambition to build one monitoring system for both ERT and SP measurements. Besides that, the polarizability of the stainless steel stakes was assumed to not significantly influence the measurements. This because of the following 3 reasons:

1. The metal-soil electrolyte contact was not expected to polarize significantly due to current flow through this surface, because the current flow in the measurement circuit is negligible due to the high impedance of the voltmeter.
2. Polarization of, i.e. changes in electrolyte concentrations at the metal-soil electrolyte contact, due to the SP field were assumed negligible.
3. Extra time dependent variation in the SP signal, due to the use of polarizable electrodes was expected to be compensatable.

To quantify the difference in time dependent variation of the signal, data acquired with polarizable and non-polarizable electrodes was compared. During ERT measurements, current is injected at all electrodes, therefore ERT was performed at least 1 day prior to SP measurements, such that polarizable electrodes had the time to depolarize.

Electrical resistivity tomography

In an electrical resistivity tomography survey data is acquired by injecting current between two injection electrodes A and B and simultaneously measuring the potential difference between two measuring electrodes M and N. Such a combination of 4 electrodes is called a quadruple. From this data the apparent resistivity can be calculated:

$$\rho_a = K * \frac{V_{MN}}{I_{AB}}, \quad (5-1)$$

where ρ_a is the apparent resistivity [Ωm]; K is the geometric factor [m], which is a function of the quadruple configuration, e.g. dipole-dipole or Wenner-Slumberger and topography; V_{MN} is the potential difference between potential electrodes M and N and I_{AB} is the current between injection electrodes A and B.

ERT was done a day in advance of the SP measurements, both during the piping experiment and the preliminary fieldwork. The ERT acquisition designs are shown in [Figure 5-5](#). The dike was assumed relatively homogeneous in the longitudinal direction, therefore ERT data was acquired in crosswise lines over the dike. For the inversion the data from all lines was combined to get a 3D resistivity model.

During the preliminary field work, ERT data was acquired over 8 lines across the dike, with 0.5 m electrode spacing measured overground. Measurements were taken both with dipole-dipole and Wenner-Slumberger quadruple configurations. For the ERT data acquired prior to the piping experiment, the electrodes were put in 7 lines similar to the preliminary fieldwork. The difference was that on the downstream side of the dike, the electrodes were placed in a checkerboard pattern. The checkerboard pattern was chosen for the SP data acquisition to get better spacial coverage. Measurements were taken with a dipole-dipole configuration.

The ERT lines also extended to the downstream side of the dike, such that a better resistivity model of the entire dike could be obtained. In the proposed long term monitoring system,

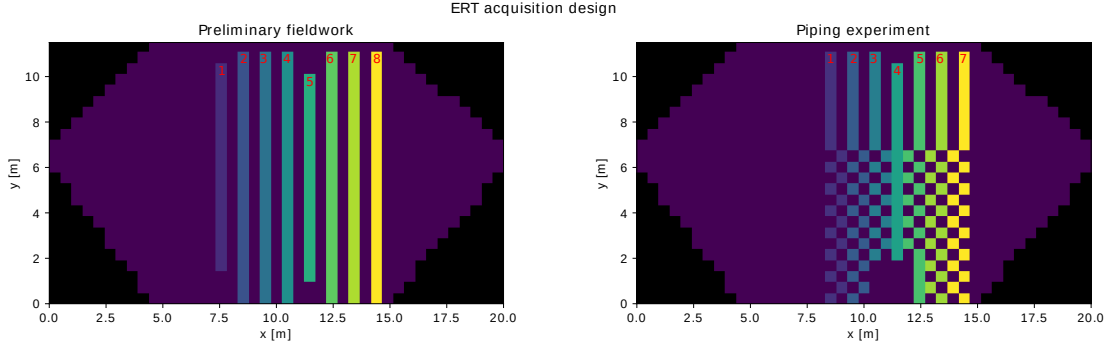


Figure 5-5: Top view of ERT acquisition in lines across the dike with 0.5 m electrode spacing. y [m] measured overground, blocks are 0.5 m squares. The black triangles are where the test dike attaches to the basin wall. The red numbers indicate the ERT line numbers. Most of the ERT electrodes on the downstream side were also used for SP measurements. Therefore the checkerboard pattern in the piping experiment ERT acquisition design.

ERT and SP electrodes would be the same however. But in this proof of concept, ERT was performed over the entire dike, such that the resistivity model would not limit the interpretation of the SP data. [Figure A-5](#) is a photo of the upstream side of the dike, taken during ERT acquisition prior to the piping experiment.

The ERT inversion was performed using the FreeCAD \rightarrow Gmsh \rightarrow pyGIMLi workflow presented in [chapter 4](#). Here pyGIMLi was only used to prepare the mesh and data for use in BERT. The inversion itself was then done in BERT ([Günther et al., 2006](#); [Rücker et al., 2006](#), Boundless electrical resistivity tomography), which is a versatile 3D ERT modeling and inversion open-source software package. The mesh used for inversion of the data acquired prior to the piping experiment is shown in [Figure A-6](#).

In an ERT inversion the resistivity of each elements inside the inversion region of the mesh is optimized iteratively, until a model is found, that explains the field data as accurately as possible. Such an inversion problem is solved in BERT by minimizing the L2-norm of the weighted residual between field data and model response. This least squares minimization problem is strongly underdetermined, since there are many more unknowns than data. Where the unknowns are the resistivities of the elements inside the inversion region of the mesh and the data are the apparent resistivities. To overcome the ill-posedness of the inversion problem regularization is applied. Regularization is included in the objective function as the L2-norm of the difference between a starting model and the inversion model, weighted by a constraints matrix. This L2-norm is then multiplied by a factor λ , which is the regularization strength. The complete L2-norm objective function is minimized in BERT with the Gauss-Newton scheme. The objective function can be written as:

$$\Phi = \Phi_d(\mathbf{m}) + \lambda\Phi_m(\mathbf{m}) = \|\mathbf{D}(\mathbf{d} - \mathbf{f}(\mathbf{m}))\|_2^2 + \lambda \|\mathbf{C}(\mathbf{m} - \mathbf{m}^0)\|_2^2, \quad (5-2)$$

$$\|\mathbf{D}(\mathbf{d} - \mathbf{f}(\mathbf{m}))\|_2^2 = \sum_{i=1}^N \left| \frac{d_i - f_i(\mathbf{m})}{\epsilon_i} \right|^2, \quad (5-3)$$

$$\mathbf{D} = \text{diag}(1/\epsilon_i), \quad (5-4)$$

where:

$\Phi_{(d,m)}$	total, data, regularization objective functions	λ	regularization strength
\mathbf{m}	model vector, resistivity of each element	\mathbf{m}^0	starting model vector
\mathbf{d}	data vector, apparent resistivities	$\mathbf{f}(\mathbf{m})$	model response
ϵ_i	error of apparent resistivity i	\mathbf{C}	constraints matrix
N	number of data, apparent resistivities		

Usually the constraints matrix \mathbf{C} is an identity matrix, but can be changed to a diagonal matrix prescribing a weight to each model resistivity. In such a way regularization can also be controlled locally, on top of controlling it with the regularization strength λ . The data error ϵ_i is the standard deviation in the apparent resistivity of 3 to 6 repeated measurements on the same quadruple. In that way the error in every measurement was estimated. The default starting model \mathbf{m}^0 in BERT is a homogeneous resistivity model of the mean apparent resistivity. Alternatively a starting model can be provided.

Besides the default L2-norm objective function, BERT can also minimize a L1-norm objective function to arrive at a resistivity model based on ERT data. The minimization of a L1-norm objective function is also known as a least absolute deviations minimization problem. Minimizing a L1-norm objective function gives a more robust inversion result, because the difference between data and model is not squared as is the case in a L2-norm objective function. However, the resistivity model obtained from a L1-norm inversion is more smooth than a L2-norm resistivity model, because of the same reason, which is the main disadvantage of using a L1-norm objective function.

There are several quality measures to quantify the result of the inversion. Two common quality measures are the root mean square error (RMS) and the χ^2 . The value of the RMS should be close to the data error. The optimal value for χ^2 is 1.00. Another quality measure is the cumulative sensitivity distribution. It is calculated as change of apparent resistivity [Ωm] over change in model resistivity [Ωm], summed over the model elements. In other words, the Jacobian summed over the model elements. Consequently, each model element in the sensitivity distribution contains a value that represents how sensitive the resistivity of that model element is to changes in the data, i.e. apparent resistivity.

Preliminary fieldwork

During the preliminary fieldwork the SP measurements were done on a grid with a 1 m spacing measured overground. Given that 144 electrodes could be connected to the Syscal Pro measurement system, a smaller electrode spacing was chosen close to the exit hole and downstream current injection electrode, see [Figure 5-6](#). The extra electrodes around the exit hole were electrodes that were also used during the ERT measurements. SP data was acquired by measuring the potential difference between each of the 144 field electrodes and each of the 2 reference electrodes. The non-polarizable field electrode (62) was positioned at 3.5 m upslope from the toe of the test dike. The polarizable and non-polarizable reference electrodes were put at a distance of approximately 300 m from the test dike.

To get an idea of signal drift, SP data were acquired without current injection over the course of several hours. To determine the sensitivity of the monitoring system, the streaming potential was simulated by injecting a DC current between the inlet and exit hole, again see

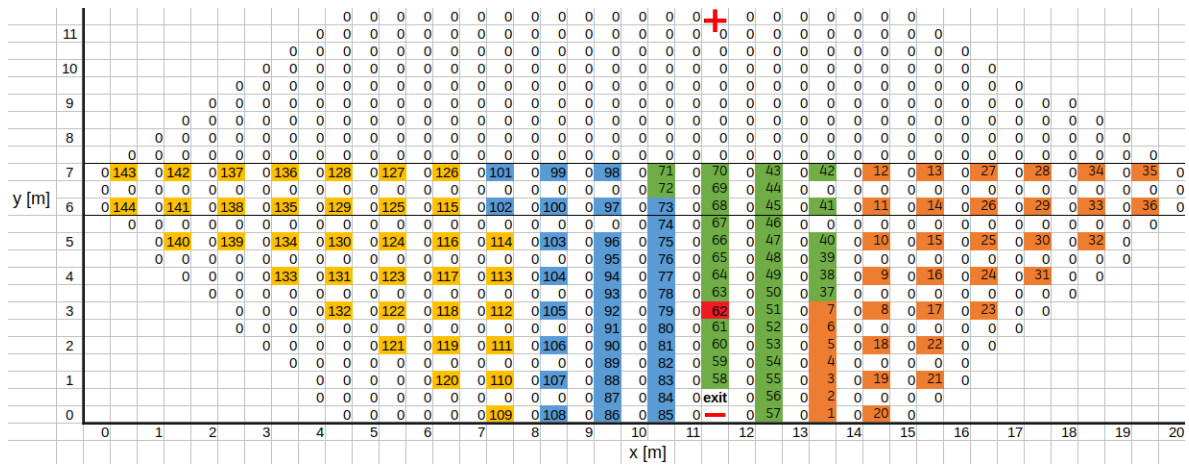


Figure 5-6: Top view of SP acquisition design during preliminary fieldwork. y [m] measured overground, blocks are 0.5 m squares. The numbers indicate the electrode number. Orange: multi-core cable 1, electrodes 1-36; green: cable 2, elec 37-72; blue: cable 3, elec 73-108; yellow: cable 4, elec 109-144. Red electrode 62 was the Cu-CuSO₄ electrode. The red + and - are the positions of the DC current injection electrodes.

Figure 5-6. A potential difference of 12, 6, 3 and 1.5 V was applied between the 2 current injection electrodes for the duration of 18 minutes with 12 minute intervals. At the same time the SP between field and reference electrodes was measured every 6 minutes. Resulting in 3 data points during current injection and 2 data points in between current injection.

Note that the positive self-potential anomaly would be measured on the downstream side of the dike, and the negative anomaly on the upstream side of the dike. The positive and negative poles were unfortunately mixed up during the preliminary fieldwork. This did however not hamper the sensitivity determination of the SP monitoring system. The only difference is that the polarity of the signal was inverted, because of the incorrect polarity of the injection current.

SP monitoring during piping experiment

Figure 5-7 is a top view of the SP acquisition design used during the piping experiment. A similar grid as during the preliminary fieldwork was used. A grid with a 1 m spacing measured overground with extra electrodes around the exit hole. More space was needed around the exit hole, such that the bucket around the exit hole could be installed and there was space to work. i.e. space to monitor flow rate through the v-weir and scoop up sand with the tea spoon. Therefore fewer electrodes were placed very close to the exit hole, compared to the preliminary fieldwork. Besides that, the extra electrodes close to the exit hole were put in a checker board pattern w.r.t. the electrodes in the 1 m spaced grid. This was done to get a better spatial coverage of SP data.

The non-polarizable field electrode (120) was again positioned at 3.5 m upslope from the toe of the test dike. The polarizable and non-polarizable reference electrodes were again put at a distance of approximately 300 m from the test dike. During both the null-measurement on 6 September 2019 and the piping experiment on 7 September, the SP was measured every 3 minutes.

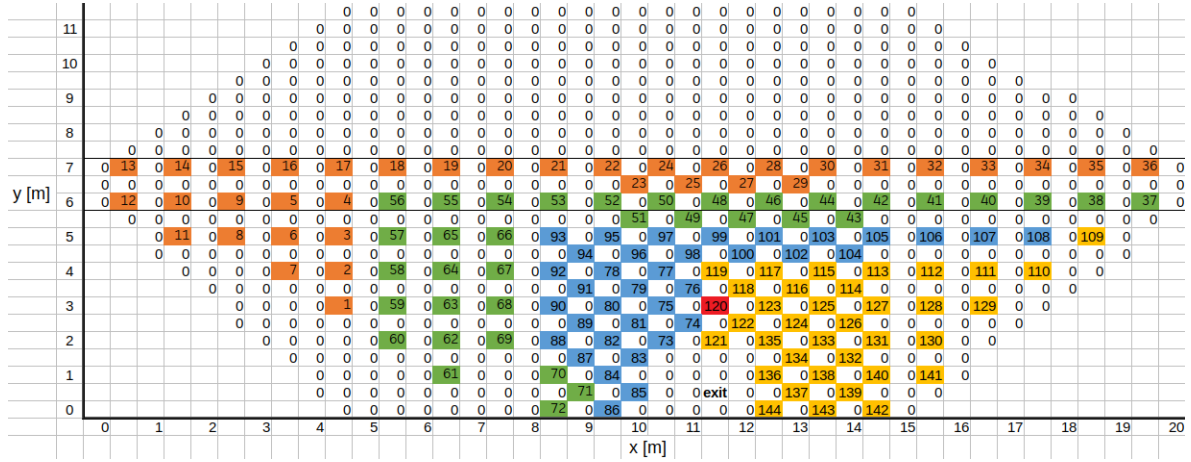


Figure 5-7: Top view of SP acquisition design during the piping experiment. y [m] measured overground, blocks are 0.5 m squares. The numbers indicate the electrode number. Orange: multi-core cable 1, electrodes 1-36; green: cable 2, elec 37-72; blue: cable 3, elec 73-108; yellow: cable 4, elec 109-144. Red electrode 120 indicates the Cu-CuSO₄ electrode.

5-3 Results

5-3-1 Piping experiment

The second piping experiment on channel ② was initiated at 9:45 in the morning on 7 September 2019, by raising the water level in the upstream basin by 20 cm. Which was just enough so that water could enter the slanted pipe. The entry pipe and exit hole of channel ① were closed off. Subsequently the water level was increased in steps of approximately 20 cm until the water level was 85 cm at 15:00 and a small amount of water started flowing. Approximately 7.2 liter per hour. Piping phase 1: seepage.

From that point on the water level was raised in steps of 10 cm. At 18:15 the water level was 125 cm and half an hour later the first sand was detected in the bucket. Unfortunately the water in the bucket was too turbid to see the sand. However, when reaching to the exit hole with one's hands, one could feel a small amount of sand around the exit hole that had not been there previously.

Sand coming out of the exit hole meant that the equilibrium stage of backward erosion had started. Piping phase 2: backward erosion. At 19:35 the pressure readings of all piezometers stabilized, meaning that no more erosion was taking place. At this point the flow rate was approximately 18 liter per hour. For erosion to continue the water level needed to be increased. 10 cm was added. After that more sand was coming out, but the flow rate stayed almost the same. At 21:45 the pressures stabilized again and the water level was raised by another 10 cm. The flow rate increased to 28 liter per hour. After this increase in water level, the pressures did not stabilize anymore. That indicated that the progressive stage of backward erosion had started.

After 23:45 the downstream slope was visibly wet due to seepage through the core of the test dike. The top of the test dike was very dry at the start of the experiment. Cracks in the dry

clay cover must have allowed the water seep into and through the core of the test dike.

At the transition between the regressive and progressive stages of backward erosion, the critical head was 0.9 m, after compensating for entrance losses. During the first piping experiment the critical head was 1.15 m. The progression rates during the first and second experiments were 7.8 m/day and 18 m/day respectively. Both indicating that backward erosion piping goes faster after the first time it occurs. However, the sand bed did recover partially, because a pipe did have to develop again during this second experiment.

5-3-2 Self-potential

Electrical resistivity tomography

The inversion result of the dipole-dipole data obtained prior to the piping experiment is shown in [Figure 5-8](#) and a slice through this resistivity model in [Figure 5-9](#). The sensitivity distribution of the inversion is included in the appendix together with the inversion result of the preliminary fieldwork ERT data and the sensitivity of that inversion, [Figure A-7](#) to [Figure A-11](#).

Neither of the two ERT data sets contained negative apparent resistivities. However, both did contain large outliers. Therefore, apparent resistivities above 1200 Ωm were disregarded for the preliminary fieldwork data and apparent resistivities above 800 Ωm were disregarded for the piping experiment ERT. The cut-offs were determined based on a apparent resistivity histogram.

Even with the filtered data, the inversion result gave bad results using an L2-norm inversion. This was also the case with a high regularization strength. Therefore, inversion of both data sets was done in 2 separate steps:

1. L1-norm inversion with an upper bound on the model resistivity of 600 Ωm . Without the upper bound there were still a few elements with excessively high resistivities, while the aim of the first step was to make a smooth first guess of the dike resistivity.
2. L2-norm inversion with the L1-norm inversion result as starting model. Additionally the regularization strength was moderately large on the first iteration and then reduced by 0.8 in every subsequent iteration. Again upper bounds on the model resistivity were needed to make sure resistivities stayed within a feasible range. 900 Ωm for the piping experiment ERT inversion and 1100 Ωm for the preliminary fieldwork ERT inversion.

The main reason for the high RMS and χ^2 is thought to be caused by incorrect geometric factors. This because the location of the electrodes in the mesh was determined based on the CAD model of the test dike and the acquisition grid measured overground. Therefore, the locations of the electrodes in the field and in the model did not match perfectly, because the CAD model is not an exact representation of the geometry of the test dike. Where inaccuracies in the construction and subsidence of the dike are possible causes of the differences between the CAD model and the actual geometry of the dike.

Even though the inversion quality measures are not close to their ideal values, the resistivity models do align with observations in the field and prior information about the geometry of the dike. Both the resistivity models from the preliminary fieldwork and from the piping

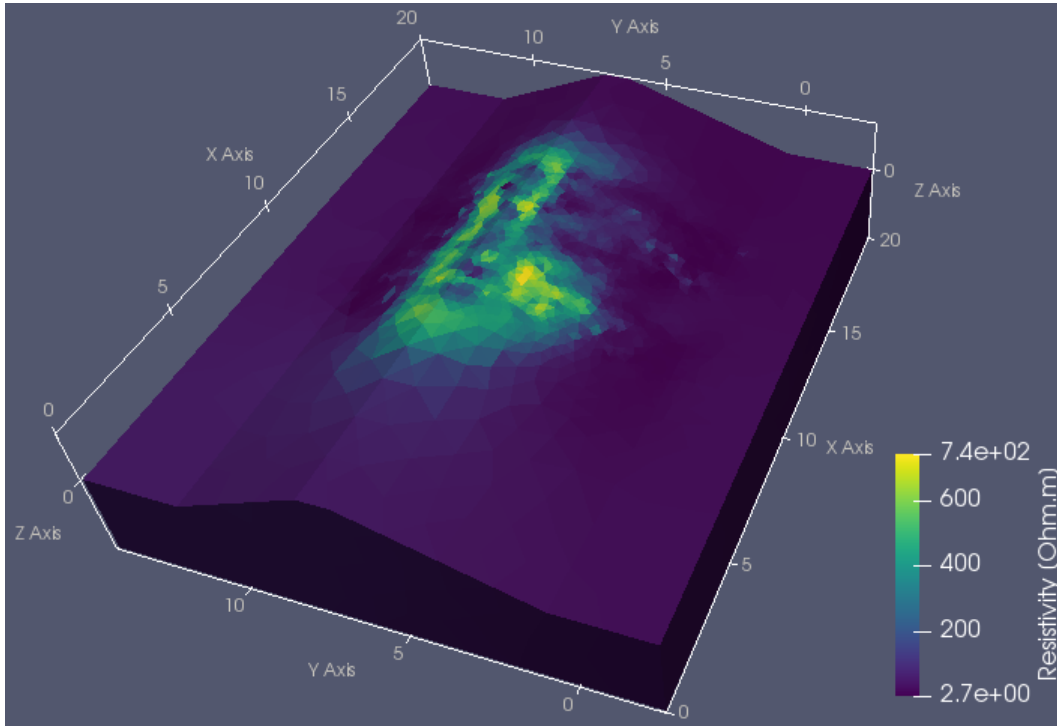


Figure 5-8: 3D resistivity model obtained through simultaneous inversion of dipole-dipole data obtained prior to the piping experiment. 2 step inversion parameters and statistics: (a) L1-norm inversion with an upper bound on the resistivity of 600 Ωm . 20 iterations; RMS = 161%; $\chi^2 = 2.81$ (b) L2-norm inversion with the L1-norm inversion result as starting model; a decrease in regularization strength of 0.8 at every iteration and an upper bound on the resistivity of 900 Ωm . 3 iterations; RMS = 88.1%; $\chi^2 = 93.2$.

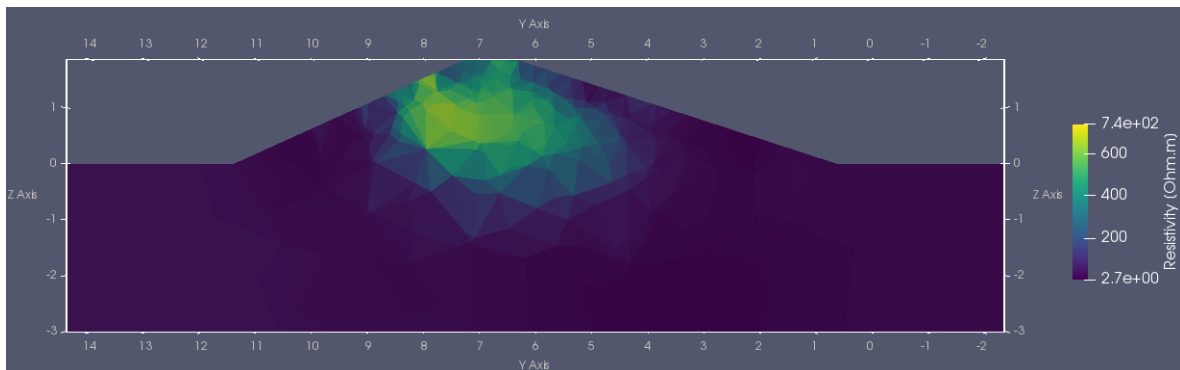


Figure 5-9: Slice through the resistivity model that was the outcome of the inversion of dipole-dipole data obtained prior to the piping experiment. Slice through the exit hole at $x = 11.5$ m.

experiment show higher resistivities at the top and core of the dike. The core of the dike was made of sand and the dike was very dry at the top. Both of these factors give rise to a high resistivity compared to wet clay which is found at the toes of the dike. Additionally a high resistivity anomaly at $x \approx 10$ m at the top of the downstream slope is visible in the piping

experiment resistivity model. That high resistivity anomaly matches the 3 m wide sand strip in the middle of downstream slope, see [section 5-1](#).

Preliminary fieldwork

[Figure 5-10](#) shows the SP relative to the first measurement, obtained for non-polarizable Cu-CuSO₄ field electrode 62 during the preliminary fieldwork, see [Figure 5-6](#) for the SP acquisition design. By displaying the data relative to the first measurement, the time dependent variation in the SP signal was visualized. The plot in [Figure 5-10](#) contains three data sets. The blue data set represents the potential measured between field electrode 62 and the polarizable reference electrode. The orange data set represents the potential measured between field electrode 62 and the non-polarizable Cu-CuSO₄ reference electrode. The third data set is the SP measured between field electrode 62 and the polarizable reference electrode, compensated for the drift of the polarizable reference electrode. More about this drift compensation below.

The DC potential difference applied across the dike is clearly visible in the data of electrode 62. The steps in the measured SP were the signal, any deviation from 0, when there was no DC current injection, was therefore considered drift. The total drift is the sum of the drift in the field and reference electrodes. Hence the non-polarizable field and reference electrodes display very little drift (orange). These electrodes were therefore considered stable and no drift compensation was deemed necessary. The polarizable reference electrode on the other hand does display significant drift (blue). Over the course of the four and a half hour experiment, the polarizable reference electrode experienced a drift of about -20 mV. Linear drift compensation for the polarizable reference electrode was therefore proposed.

The difference between the measurements w.r.t. the polarizable (blue) and non-polarizable reference electrodes (orange) was taken. Subsequently linear regression analysis was performed on the difference of these data, to arrive at a linear drift model for the polarizable reference electrode, see [Figure 5-11](#). Subtracting the drift compensation from the data measured w.r.t. the polarizable reference electrode (blue) gave the green data in [Figure 5-10](#), which shows a good match with the data measured w.r.t. the non-polarizable reference electrode.

As mentioned above the total drift is the sum of the drift of the reference electrode and the field electrode. A linear drift model was obtained for the polarizable reference electrode. In a similar fashion linear drift compensation was proposed for the field electrodes. [Figure 5-12](#) shows the data obtained for field electrode 94. The data measured w.r.t. the non-polarizable electrode (orange) and drift compensated data (green) suggest that the drift of field electrode 94 could be approximated with a linear model. The drift caused by polarizable field electrode 94 could be approximated with a linear drift of about +40 mV over the course of the four and a half hour experiment. However, for some field electrodes a linear drift model would not have sufficed, such as for electrode 70 shown in [Figure 5-13](#). Furthermore, some field electrodes showed very large, unexplainable drift and the DC current injection did also not show up on the time series for these electrodes, e.g. electrode 133 [Figure 5-14](#).

[Figure 5-15](#) shows a top view of the SP distribution when applying a 12 V DC potential difference across the dike. The SP distribution was visualized relative to the measurement right before the injection of the 12 V current. In that way the effect of the current injection on the SP field was visualized without field electrode drift disturbing the visualization. The

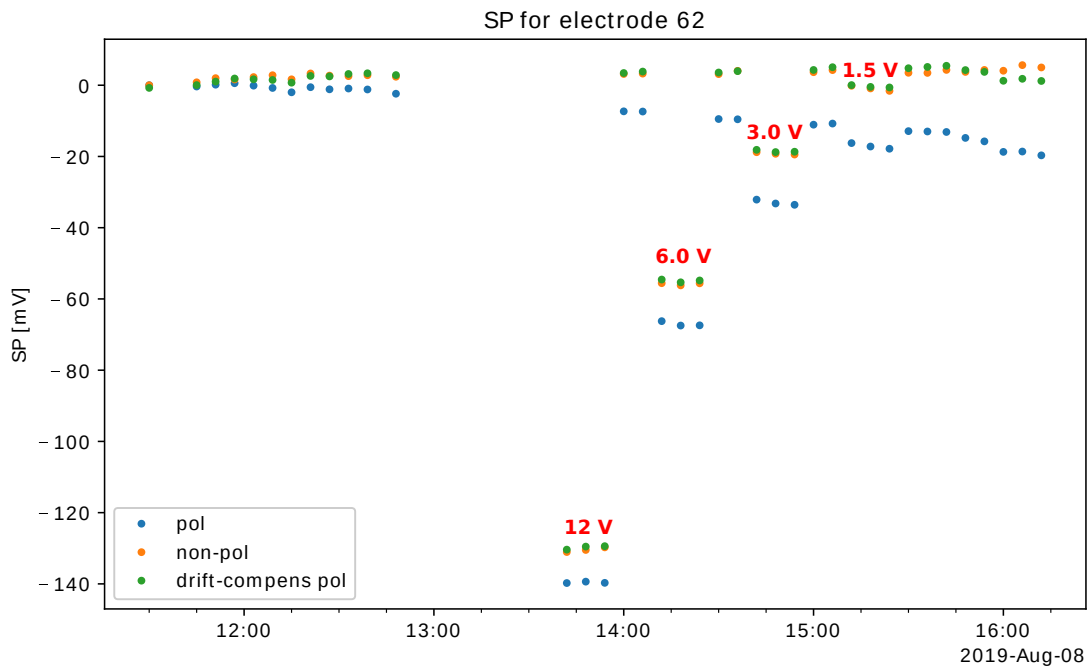


Figure 5-10: SP relative to the first measurement, obtained for non-polarizable Cu-CuSO₄ field electrode 62 during the preliminary fieldwork, measured w.r.t. the polarizable and non-polarizable Cu-CuSO₄ reference electrodes. Compensated data was measured w.r.t. the polarizable reference electrode, compensated for the drift of the polarizable reference electrode using a linear drift model.

SP distribution due to the injection of a 1.5 V DC current was visualized in a similar manner in Figure 5-16.

Comparing the SP distributions resulting from 12 V and 1.5 V current injection, two things stand out. The first is that the SP distribution during the 12 V injection is much smoother than the SP distribution during 1.5 V injection. The smoothness of the SP distributions during 6 and 3 V injection lay in between the SP distributions in Figure 5-15 and Figure 5-16, both in terms of signal strength and distribution smoothness. The reason for this difference is that, the lower the injection current, the smaller the signal strength and hence the larger the relative influence of drift in the measured SP.

The second thing that stands out is that not all electrodes pick up the SP signal due to current injection across the dike. Electrodes 1 to 7 at $x = 13$ m and electrode 133 for example, do not show an SP signal during any of the current injections. The reason for this is unknown.

Based on the SP distribution during 1.5 V injection and SP time series for single electrodes (e.g. Figure 5-10 and 5-12), the sensitivity of the measurement setup was considered 3 mV. Such a sensitivity can however only be obtained during monitoring when the drift can be removed accurately. Otherwise the signal and drift cannot be differentiated from each other. Especially given that the a realistic SP signal would not display such an abrupt change in SP, as is the case when switching on a current source. On the contrary, the SP signal during the piping experiment is expected to increase slowly together with the amount of water flowing out of the dike. Which would make it harder to distinguish drift from signal. In order to be able

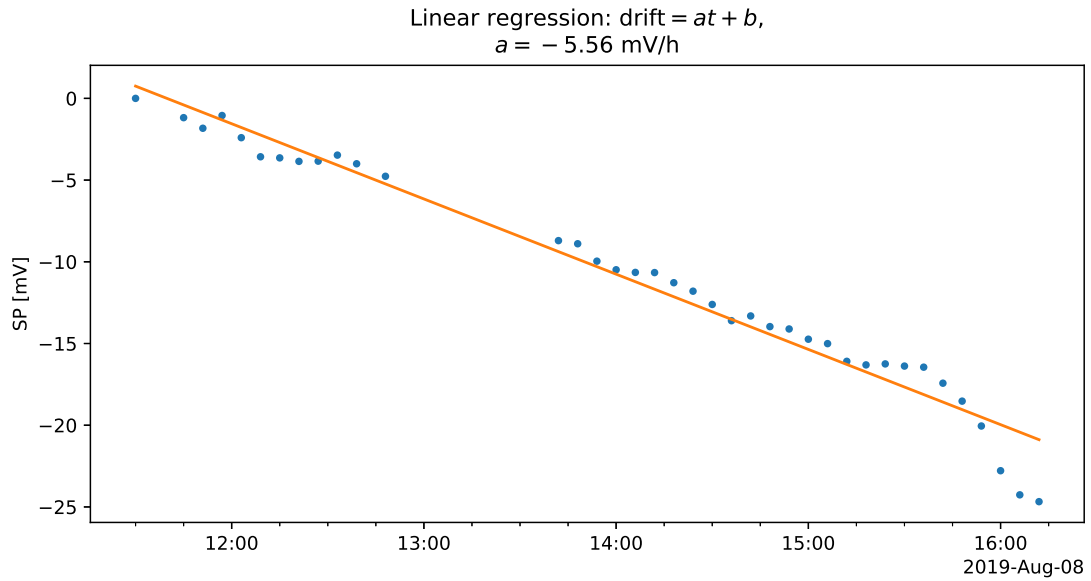


Figure 5-11: Linear drift compensation model for the polarizable reference electrode. The drift model was the result of linear regression on the difference between SP measured with electrode 62 w.r.t. the polarizable reference electrode and the SP measured with electrode 62 w.r.t. the non-polarizable reference electrode.

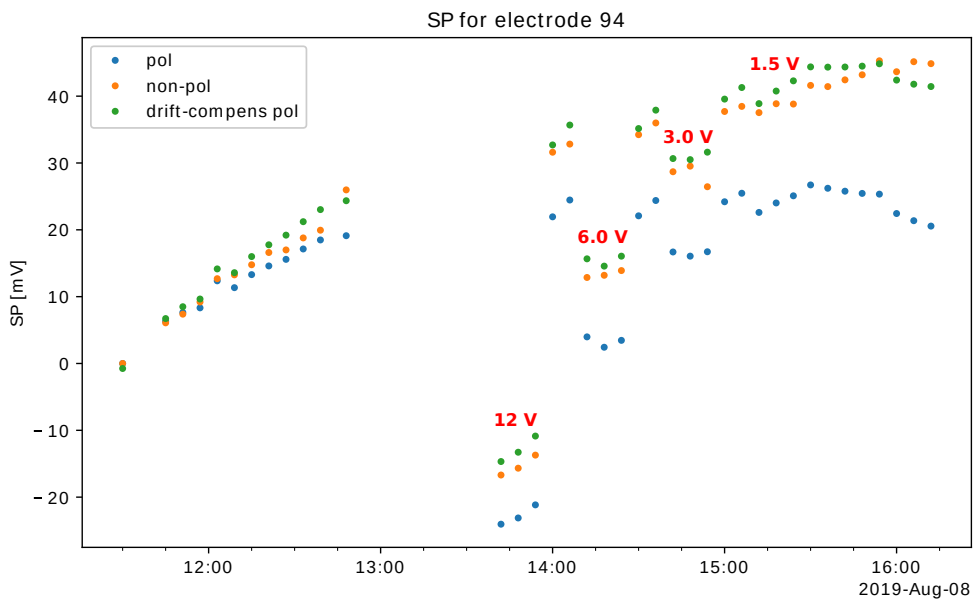


Figure 5-12: SP relative to the first measurement, obtained for polarizable electrode 94 during the preliminary fieldwork, measured w.r.t. the polarizable and non-polarizable Cu-CuSO_4 reference electrodes. The drift of the polarizable reference electrode was compensated using a linear drift model.

to distinguish between drift and signal during the piping experiment, the null-measurement also served as a means to find a drift model for every electrode.

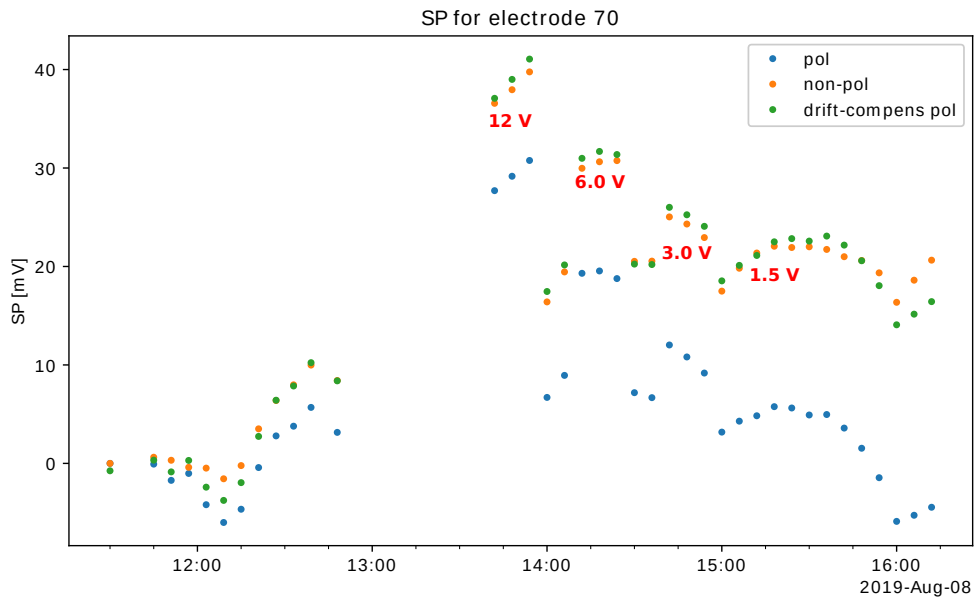


Figure 5-13: SP relative to the first measurement, obtained for polarizable electrode 70 during the preliminary fieldwork, measured w.r.t. the polarizable and non-polarizable Cu-CuSO_4 reference electrodes. The drift of the polarizable reference electrode was compensated using a linear drift model.

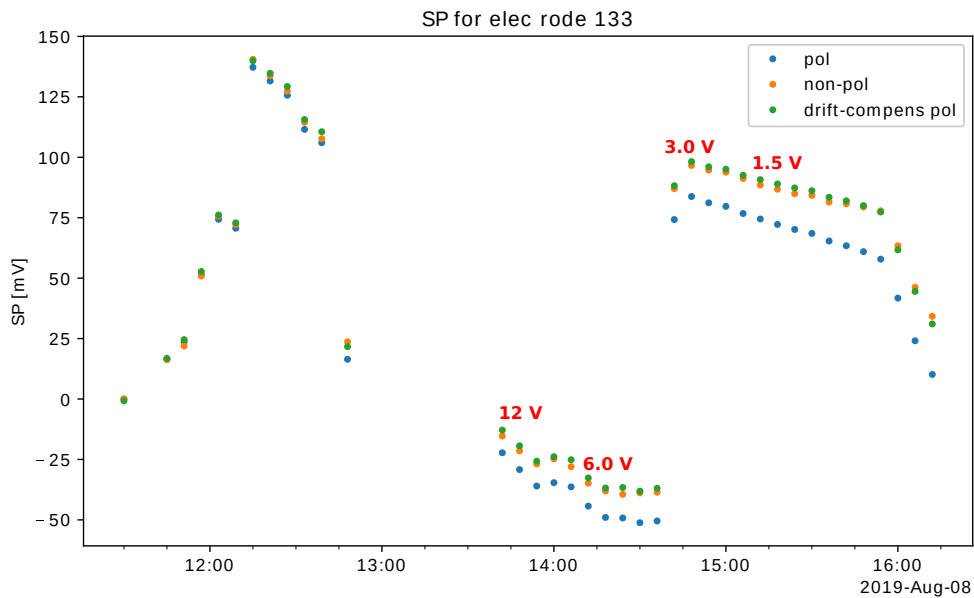


Figure 5-14: SP relative to the first measurement, obtained for polarizable electrode 133 during the preliminary fieldwork, measured w.r.t. the polarizable and non-polarizable Cu-CuSO_4 reference electrodes. The drift of the polarizable reference electrode was compensated using a linear drift model.

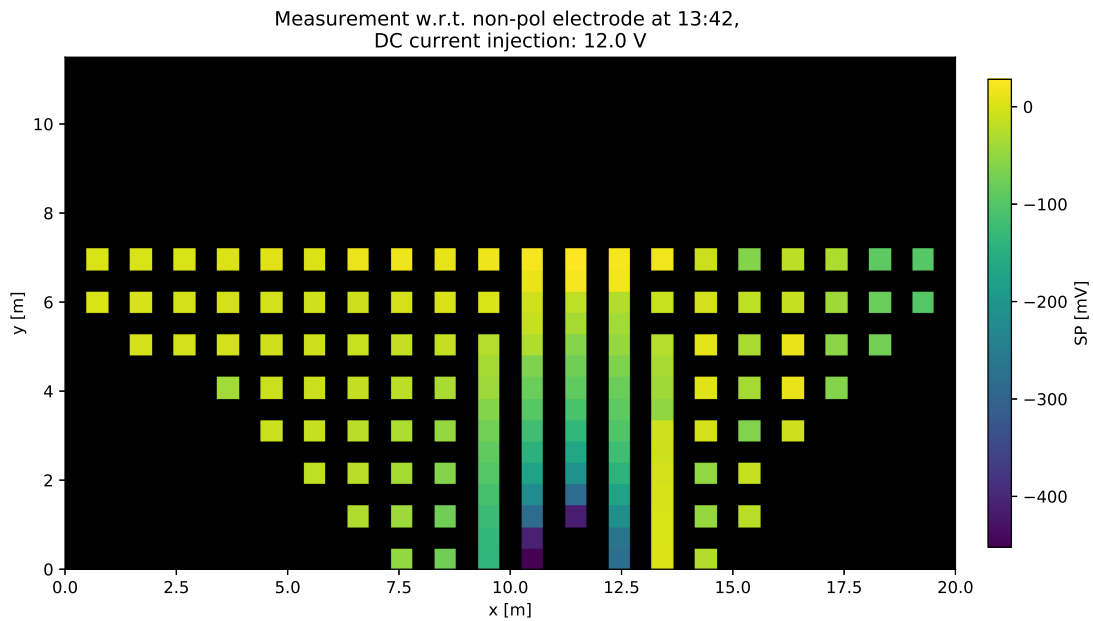


Figure 5-15: SP distribution relative to the measurement before switching on the 12 V DC current.

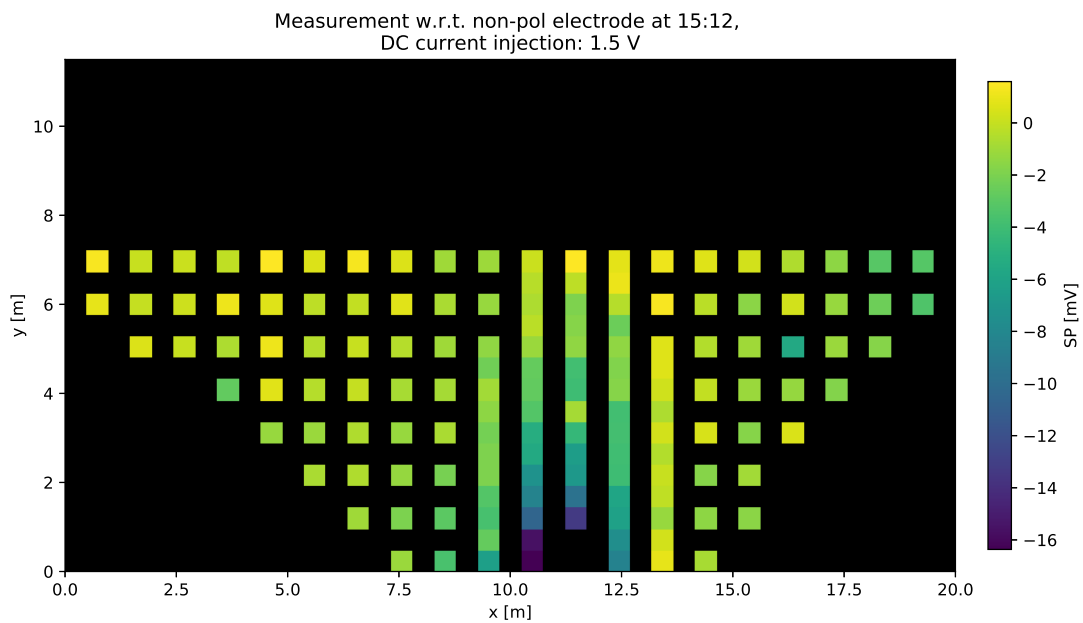


Figure 5-16: SP distribution relative to the measurement before switching on the 1.5 V DC current.

SP monitoring during piping experiment

During the piping experiment electrode 120 was the non-polarizable Cu-CuSO_4 field electrode, see Figure 5-7. Figure 5-17 shows the SP measured with electrode 120 during the

null-measurement and the piping experiment, both w.r.t. the polarizable (blue) and non-polarizable (orange) reference electrodes. The data is again represented relative to the first measurement, because the time dependent variation was of interest. The null-measurement was started at 8:00 on 2 September 2019 and continued until 8:20 on 3 September 2019. Then the Cu-CuSO₄ electrodes were refilled with copper(II) sulfate and the measurement system was turned on again. At 9:45 the piping experiment was started by raising the water level in the upstream basin with 20 cm. During both the null-measurement and the piping experiment, the SP was measured every 3 minutes.

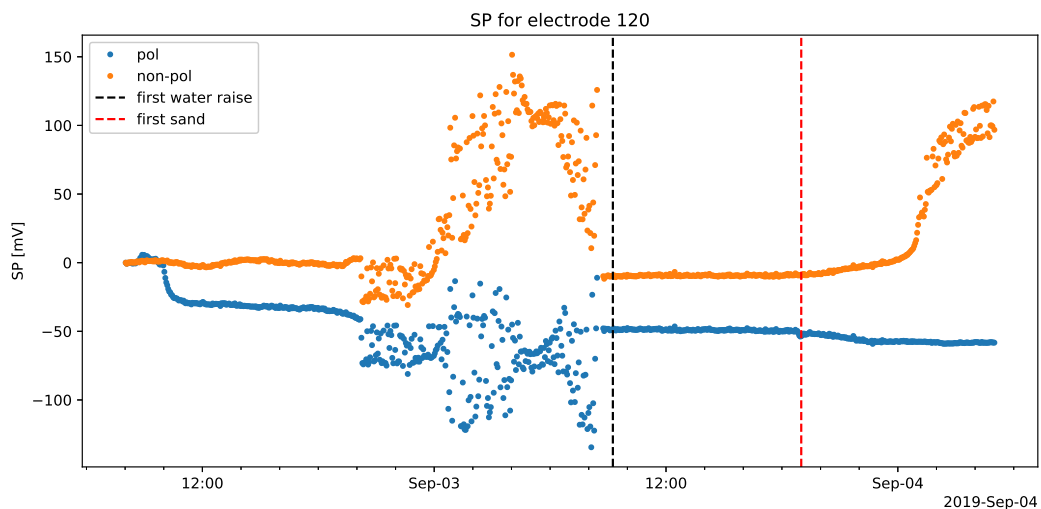


Figure 5-17: SP relative to the first measurement, measured with non-polarizable Cu-CuSO₄ field electrode 120 w.r.t. the polarizable and non-polarizable reference electrodes. Null-measurement from 8:00 02-09 to 8:20 03-09. The piping experiment started at 9:45 on 03-09.

The data obtained with electrode 120 show very strong drift after 20:00 on 02-09 (both orange and blue) and after 1:00 on 04-09 (only orange). Recall that drift in the data is the sum of the drift of the field and reference electrodes. With this in mind, it is possible to tell which electrodes caused this strong drift, by comparing the data obtained with electrode 120 with data obtained with another field electrode, e.g. electrode 87 (Figure 5-18).

The orange data of electrode 87 shows strong drift after 23:00 on 02-09 and again after 1:00 on 04-09. This drift is not visible in the blue data, meaning that it was caused by the non-polarizable reference electrode. Similar strong drift signatures are visible in the orange data of electrode 120, confirming that the non-polarizable reference electrode was the cause of this strong drift. Subsequently comparing the blue and orange data of electrode 120, leads to the conclusion that non-polarizable field electrode 120 was the cause of the drift after 20:00 on 02-09. And indeed the first strong drift signature in the orange data of electrode 120 can be seen as the sum of the strong drift caused by the non-polarizable reference electrode and the strong drift caused by non-polarizable field electrode 120. In summary, the non-polarizable reference electrode caused strong drift both during the null-measurement and during the piping experiment. Non-polarizable field electrode 120 caused strong drift during the null-measurement only.

The above described strong drift of the non-polarizable electrodes started when all the CuSO₄

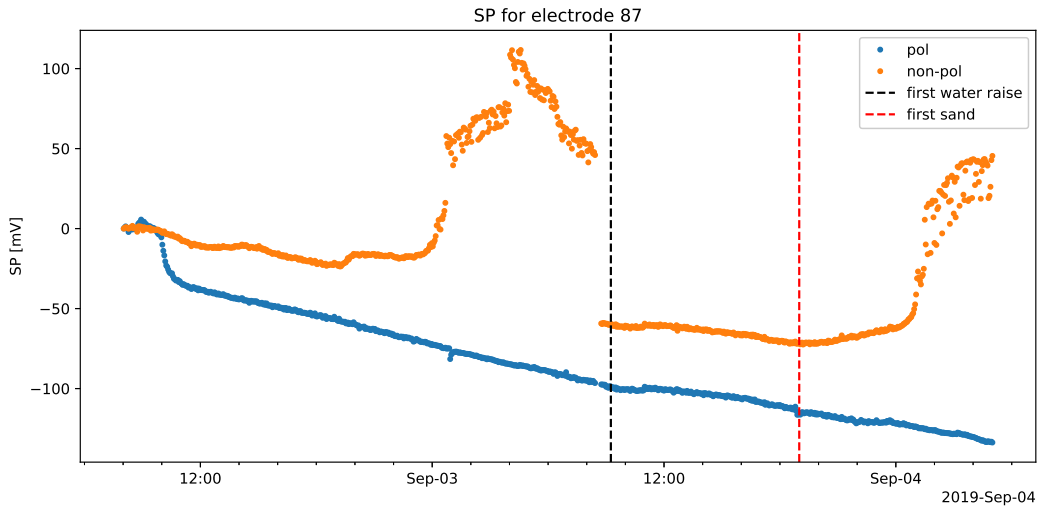


Figure 5-18: SP relative to the first measurement, measured with field electrode 87 w.r.t. the polarizable and non-polarizable reference electrodes. Null-measurement from 8:00 02-09 to 8:20 03-09. The piping experiment started at 9:45 on 03-09.

had leaked out. After refilling the non-polarizable electrodes in the morning of 3 September, right before starting the piping experiment measurements, the SP came back to its normal levels again. When thinking away the first bump in the orange data of e.g. electrode 87, the orange line would be continuous. During the piping experiment only the non-polarizable reference electrode became empty. Much less CuSO_4 leaked out of non-polarizable field electrode 120. The reason for this is that water was seeping through the core of the dike, the downstream slope of the dike was visibly wet after 23:45. With the water seeping through the core of the dike, the soil around the non-polarizable field electrode was saturated, resulting in less CuSO_4 leaking out.

Concerning the drift of the polarizable reference and field electrodes the following observations were made. Firstly, the drift of the polarizable reference electrode was minimal after the 30 mV SP drop in the first two and a half hours of the null-measurement. Secondly, assuming linear drift of field electrodes is justifiable for several field electrodes, as is the case for field electrode 87. Thirdly, data such as obtained with field electrode 52 (Figure 5-19), suggest that a piecewise linear drift model could be employed to compensate for the electrode drift. However, the drift signature during the null-measurement was not repeated during the piping experiment. Hence distinguishing signal and drift would still be non-trivial. Lastly, a few electrodes showed drift without coherence. In other words, drift that could not be approximated with an electrode drift model, see Figure 5-20.

In order to evaluate if the onset of fluid flow through the sand channel underneath the test dike and subsequent piping were visible in the SP data, two things were looked at. Firstly, SP data were compared with events during the piping experiment. Increases in fluid flow through and sand production from the sand channel were looked at, as well as how the SP developed after water was seen seeping through the core of the dike. An increase in SP was expected due to these events, given that the electrodes were placed on the downstream side of the dike. Secondly, the data was examined to find spatial correlation in the development

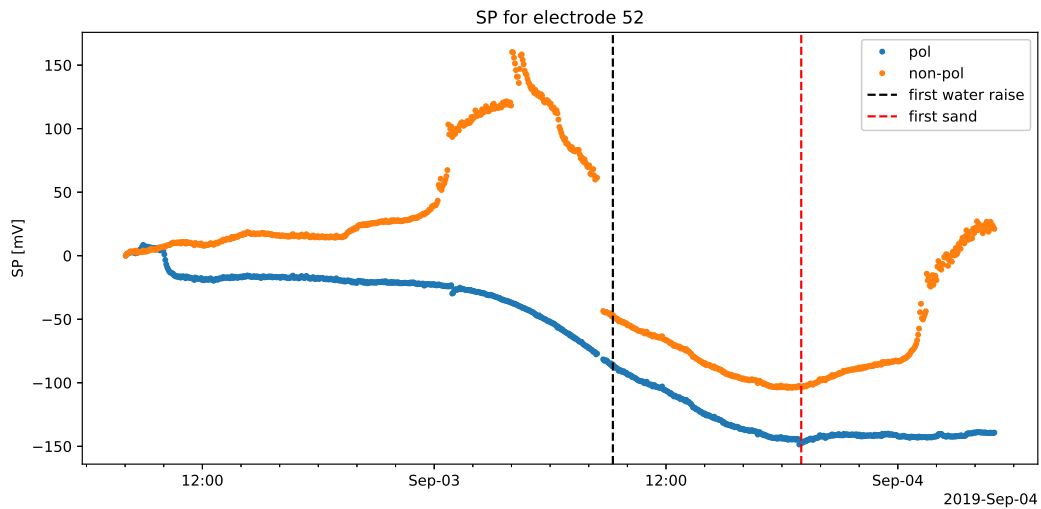


Figure 5-19: SP distribution relative to the measurement before switching on the 1.5 V DC current.

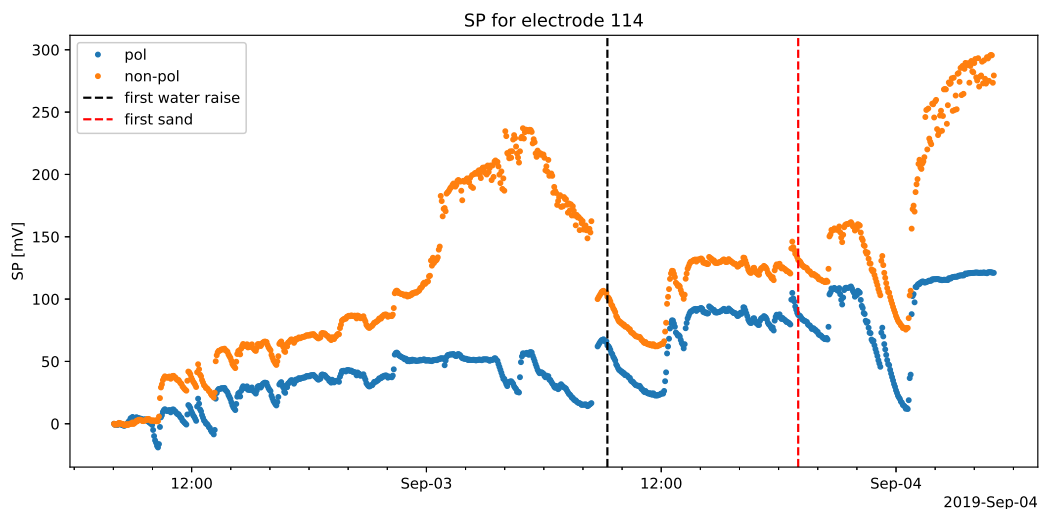


Figure 5-20: SP distribution relative to the measurement before switching on the 1.5 V DC current.

of the SP during the piping experiment.

No match between the piping experiment events and the expected increase in SP was found. To substantiate this, the data obtained during the piping experiment, with non-polarizable field electrode 120 were plotted in Figure 5-21. These data were considered most reliable, because the non-polarizable electrodes showed least drift, before being empty. Given that the expected increase in SP was not observed, neither flow through the sand channel, nor piping, nor seepage through the core of the dike were detectable with the used measurement setup.

Spatial correlation in the development of the SP during the piping experiment was also not found. Electrode drift dominated the changes in SP measured. Similarly the drop in SP

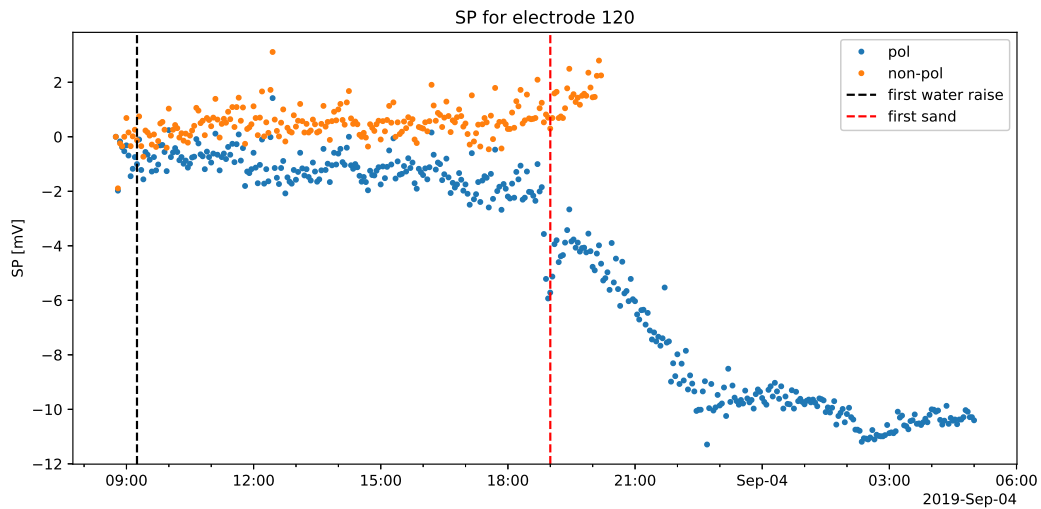


Figure 5-21: SP relative to the first measurement during the piping experiment, measured with non-polarizable Cu-CuSO_4 field electrode 120 w.r.t. the polarizable and non-polarizable reference electrodes. The strong drift in the data due to the empty non-polarizable reference electrode, were cut off.

measured with electrode 120 after the first sand was found around the exit hole, was not spatially correlated and therefore attributed to electrode drift.

As a last observation the 1 mV noise band in Figure 5-21 should be mentioned. Such a noise band of 1 mV is too large, given that the streaming potential measured during an Ijkdijk piping experiment had a reported maximum magnitude of about 3 mV (Rittgers et al., 2014).

Environmental impact of copper(II) sulfate

The copper(II) sulfate solution that was used in the non-polarizable electrodes, leaked out during the preliminary fieldwork and piping experiment. This section gives a very brief analysis of the environmental impact of the solution leaking into the environment. Copper(II) sulfate is used in agriculture as an artificial fertilizer, but is also used in pesticide products (*Copper(II) Sulfate* — *Encyclopedia.Com*, 2019). For the environmental impact analysis a 5 m radius, 2 m deep cylinder was taken as the region of influence. Where 5 m is the approximate distance from the non-polarizable electrode to the nearest surface water body. The solution was assumed to trickle down to the groundwater and influence the first 2 m of saturated soil, with a water content of 40%. This means that the total volume of groundwater considered was 63 m^3 . This was considered a conservative estimation. Firstly, because the copper will adhere to clay minerals, thereby decreasing the short term environmental load on the groundwater. Secondly, because the water volume to consider would be much larger when the solution reaches the surface water. A larger volume means a smaller environmental load.

Verweij, Boumans, Claessens, and Lijzen (2017) gives the Dutch drinking water norm for dissolved copper of $2000 \mu\text{g/l}$ and a background concentration for copper in the Netherlands of $8.8 \mu\text{g/l}$. For sulfate Brand, Baars, Verbruggen, and Lijzen (2008) lists a WHO (world health organization) limit of 400 mg/l and RIVM (rijksinstituut for public health and the

environment) and European limits of 250 mg/l. However the RIVM uses a guideline concentration of 100 mg/l. Additionally a map of SO_4^{2-} background concentrations is given, stating a concentration of 15 - 20 mg/l around Delft.

The concentration of copper(II) sulfate pentahydrate ($\text{CuSO}_4 \cdot 5\text{H}_2\text{O}$) in the electrolyte solution poured into the non-polarizable electrodes was 350 g/l = 1.4 mol/l. Equivalent to a Cu^{2+} concentration in the electrolyte solution of 89 g/l and the SO_4^{2-} concentration in electrolyte solution of 135 g/l. During the experiments 70 ml of copper(II) sulfate solution leaked out each day, so in total 70 ml leaked away during the preliminary fieldwork and another 140 ml during the piping experiment. This means that the concentration Cu^{2+} in the volume of influence increased from 8.8 $\mu\text{g}/\text{l}$ to 310 $\mu\text{g}/\text{l}$, which is a 3400% increase. And the concentration SO_4^{2-} increased from 15 mg/l to 15.4 mg/l, which is a 2.7% increase. See [Appendix B](#) for the complete calculations.

Concluding, the sulfate concentration does not rise significantly and also does not come close to RIVM, European or WHO limits. The copper(II) concentration in the direct vicinity does also not come close to RIVM limits. However, according to this conservative estimate, the concentration does increase significantly, by 3400% in the direct vicinity of the electrode.

5-4 Discussion and recommendations

The inversion of the ERT data, obtained during the preliminary fieldwork and prior to the piping experiment, showed that it is essential to know the electrode positions accurately. Given that the electrode positions in the field did not match the electrode positions in the inversion, the geometric factors were incorrect. As a consequence a 2 step L1-norm \rightarrow L2-norm inversion had to be applied, resulting in an oversmoothed resistivity model and a very large root mean square error in the inversion.

Contrary to what was expected, polarizable electrodes did not offer a reliable means of measuring SP. SP measurements during the preliminary fieldwork did point out that the monitoring system had a sensitivity of about 3 mV to sudden changes in the SP field, provided that the electrode drift was known accurately. However, there were also electrodes that did not show any response to changes in the SP field. Where the sudden changes to the SP field were induced by injecting DC current across the dike. Furthermore, accurately estimating the drift of polarizable electrodes consistently proved to be complicated. The drift of polarizable electrodes was highly variable from one electrode to another and could not be approximated by a linear, or piecewise linear drift model consistently.

The reason for the inferior stability of polarizable electrodes compared to non-polarizable electrodes was described in [subsection 3-2-4](#). The problem with polarizable electrodes is that there is direct contact between the metal and the electrolytes in the soil. On the other hand the contact between the metal and soil electrolytes in non-polarizable electrodes occurs in two separate steps. First there is the contact between the metal and an electrolyte solution of its own salt, e.g. Cu-CuSO₄ or Pb-PbCl₂. Then there is the contact between the electrode solution and the soil electrolytes. For both electrode types the largest potentials are associated with the metal-electrolyte contact. For non-polarizable electrodes this contact is stable, because the electrolyte concentration in the electrode solution is always the same. The

metal-soil electrolyte contact of polarizable electrodes is subject to change however. Hence the larger drift of polarizable electrodes.

The non-polarizable Cu-CuSO₄ indeed displayed much less drift, compared to the polarizable. However, once all the CuSO₄ had leaked out, the potentials measured by these electrodes became utterly unreliable. Therefore these electrodes need servicing, making them unsuitable for long term monitoring. Additionally it was demonstrated that the Cu²⁺ concentrations around the Cu-CuSO₄ electrodes increase a lot, due to the CuSO₄ that leaks out of them. On the short term the increase in Cu²⁺ concentration did not exceed drinking water limits, but when more than 2 Cu-CuSO₄ electrodes had been placed and CuSO₄ had been allowed to leak out over the course of weeks. Then the accumulation of Cu²⁺ could have exceeded drinking water limits. This is another reason that Cu-CuSO₄ electrodes are not suitable for the integration in a long term ERT and SP monitoring system.

Accordingly, for such an integrated long term ERT and SP monitoring system, a combination of stainless steel and Petiau (2000) lead-lead(II) chloride electrodes is recommended. The stainless steel electrodes are necessary for current injection during ERT measurements. The Petiau Pb-PbCl₂ have a better long term stability than Cu-CuSO₄ electrodes and do not need any servicing. Petiau electrodes are however not suitable for current injection as explained in subsection 3-2-4, but can be used to also measure the potential during ERT measurements.

The environmental impact of Petiau Pb-PbCl electrodes is minimal, because the Pb²⁺ cannot freely leak into the environment, like the CuSO₄ does when using Cu-CuSO₄ electrodes. The Pb²⁺ in Petiau electrodes is trapped in kaolinite and behind a wooden plate. The bentonite, into which Petiau electrodes should be installed (Figure A-4), further protects the environment from Pb²⁺ leaking into it. Given that bentonite is known to adsorb lead and other heavy metals (Uddin, 2017).

Additionally, the location of the Petiau reference electrode should be considered carefully. The reason being that the time dependent variation of the potential measured by the reference electrode differs from one place to the other. For example, the SP generated by rain water infiltration is not the same everywhere, because the soil differs from one place to the other. In addition to carefully considering the location of the reference electrode, one could opt to also install multiple Petiau reference electrodes.

Apart from the limitations regarding the use of polarizable and non-polarizable Cu-CuSO₄ electrodes, the used monitoring system also showed a relatively large noise band of approximately 1 mV, see Figure 5-21. This noise band around the SP trend was not understood well. However, given that this noise band was visible in data obtained with polarizable as well as non-polarizable electrodes, it was attributed to the used combination of the measurement system, multi-core cables and connectors. Such a noise band of 1 mV is too large, given that the streaming potential measured during an Ijkdijk piping experiment had a reported maximum magnitude of about 3 mV (Rittgers et al., 2014). Therefore, for future measurements a setup with a lower noise floor should be used.

The fact that neither the onset of flow through the sand channel nor piping were visible in the SP data, could have been predicted based on SP modeling and previous research reported in literature. SP modeling presented in chapter 4 underestimated the flow rate through the sand channel by a factor 3.5, but after correction for the higher flow rate in the field, the expected SP at the exit hole would have been no higher than 0.046 mV. SP signals that low, would

also not be measurable with conventional SP equipment. SP monitoring of piping during one of the Ijkdijk experiments showed a maximum SP anomaly of +3 mV at the downstream toe of the dike. This SP anomaly did however only show up, once large sand boils had formed. During the piping experiment on the test dike, flow rates were no higher than 28 liter per hour and sand boiling could only be detected by reaching to the bottom of the ring around the exit hole [Figure 5-3](#). Therefore, the SP signal associated with piping in the test dike must also have been lower than 3 mV. Prior to the field experiments, the model contained some errors, leading to an overestimation of the predicted SP signal. Also a sand boil large enough to be visible with the naked eye was expected, together with the associated higher flow rates and SP signal.

Concerning the applicability of SP monitoring to track the growth of a backward erosion pipe, this hypothesis is now considered too optimistic. Piping can be detected as a positive anomaly at the downstream toe of the dike as reported by [Rittgers et al. \(2014\)](#). However, given that large sand boils were already visible, before the positive SP anomaly at the downstream toe of the dike became visible, an SP monitoring system would not be useful as an early warning system. Furthermore, the growth of a pipe is not expected to be visible with SP monitoring, because changes in the SP field, due to growth of a pipe, are expected to be too small relative to the signal strength of flow through the sand boil and relative to the sensitivity of an SP monitoring system.

Even though an integrated long term ERT and SP monitoring system would not be able to track the growth of a backward erosion pipe, such a system could provide valuable information about a dike. A good example of an ERT monitoring system is the Proactive Infrastructure Monitoring and Evaluation (PRIME) system, developed by [Chambers et al. \(2019\)](#), who is keen on research collaboration. The PRIME system was specifically designed for long term resistivity monitoring and combines low cost, solar powered instrumentation with automated data processing. The employed inversion algorithm jointly inverts for the medium resistivity as well as for the electrode position. The accuracy of the electrode position is claimed to lie within 10% of the electrode spacing ([Boyle et al., 2018](#); [Wilkinson et al., 2016](#)). Jointly inverting for the electrode position is based on the principle that the geometric factors change as electrodes move, for example due to creep. One of the most recent developments in the PRIME system is directed towards integrating SP monitoring ([Sujitapan, Kendall, Whiteley, Chambers, & Uhlemann, 2019](#)), which promises to provide useful information about the hydrology of a dike.

Conclusions and recommendations

The principal aim of this master thesis was to assess the possibilities and limitations of monitoring backward erosion piping with time-lapse measurements of the self-potential at the surface of a dike. In order to answer this question, the expected SP response was modeled and field experiments were conducted on a test dike.

The SP in the test dike was modeled with the here developed FreeCAD → Gmsh → pyGIMLi workflow. Fluid flow and SP were modeled separately in two steps. First the fluid flow in the sand channel underneath the test dike was modeled under saturated conditions. Then the streaming current density resulting from this fluid flow, was interpolated on the SP mesh and the SP field was solved for. The results showed that both an accurate fluid flow and resistivity model are essential for correctly modeling the SP due to backward erosion piping. Hence, future research should be directed towards accurately modeling the change in flow field as the pipe grows and towards integrating Richard's equation for unsaturated flow. The latter because unsaturated flow in the core of the dike is expected to have a considerable impact on the total SP field.

All software in the workflow are free, open-source and under continuous development. Furthermore, the workflow is not only applicable to SP modeling. It allows for the meshing of practically any geometry, after which modeling and inversion of a wide range of standard and customizable geophysical methods is possible in pyGIMLi. Besides that, a geomatics workbench was recently developed for FreeCAD, through which GPS, topography and geospatial data can be loaded into FreeCAD. This could further simplify setting up inversion routines in pyGIMLi and possibly allow for constraining geophysical inversions based on geospatial data. As a last suggestion, there is a Gmsh plugin for QGIS that also looks promising for the integration of geophysical and geospatial data.

Field experiments during the preliminary and piping experiments pointed out that the proposed integrated ERT and SP monitoring system, with polarizable electrodes had several limitations. Firstly, drift of polarizable electrodes had a much larger impact on the measurements than expected. Secondly, compensating for this drift was not possible, given the large time variability and variability from one electrode to the other.

The reason that the polarizable electrodes show much larger drift than non-polarizable electrodes is, that there is direct contact between the metal of a polarizable electrode and the electrolytes in the soil. For both electrode types, the largest potentials are associated with the metal-electrolyte contact. The metal of non-polarizable electrodes is in contact with a solution with a constant concentration of its own salt. On the other hand, the electrolyte concentrations in the soil in the vicinity of the metal of a polarizable electrode are not stable. Hence, the potential measured fluctuates together with the soil electrolyte concentrations and thus the difference in stability between polarizable and non-polarizable electrodes. For future integrated ERT and SP monitoring systems, a combination of polarizable and non-polarizable electrodes should be used. Petiau Pb-PbCl₂ electrodes are recommended as non-polarizable electrodes, because these electrodes do not need servicing and have a smaller environmental impact compared to copper-copper(II) sulfate electrodes. The Petiau electrodes must not be used for current injection during ERT, but can be used to also measure the potential during ERT.

Piping was not visible in the SP data, also not on the data obtained with non-polarizable electrodes. That would most certainly also not have been the case, if more sensitive SP monitoring equipment had been used. This, because the flow rates during the piping experiment were no higher than 28 liter per hour. More generally, the hypothesis that SP monitoring can be used to track the growth of a backward erosion pipe is now considered too optimistic.

In a realistic case, an SP monitoring system would most likely not register SP anomalies before the flow rate is high enough to produce a large, visible sand boil. Hence, such a system would lose much of its value as a early warning system. Moreover, the change in SP signal associated with the growth of the pipe is expected to be overshadowed by the much larger positive SP anomaly around the sand boil. Also a well designed SP monitoring system is not expected to be sensitive enough to pick up these changes in the SP field.

Monitoring backward erosion piping does not look promising using an integrated ERT and SP monitoring system. However, such a system could provide valuable, real-time information about the condition of a dike. [Chambers et al. \(2019\)](#) developed a low cost, solar powered, long term ERT monitoring system, with automated data processing routines, called PRIME. Besides time-lapse resistivity data, the system also provides data about the movement of the electrodes to within 10% of the electrode spacing. One of the most recent developments in the PRIME system is directed towards integrating SP monitoring, which promises to provide useful information about the hydrology of a dike. For the further development of an integrated ERT and SP monitoring system for dikes, seeking research collaboration with J.E. Chambers is recommended and something he is looking for.

References

- Ayachit, U. (2015). *The paraview guide: A parallel visualization application*. United States: Kitware, Inc.
- Bersan, S., Jommi, C., Koelewijn, A., & Simonini, P. (2013). Applicability of the fracture flow interface to the analysis of piping in granular material. In *Proc., COMSOL Conference, Rotterdam, The Netherlands* (pp. 23–25).
- Bolève, A., Crespy, A., Revil, A., Janod, F., & Mattiuzzo, J. L. (2007). Streaming potentials of granular media: Influence of the Dukhin and Reynolds numbers. *Journal of Geophysical Research: Solid Earth*, *112*(B8). doi: 10.1029/2006JB004673
- Bolève, A., Revil, A., Janod, F., Mattiuzzo, J. L., & Fry, J.-J. (2009). Preferential fluid flow pathways in embankment dams imaged by self-potential tomography. *Near Surface Geophysics*, *7*(5-6), 447-462. doi: 10.3997/1873-0604.2009012
- Bolève, A., Vandemeulebrouck, J., & Grangeon, J. (2012, November). Dyke leakage localization and hydraulic permeability estimation through self-potential and hydro-acoustic measurements: Self-potential ‘abacus’ diagram for hydraulic permeability estimation and uncertainty computation. *Journal of Applied Geophysics*, *86*, 17-28. doi: 10.1016/j.jappgeo.2012.07.007
- Boyle, A., Wilkinson, P. B., Chambers, J. E., Meldrum, P. I., Uhlemann, S., & Adler, A. (2018, February). Jointly reconstructing ground motion and resistivity for ERT-based slope stability monitoring. *Geophysical Journal International*, *212*(2), 1167-1182. doi: 10.1093/gji/ggx453
- Brand, E., Baars, A., Verbruggen, E., & Lijzen, J. (2008). *Afleiding van milieurisicogrenzen voor sulfaat in oppervlaktewater, grondwater, bodem en waterbodem* (Tech. Rep. No. Briefrapport 711701069/2008). Bilthoven, Nederland: Rijksinstituut voor Volksgezondheid en Milieu. Retrieved from <https://www.rivm.nl/bibliotheek/rapporten/711701069.html>
- Chambers, J., Meldrum, P., Wilkinson, P., Kuras, O., Gunn, D., Uhlemann, S., ... Slater, N. (2019). Novel Low-Power Autonomous Ground Imaging Technology for Geohazard Monitoring, Information Delivery and Decision Support. In *81st EAGE Conference and Exhibition 2019*. Retrieved from <https://www.bgs.ac.uk/research/tomography/PRIME.html>

- Copper(II) Sulfate* — *Encyclopedia.com*. (2019, August). Retrieved 2019-10-05, from <https://www.encyclopedia.com/science/academic-and-educational-journals/copperii-sulfate>
- FreeCAD*. (2019, October). Retrieved from <https://www.freecadweb.org/> (Version: 0.18.0)
- Geuzaine, C., & Remacle, J.-F. (2009). Gmsh: A 3-D finite element mesh generator with built-in pre- and post-processing facilities. *International Journal for Numerical Methods in Engineering*, 79(11), 1309-1331. doi: 10.1002/nme.2579
- Glawdel, T., & Ren, C. L. (2015). Zeta Potential Measurement. In D. Li (Ed.), *Encyclopedia of Microfluidics and Nanofluidics* (p. 3513-3522). New York, NY: Springer. doi: 10.1007/978-1-4614-5491-5_1702
- Günther, T., Rücker, C., & Spitzer, K. (2006, August). Three-dimensional modelling and inversion of dc resistivity data incorporating topography — II. Inversion. *Geophysical Journal International*, 166(2), 506-517. doi: 10.1111/j.1365-246X.2006.03011.x
- Jardani, A., Revil, A., Bolève, A., Crespy, A., Dupont, J.-P., Barrash, W., & Malama, B. (2007). Tomography of the Darcy velocity from self-potential measurements. *Geophysical Research Letters*, 34(24). doi: 10.1029/2007GL031907
- Koelewijn, A. R., De Vries, G., Van Lottum, H., Förster, U., Van Beek, V. M., & Bezuijen, A. (2014). Full-scale testing of piping prevention measures: Three tests at the Ijkdijk. In *8th International Conference on Physical modelling in Geotechnics, Proceedings* (Vol. 2, p. 891-897). CRC Press - Taylor and Francis Group. Retrieved from <http://hdl.handle.net/1854/LU-4243606>
- Martinsen, O. G., & Grimnes, S. (2011). *Bioimpedance and bioelectricity basics* (Second ed.). Oxford, United Kingdom: Academic press.
- Minsley, B. J. (2007). *Modeling and inversion of self-potential data* (Thesis, Massachusetts Institute of Technology, Boston). Retrieved from <https://dspace.mit.edu/handle/1721.1/40863>
- Neuman, M. R. (2000). *The Biomedical Engineering Handbook, Chapter 48: Biopotential Electrodes* (Second ed.). Boca Raton, Florida: CRC Press.
- Petiau, G. (2000, March). Second Generation of Lead-lead Chloride Electrodes for Geophysical Applications. *pure and applied geophysics*, 157(3), 357-382. doi: 10.1007/s000240050004
- Petiau, G., & Dupis, A. (1980). Noise, Temperature Coefficient, and Long Time Stability of Electrodes for Telluric Observations. *Geophysical Prospecting*, 28(5), 792-804. doi: 10.1111/j.1365-2478.1980.tb01261.x
- Pol, J. C., Kanning, W., & Jonkman, S. N. (2019). Temporal development of backward erosion piping in a large scale experiment. *Manuscript submitted for publication*.
- Revil, A., & Jardani, A. (2013). *The Self-Potential Method: Theory and Applications in Environmental Geosciences*. New York, NY: Cambridge University Press. Retrieved from <http://ebookcentral.proquest.com/lib/delft/detail.action?docID=1357341>
- Rittgers, J. B., Revil, A., Planes, T., Mooney, M. A., & Koelewijn, A. R. (2014, December). 4-D imaging of seepage in earthen embankments with time-lapse inversion of self-potential data constrained by acoustic emissions localization. *Geophysical Journal International*, 200(2), 758-772. doi: 10.1093/gji/ggu432
- Robbins, B., & van Beek, V. (2015, September). Backward Erosion Piping: A Historical Review and Discussion of Influential Factors. In *ASDSO Dam Safety Conference*. New Orleans, Louisiana, United States.

- Rücker, C., Günther, T., & Spitzer, K. (2006). Three-dimensional modelling and inversion of dc resistivity data incorporating topography – I. Modelling. *Geophysical Journal International*, 166(2), 495-505. doi: 10.1111/j.1365-246X.2006.03010.x
- Rücker, C., Günther, T., & Wagner, F. M. (2017, December). pyGIMLi: An open-source library for modelling and inversion in geophysics. *Computers & Geosciences*, 109, 106-123. doi: 10.1016/j.cageo.2017.07.011
- Sellmeijer, H., de la Cruz, J. L., van Beek, V. M., & Knoeff, H. (2011). Fine-tuning of the backward erosion piping model through small-scale, medium-scale and IJkdijk experiments. *European Journal of Environmental and Civil Engineering*, 15(8), 1139–1154.
- Sellmeijer, J. B. (1988). *On the mechanism of piping under impervious structures* (Doctoral dissertation, Delft University of Technology, Delft). Retrieved from <https://repository.tudelft.nl/islandora/object/uuid%3A7f3c5919-1b37-4de9-a552-1f6e900eeaad>
- Sill, W. R. (1983, January). Self-potential modeling from primary flows. *GEOPHYSICS*, 48(1), 76-86. doi: 10.1190/1.1441409
- Soueid Ahmed, A., Revil, A., Steck, B., Vergniault, C., Jardani, A., & Vincelas, G. (2019, April). Self-potential signals associated with localized leaks in embankment dams and dikes. *Engineering Geology*, 253, 229-239. doi: 10.1016/j.enggeo.2019.03.019
- Sujitapan, C., Kendall, M., Whiteley, J. S., Chambers, J. E., & Uhlemann, S. (2019). Landslide Investigation and Monitoring Using Self-Potential Methods. In *25th European Meeting of Environmental and Engineering Geophysics*.
- Uddin, M. K. (2017, January). A review on the adsorption of heavy metals by clay minerals, with special focus on the past decade. *Chemical Engineering Journal*, 308, 438-462. doi: 10.1016/j.cej.2016.09.029
- Van Beek, V. M. (2015). *Backward erosion piping: Initiation and progression* (Thesis, Delft University of Technology, Delft). Retrieved from <http://resolver.tudelft.nl/uuid:4b3ff166-b487-4f55-a710-2a2e00307311>
- Van Dam, P., & Beijersbergen, J. A. (1981). Dijkdoorbraak Zalk: 8 januari 1926. *Centrum Onderzoek Waterkeringen, Publication: S 80.056a*. Retrieved from <http://resolver.tudelft.nl/uuid:93ce054b-fd68-4920-a0f4-080743483903>
- Vandenboer, K., van Beek, V., & Bezuijen, A. (2014, June). 3D finite element method (FEM) simulation of groundwater flow during backward erosion piping. *Frontiers of Structural and Civil Engineering*, 8(2), 160-166. doi: 10.1007/s11709-014-0257-7
- Verweij, W., Boumans, L., Claessens, J., & Lijzen, J. (2017). *Achtergrondconcentraties en kwaliteitscriteria grondwater; gegevens voor antimoon, arseen, barium, cadmium, chroom, kobalt, koper, kwik, lood, molybdeen, nikkel en zink*. (Tech. Rep. No. RIVM Briefrapport 2017-0125). Bilthoven, Nederland: Rijksinstituut voor Volksgezondheid en Milieu.
- VNK. (2014). *De veiligheid van Nederland in kaart: Eindrapportage VNK* (Tech. Rep. Nos. Eindverslag, Document HB2540621). Utrecht, Nederland: Rijkswaterstaat. Retrieved from <https://repository.tudelft.nl/islandora/object/uuid%3A52035faa-43ab-4dd0-a5b0-099119085356>
- Vrijling, J. K., Kok, M., Calle, E., Epema, W., Van der Meer, M., Van den Berg, P., & Schweckendiek, T. (2010). *Piping: Realiteit of Rekenfout?* (Tech. Rep. No. 2040048). Lelystad, Nederland: Expertisenetwerk Waterveiligheid (ENW). Retrieved from <https://repository.tudelft.nl/islandora/object/uuid%3Af5b79879-f4d2-4fce-9b11-38547db4509f>

- Wilkinson, P., Chambers, J., Uhlemann, S., Meldrum, P., Smith, A., Dixon, N., & Loke, M. H. (2016). Reconstruction of landslide movements by inversion of 4-D electrical resistivity tomography monitoring data. *Geophysical Research Letters*, *43*(3), 1166-1174. doi: 10.1002/2015GL067494

Appendix A

Complementary figures and tables

A-1 Theoretical background

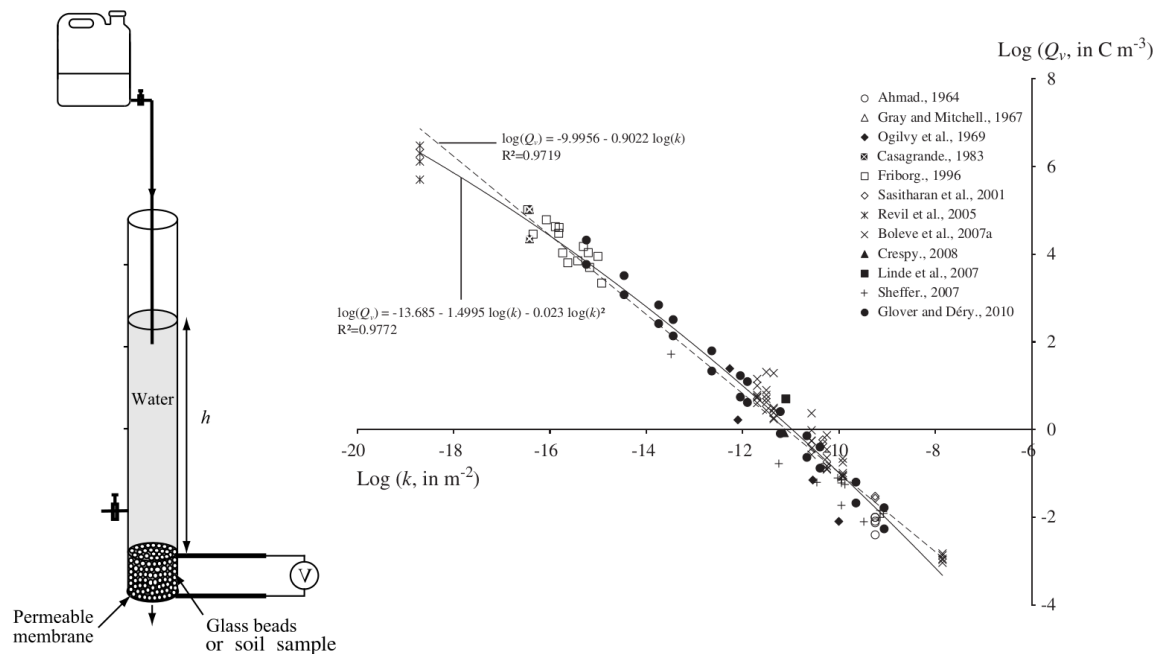


Figure A-1: Experimental setup (left) used to determine the empirical relationship between excess charge in the diffuse layer per unit volume (Q_v [Coulomb/m³]) and hydraulic permeability (k [m⁻²]). The sample was put at the bottom of a Plexiglas tube, with a permeable bottom. The SP was measured using two Ag-AgCl non-polarizable electrodes and a high impedance voltmeter. Sources: Bol ve et al. (2007, 2012)

Forces

		Electric gradient	Hydraulic gradient	Chemical gradient	Temperature gradient
Fluxes	Electric	Ohm's Law	Streaming current	Electro-diffusion	Seebeck effect
	Fluid	Electro-osmosis	Darcy's Law	Chemico-osmosis	Thermo-osmosis
	Solute	Electrophoresis	Ultrafiltration	Fick's Law	Soret effect
	Heat	Peltier effect	Thermal filtration	Dufour effect	Fourier's Law

Figure A-2: Coupling mechanisms between electric, hydraulic, solute diffusion and heat fluxes, driven by the corresponding gradients. Source: Minsley (2007)

A-2 Fieldwork

Parameter	Units	Fine	Coarse
		μ (σ , N)	μ (σ , N)
d_{10}	μm	127 (3,3)	190 (-)
d_{50}	μm	185 (9,3)	400 (-)
d_{60}	μm	201 (3,3)	450 (-)
d_{70}	μm	223 (15,3)	500 (-)
ρ_s	kg/m^3	2580 (52,9)	-
n	-	0.383 (0.005,4)	-
n_{min}	-	0.369 (-)	-
n_{max}	-	0.467 (-)	-
κ_{lab}	m^2	$1.2 \cdot 10^{-11}$ ($5.6 \cdot 10^{-12}$, 6)	$4.1 \cdot 10^{-11}$ ($8.3 \cdot 10^{-13}$, 3)
k_{lab} at $5^\circ C$	m/s	$8.0 \cdot 10^{-5}$ ($3.6 \cdot 10^{-5}$, 6)	$2.6 \cdot 10^{-4}$ ($5.4 \cdot 10^{-6}$, 3)
k_{dike}	m/s	$9 \cdot 10^{-5}$	-
C_u	-	1.59 (0.01,3)	2.4 (-)
D_r	-	0.854	-

Table A-1: Properties of the fine and coarse sand used in the sand channels underneath the test dike. Source: Pol et al. (2019)

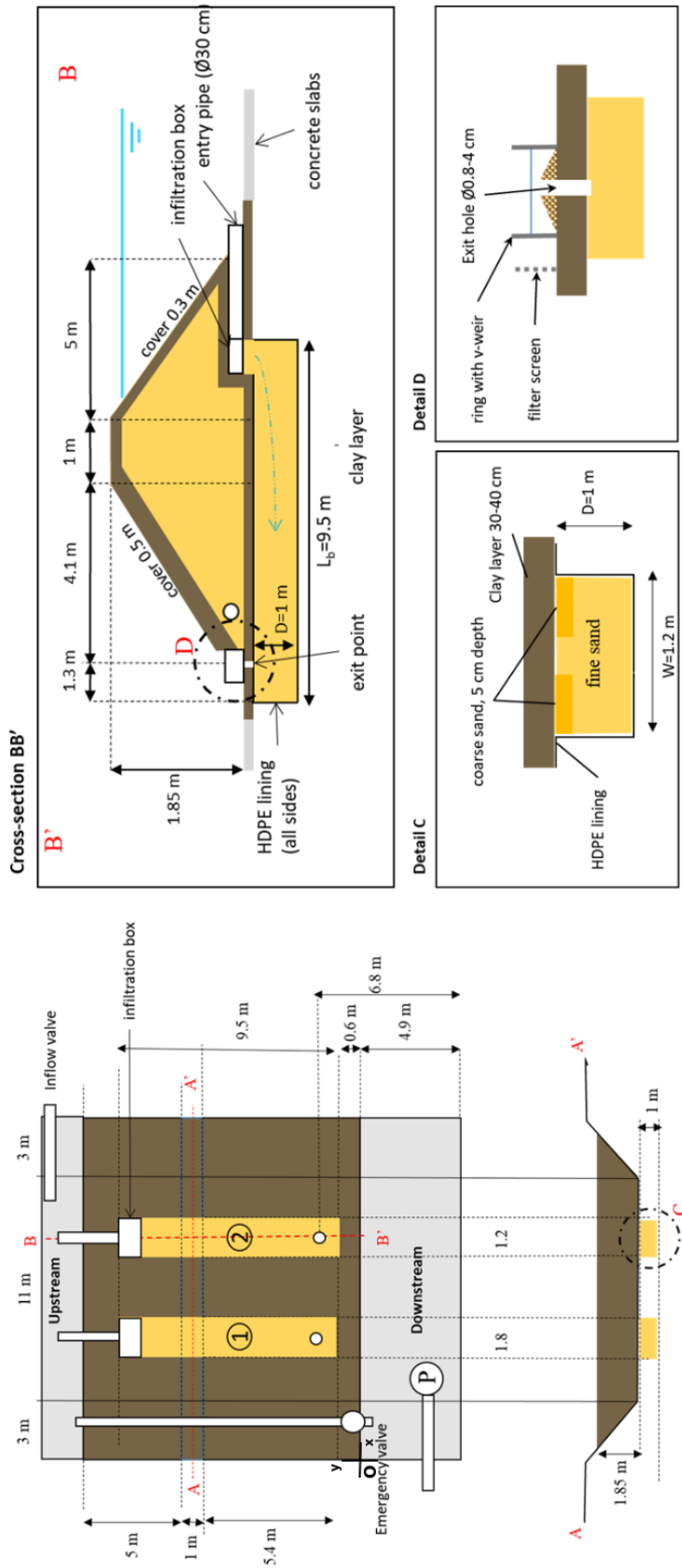


Figure A-3: Schematic drawing of the test dike. Note that the drawings are not to scale and that cross section BB' is a view in negative x direction. Source: Pol et al. (2019)

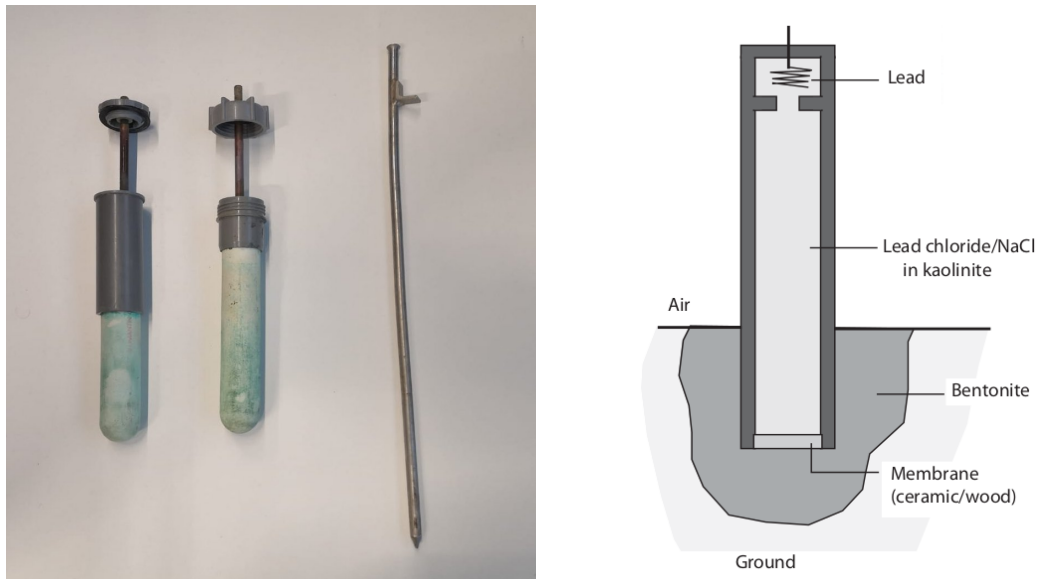


Figure A-4: Left: the 2 non-polarizable copper-copper(II) sulfate electrodes and one of the polarizable stainless steel electrodes used in the field. The non-polarizable electrodes are a porous pot with a screw cap to which a copper rod is attached. The rod is submerged in a CuSO_4 solution in the porous pot. Right: Schematic of Petiau electrode placed in the ground using bentonite to ensure good coupling. Source: [Revil and Jardani \(2013, chap. 1\)](#)



Figure A-5: Photo of upstream side of the dike. ERT measurements of lines 4 and 5 prior to the piping experiment.

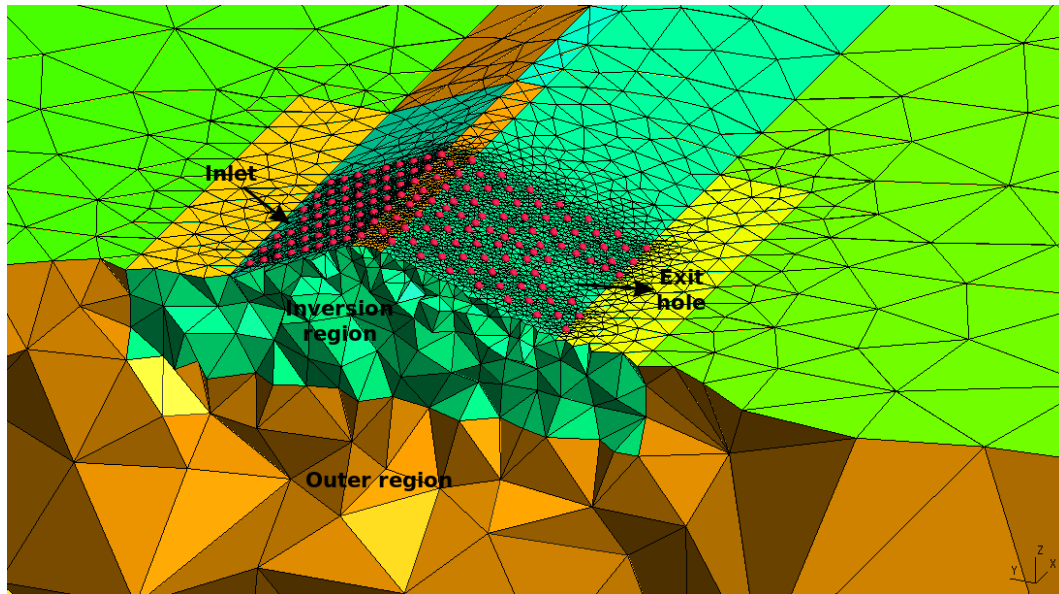


Figure A-6: Mesh used for the inversion of piping experiment ERT data. Red dots indicate electrode positions. The mesh is finer at the electrodes and inversion region and becomes very coarse towards the edge of the outer region. Dimensions of inversion region: 20 m longitudinal length and 3 m wide and deep from the toes of the dike.

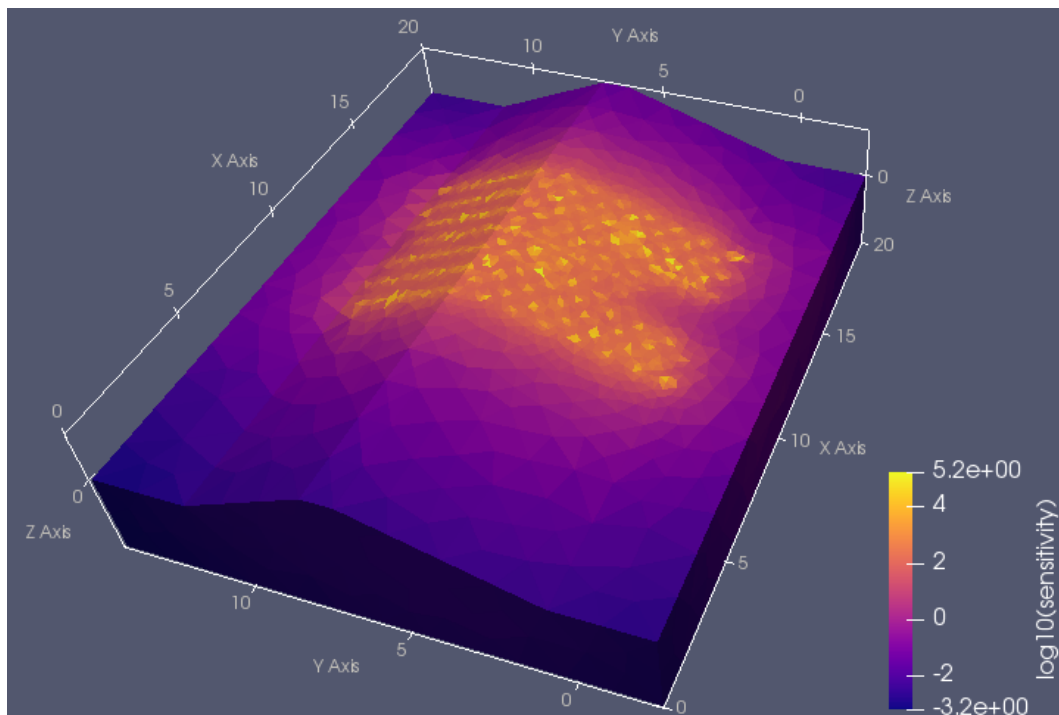


Figure A-7: 3D cumulative sensitivity distribution of the inversion of dipole-dipole data obtained prior to the piping experiment.

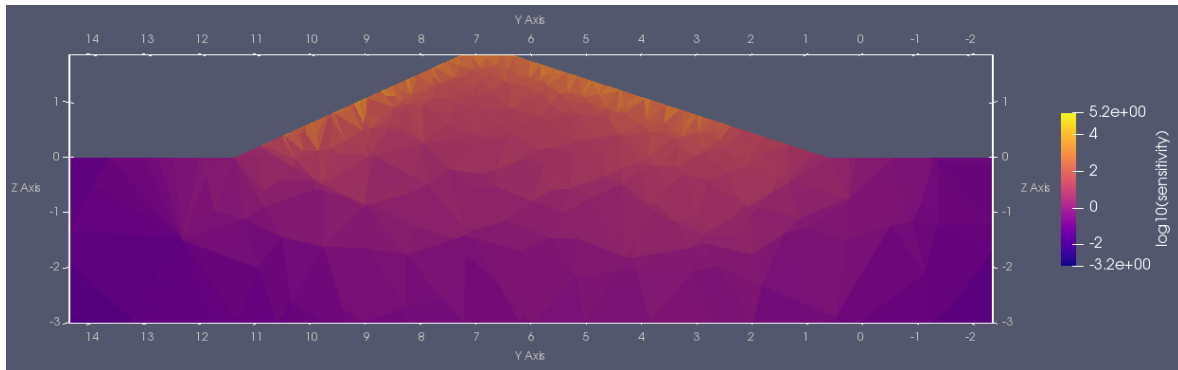


Figure A-8: Slice through the cumulative sensitivity distribution of the ERT inversion of dipole-dipole data obtained prior to the piping experiment. Slice through the exit hole at $x = 11.5$ m.

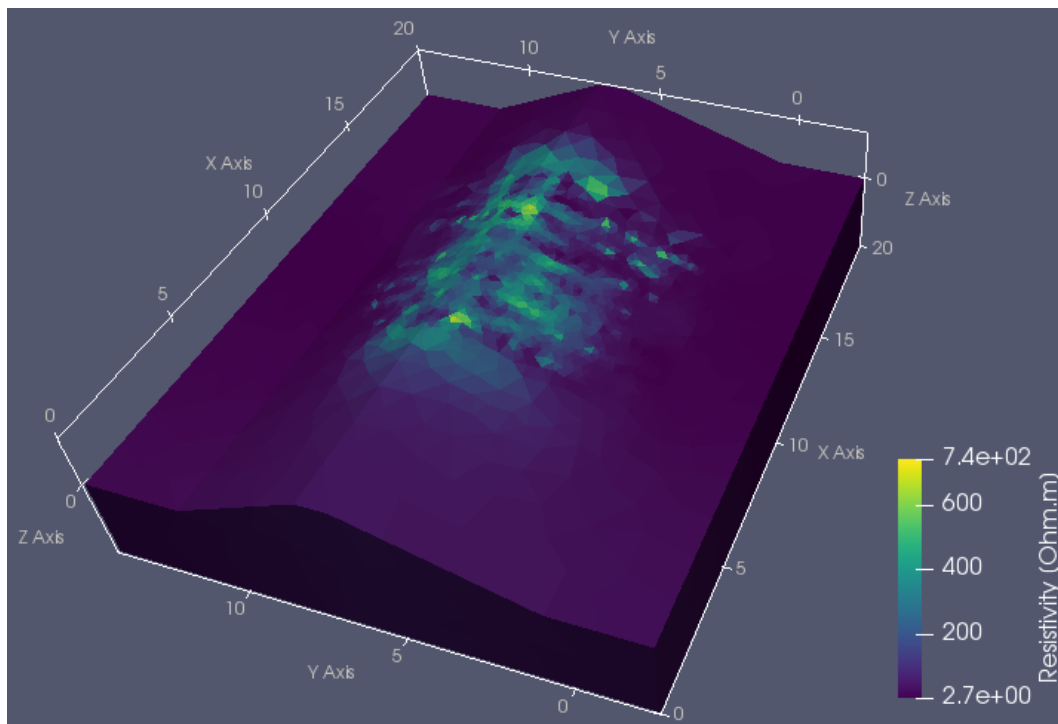


Figure A-9: 3D resistivity model obtained through simultaneous inversion of dipole-dipole and Wenner-Slumberger data obtained during the preliminary fieldwork. 2 step inversion parameters and statistics: (a) L1-norm inversion with an upper bound on the resistivity of $600 \Omega\text{m}$. 20 iterations; RMS = 84.2%; $\chi^2 = 2.81$ (b) L2-norm inversion with the L1-norm inversion result as starting model; a decrease in regularization strength of 0.8 at every iteration and an upper bound on the resistivity of $1100 \Omega\text{m}$. 4 iterations; RMS = 72.2%; $\chi^2 = 132$.

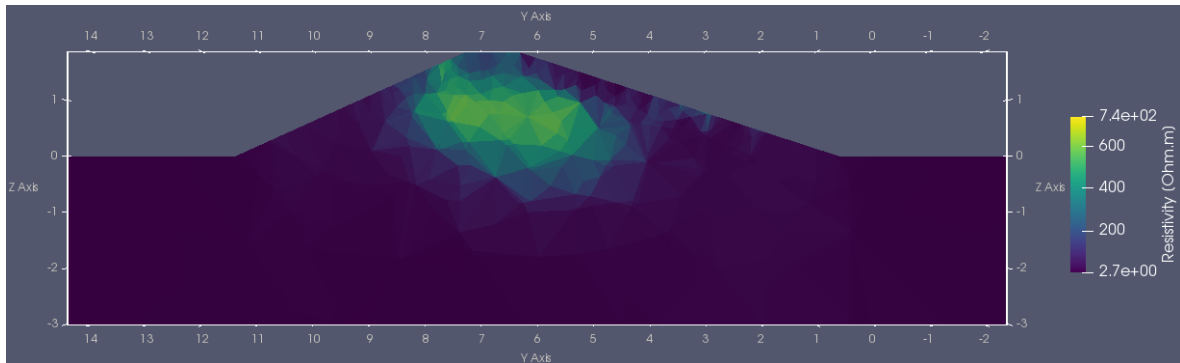


Figure A-10: Slice through the resistivity model that was the outcome of the inversion of ERT data obtained during the preliminary fieldwork. Slice through the exit hole at $x = 11.5$ m.

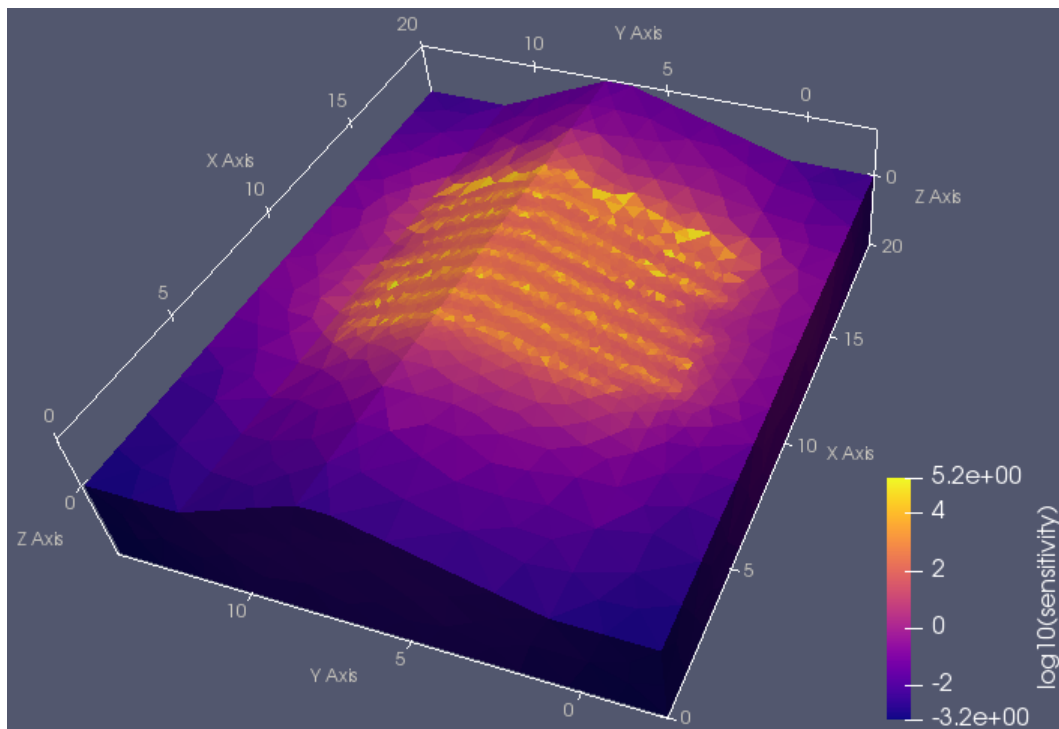


Figure A-11: 3D cumulative sensitivity distribution of the simultaneous inversion of dipole-dipole and Wenner-Slumberger data obtained during the preliminary fieldwork.

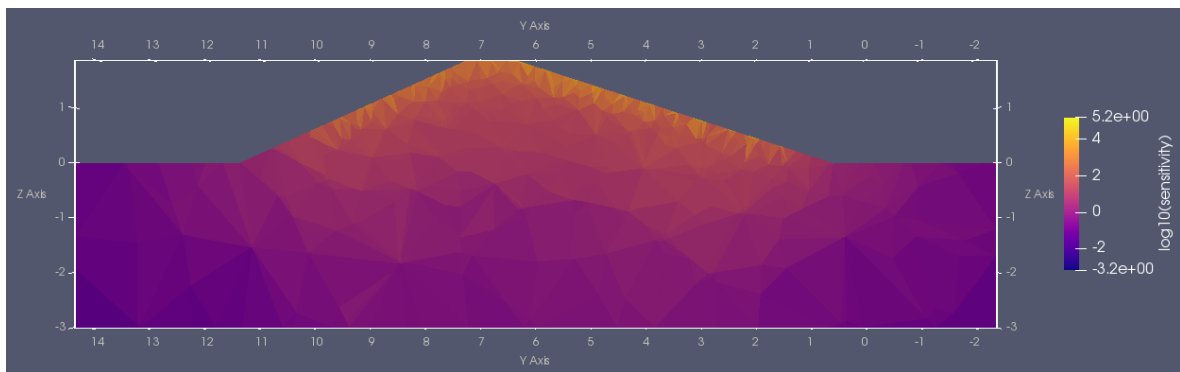


Figure A-12: Slice through the cumulative sensitivity distribution of the ERT inversion of dipole-dipole data obtained prior to the piping experiment. Slice through the exit hole at $x = 11.5$ m.

Appendix B

Copper(II) sulfate environmental impact calculations

Region of influence, a cylinder with: radius, $r = 5$ m; height, $h = 2$ m; water content, $\theta = 40$ %; volume of water considered, V_w :

$$\begin{aligned} V_w &= \pi r^2 h \theta \\ V_w &= \pi 5^2 * 2 * 0.40 \approx 63 \text{ m}^3 \end{aligned} \quad (\text{B-1})$$

Mass concentration (ρ_i [g/l]) of Cu^{2+} and SO_4^{2-} in the 350 g/l copper(II) sulfate pentahydrate ($\text{CuSO}_4 \cdot 5 \text{H}_2\text{O}$) electrolyte solution:

$$\begin{aligned} c_{\text{CuSO}_4 \cdot 5 \text{H}_2\text{O}} &= \frac{\rho_{\text{CuSO}_4 \cdot 5 \text{H}_2\text{O}}}{M_{\text{Cu}} + M_{\text{S}} + 9M_{\text{O}} + 10M_{\text{H}}} \\ c_{\text{CuSO}_4 \cdot 5 \text{H}_2\text{O}} &\approx \frac{350}{63.5 + 32.1 + 9 * 16.0 + 10 * 1.01} \approx 1.4 \text{ mol/l} \end{aligned} \quad (\text{B-2})$$

$$\begin{aligned} \rho_{\text{Cu}^{2+}\text{electrolyte}} &= c_{\text{CuSO}_4 \cdot 5 \text{H}_2\text{O}} * M_{\text{Cu}} \\ \rho_{\text{Cu}^{2+}\text{electrolyte}} &\approx 1.40 * 63.5 = 89 \text{ g/l} \end{aligned} \quad (\text{B-3})$$

$$\begin{aligned} \rho_{\text{SO}_4^{2-}\text{electrolyte}} &= c_{\text{CuSO}_4 \cdot 5 \text{H}_2\text{O}} * (M_{\text{S}} + 4M_{\text{O}}) \\ \rho_{\text{SO}_4^{2-}\text{electrolyte}} &\approx 1.40 * (32.1 + 4 * 16.0) \approx 135 \text{ g/l} \end{aligned} \quad (\text{B-4})$$

where M_i is the molar mass and c_i is the molar concentration of a chemical species i . 3*70 ml copper(II) sulfate leaked out of the electrodes. Mass (m_i [g]) of Cu^{2+} and SO_4^{2-} that leaked out of the copper-copper(II) sulfate electrodes:

$$\begin{aligned} m_{\text{Cu}^{2+}\text{electrolyte}} &= \rho_{\text{Cu}^{2+}} * V_{\text{CuSO}_4} \\ m_{\text{Cu}^{2+}\text{electrolyte}} &\approx 89.0 * 0.21 \approx 19 \text{ g} \end{aligned} \quad (\text{B-5})$$

$$\begin{aligned} m_{\text{SO}_4^{2-}\text{electrolyte}} &= \rho_{\text{SO}_4^{2-}} * V_{\text{CuSO}_4} \\ m_{\text{SO}_4^{2-}\text{electrolyte}} &\approx 135 * 0.21 \approx 28 \text{ g} \end{aligned} \quad (\text{B-6})$$

Mass of Cu^{2+} and SO_4^{2-} that were already present in the considered region, based on the background concentrations of $\rho_{\text{Cu}^{2+}} = 8.8 \mu\text{g/l}$ and $\rho_{\text{SO}_4^{2-}} = 20 \text{mg/l}$ (Brand et al., 2008; Verweij et al., 2017):

$$\begin{aligned} m_{\text{Cu}^{2+}\text{background}} &= \rho_{\text{Cu}^{2+}} * V_w \\ m_{\text{Cu}^{2+}\text{background}} &\approx 8.8 \times 10^{-6} * 63 \times 10^3 \approx 0.55 \text{ g} \end{aligned} \quad (\text{B-7})$$

$$\begin{aligned} m_{\text{SO}_4^{2-}\text{background}} &= \rho_{\text{SO}_4^{2-}} * V_w \\ m_{\text{SO}_4^{2-}\text{background}} &\approx 2.0 \times 10^{-2} * 63 \times 10^3 \approx 950 \text{ g} \end{aligned} \quad (\text{B-8})$$

New mass concentration of Cu^{2+} and SO_4^{2-} in the considered volume and percentage change in mass concentrations:

$$\begin{aligned} \rho_{\text{Cu}^{2+}} &= \frac{m_{\text{Cu}^{2+}\text{background}} + m_{\text{Cu}^{2+}\text{electrolyte}}}{V_w} \\ \rho_{\text{Cu}^{2+}} &\approx \frac{0.55 + 19}{63 \times 10^3} \approx 3.1 \times 10^{-4} \text{ g/l} = 310 \mu\text{g/l} \\ &\approx 3400 \% \text{ increase in } \text{Cu}^{2+} \text{ concentration} \end{aligned} \quad (\text{B-9})$$

$$\begin{aligned} \rho_{\text{SO}_4^{2-}} &= \frac{m_{\text{SO}_4^{2-}\text{background}} + m_{\text{SO}_4^{2-}\text{electrolyte}}}{V_w} \\ \rho_{\text{SO}_4^{2-}} &\approx \frac{950 + 28}{63 \times 10^3} \approx 1.54 \times 10^{-2} \text{ g/l} = 15.4 \text{ mg/l} \\ &\approx 2.7 \% \text{ increase in } \text{SO}_4^{2-} \text{ concentration} \end{aligned} \quad (\text{B-10})$$

Appendix C

FreeCAD; Gmsh; pyGIMLi workflow

This is a short electrical resistivity tomography (ERT) modeling and inversion example using a [FreeCAD](#) → [Gmsh](#) → [pyGIMLi](#) workflow. Gmsh provides a build-in CAD engine, but defining a geometry in a parametric CAD program such as FreeCAD is much more intuitive and flexible. After defining the geometry in FreeCAD, a mesh is created with Gmsh. In Gmsh the mesh is locally refined in the inversion region and around the electrodes and region, boundary and electrode markers are assigned. The mesh is then loaded into pyGIMLi and subsequently ERT modeling and inversion are done in [BERT](#). In the 1.1 release of pyGIMLi, BERT will be integrated into pyGIMLi and this example will be included on pygimli.org, but for now ERT modeling and inversion are still done in pyBERT. Where pyBERT is the python implementation of BERT. Note that this is an ERT modeling and inversion example, but that this workflow can easily be translated to other geophysical methods as well.

This is an ERT modeling and inversion example on a small dike. The geometry and acquisition design come from the IDEA League master thesis of Joost Gevaert. The target in this example is to find the geometry of a sand channel underneath the dike. To keep the example simple, a homogeneous resistivity is assumed except for the sand channel, which has a higher resistivity. One mesh for ERT modeling is created, consisting of 3 regions; the outer region; the inner region (same as inversion region in this example) and the sand channel. A second mesh for ERT inversion, consisting of 2 regions; the outer region and the inversion region. When the same meshes are used for modeling and inversion, the geometry of the sand channel is already included in the structure of the mesh. Therefore the mesh itself would act as prior information to the inversion.

The files used for this example are included, so that you can do the example yourself. The following file formats can be found in the attached archive:

Table C-1: FreeCAD; Gmsh; pyGIMLi workflow file types

Extension	File type	Extension	File type
.FCStd	FreeCAD file	.geo	Gmsh script
.brep	Geometry file to be imported in Gmsh	.msh	Gmsh mesh file
.dat	BERT unified data format file	.bms	BERT mesh file
.vtk	Visualization Toolkit file	.py	Python script
.xlsx	Excel with electrode locations and ERT scheme		

C-1 FreeCAD

The first step is to design each region of the geometry separately in the part workbench, or in the part design workbench for more complicated geometries. To get familiar with the part design workbench, [this FreeCAD-tutorial](#) with some videos is great. When all objects, i.e. regions are defined, they have to be merged into one single "compsolid", i.e. composite solid. Meaning one object that consists of multiple solids that share the interfaces between the solids. Once this is done, the geometry can be exported. The geometry should be exported in .brep or .step format. .brep is preferred, as that is the native format of the OpenCascade CAD engine on which both FreeCAD and Gmsh run. .step is the standardized CAD exchange format and also works well. Gmsh can also read .iges files, but this format should be avoided. Development for the .iges format stopped after 1996 and geometries are not always imported correctly.

The outer region and inversion region of this dike example were created in the Part Design workbench, by making a sketch and then extruding it with the Pad option, see the Inversion-Region in the object tree in [Figure C-1](#). The sand channel is a simple cube, created in the Part workbench. The trick then lies in merging these shapes into a single compsolid. This is done in the following steps:

1. Open a new project and merge all objects, i.e. regions (File → Merge project...) into this project
2. In the Part workbench, select all objects and create Boolean Fragments (Part → Split → Boolean Fragments)
3. Select the newly created BooleanFragments in the object tree and change its Mode property to CompSolid, see [Figure C-1](#).
4. Keep BooleanFragments selected and then apply a Compound Filter to it (Part → Compound → Compound Filter)
5. Quality check the obtained geometry. Select the newly created CompoundFilter from the object tree and click Check Geometry (Part → Check Geometry). The SOLID: number, in the Shape Content, should match the number of objects merged when creating the Boolean Fragments, 3 in this example. COMPSOLID: should be 1 and the COMPOUND: should be 0, also for other geometries. COMPSOLID: 1 and COMPOUND: 0 indicates that the objects were indeed merged correctly to one single compsolid, see [Figure C-1](#).

6. Select the CompoundSolid from the object tree and export (File → Export...) as .brep.

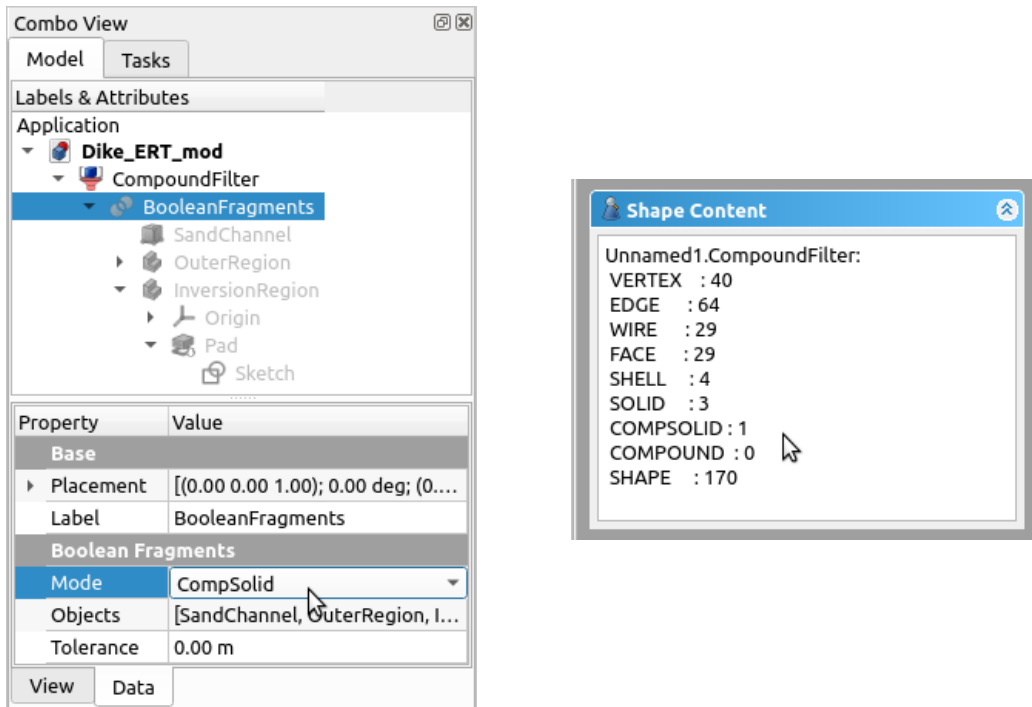


Figure C-1: Left: object tree of compsolid ERT modeling geometry. The compsolid was created by creating Boolean Fragments, in CompSolid Mode, from the SandChannel, OuterRegion and InversionRegion and then applying a Compound Filter. Right: Check Geometry of the compsolid. Important that the following match: SOLID: number of objects merged; COMPSOLID: 1; COMPOUND: 0.

C-2 Gmsh

Gmsh is incredibly versatile, but also has a very steep learning curve. Gmsh has several tutorials and demos, but lacks a clear overview on its website. [This website](#) does give a nice Gmsh tutorial overview, with pictures of the results and some additional examples.

It is easiest to work in Gmsh with both the Gmsh script and graphical user interface (GUI) open side by side. After making changes to the script, update the geometry in the GUI by pressing the Reload script button in the Geometry module. After changing something in the GUI, make sure to update the script.

Before diving into local mesh refinement, putting the electrodes in the mesh and assigning markers, the .brep geometry file should be checked. Import the geometry, change the units to [m], have a look at the geometry in the GUI and then mesh it in the GUI:

```

1 SetFactory("OpenCASCADE");
2 Merge "Dike_ERT_mod.brep"; // Import FreeCAD geometry
3 Geometry.OCCScaling = 0.001; // Scale geometry from [mm] to [m]

```

Mesh the geometry by subsequently clicking 1D, 2D and 3D in the Mesh module. Check if the geometry was meshed without errors and that the mesh makes sense. Especially check

whether the meshes of two adjacent regions share nodes on their interfaces. Tips for viewing the mesh:

1. Double left clicking opens a menu in where you can set geometry and mesh visibility.
2. Tools → Visibility opens a window in which you can select parts of the mesh and geometry. Also handy later to QC whether physical groups were set correctly.
3. Clip the mesh and geometry with Tools → Clipping.
4. The number of elements ect. can be found in the Tools → Statistics window.

If importing and meshing the .brep geometry went correctly, great! Next define the Characteristic Length (CL) for each region and the electrodes:

```

4 // Define characteristic lengths
5 cl_elec = 0.1;    cl_dike = 0.6;    cl_outer = 30;
6 // Volume 1: sand channel, Volume 2: outer region, Volume 3: inner region
7 Characteristic Length { PointsOf{ Volume{2}; } } = cl_outer;
8 Characteristic Length { PointsOf{ Volume{3}; } } = cl_dike;
9 Characteristic Length { PointsOf{ Volume{1}; } } = cl_dike;

```

The CL is defined at each point and dictates the mesh size at that point. When setting the CL, make sure to think about the order (lines 7-9 set CL from big to small), because the CL is overwritten in shared points. Now reload the script, mesh the geometry again and have a look how the mesh changed.

The next step is adding the electrodes to the mesh. The few lines of python code below read the electrode positions from an Excel data sheet and write them into a Gmsh .geo file. The grid on the dike has 152 electrodes. These points are added in Gmsh as points 201-352, to prevent clashing with points already defined in the geometry.

```

1 import pandas as pd
2 filename = 'ERT_pos_and_scheme.xlsx'
3 elec_depth = 0.02    # elec depth [m]
4 # Load electrode positions from Excel
5 pos = pd.read_excel(filename, sheet_name='elec_pos')
6 pos['z'] = pos['z'] - elec_depth
7 # Write to Gmsh .geo file
8 id = int(200)        # Gmsh point ID, high number to prevent clash with
                      # other points
9 gmsh_grid = open('gmsh_elec_pos.geo', 'w')
10 for i, xyz in pos.iterrows():
11     gmsh_grid.write('Point(%d) = {%.3f, %.3f, %.3f, cl_elec};\n'
12                    % ((xyz['elec #'] + id), xyz['x'], xyz['y'], xyz['z']))
13 gmsh_grid.close()

```

Copy and paste the electrode positions from `gmsh_elec_pos.geo` to the Gmsh script with the geometry and include the newly added points in the volume of the dike body:

```

10 Point(201) = {8.500, 0.600, -0.020, cl_elec};
11 ...
12 Point(352) = {14.500, 10.954, 0.186, cl_elec};
13 // Include electrodes in the correct geometric volume
14 Point{201:352} In Volume{3};

```

Reload the Gmsh script and mesh it again to see the result. Further mesh refinement is then possible with so-called background fields. Taking a quick look at Gmsh tutorial [t10.geo](#) is

highly recommended. It shows a wide range of possible background fields. In this example a Distance field is defined from the electrodes and then a Threshold field is applied as the background field:

```

15 // Define a background field that further refines mesh size.
16 // LcMax - /-----
17 // /
18 // /
19 // LcMin -o-----/
20 // | | |
21 // Point DistMin DistMax
22 Field[1] = Distance; Field[1].NodesList = {201:352};
23 Field[2] = Threshold; Field[2].IField = 1;
24 Field[2].LcMin = cl_elec; Field[2].LcMax = cl_dike;
25 Field[2].DistMin = 0.2; Field[2].DistMax = 1;
26 Field[2].Sigmoid = 0; Field[2].StopAtDistMax = 1;
27 Background Field = 2;

```

Again reload the Gmsh script and mesh it, to see the result. As the last step in creating the mesh, the physical groups have to be defined, such pyGIMLi and pyBERT recognize regions, boundaries and the electrodes. Defining can be done in the GUI or in the script. In the GUI in menu on the left: Modules → Geometry → Physical groups → Add. In either case it can be handy to use the Tools → Visibility window, to show and hide parts of the geometry. Make sure to follow the same naming conventions for marking the regions, surfaces and points. This to make sure that pyBERT correctly recognizes them. In the script it should look similar to:

```

28 // Boundaries: (1) Free Surface
29 Physical Surface(1) = {13, 12, 7, 9, 11, 21, 23, 24, 27, 25, 26, 28, 29};
30 // (2) Mixed Boundary Conditions: V = 0
31 Physical Surface(2) = {14, 20, 15, 8, 16};
32 // Regions
33 Physical Volume(2) = {1}; // Outer region
34 Physical Volume(1) = {2}; // Outer region
35 // Electrodes
36 Physical Point(99) = {201:352}; // Setting electrode marker

```

The final mesh should look something like [Figure C-2](#). Check whether the Physical groups are defined correctly using the Visibility window as shown in the figure. Then save the mesh in .msh format: File → Save Mesh. Finally make the inversion mesh in the same way as the modeling mesh. The differences being that (a) there should be no sand channel in the geometry of the inversion mesh. Meaning that there are also only 2 volumes, the outer region and the inner region, i.e. inversion region. And (b) that the mesh does not have to be as fine. `cl_elec = 0.25` and `cl_dike = 1.2` were used for the inversion mesh in the attached files. Besides changing the mesh size by playing around with the CL, the general mesh size can also be adapted in Gmsh by changing the Global mesh size factor (double left click).

C-3 pyGIMLi and pyBERT

When the mesh has the desired refinement and is saved in .msh format, it is time to set up ERT modeling and inversion. First an ERT file in [unified data format](#), which is the file format which tells BERT the electrode positions and quadruples, i.e. measurement scheme.

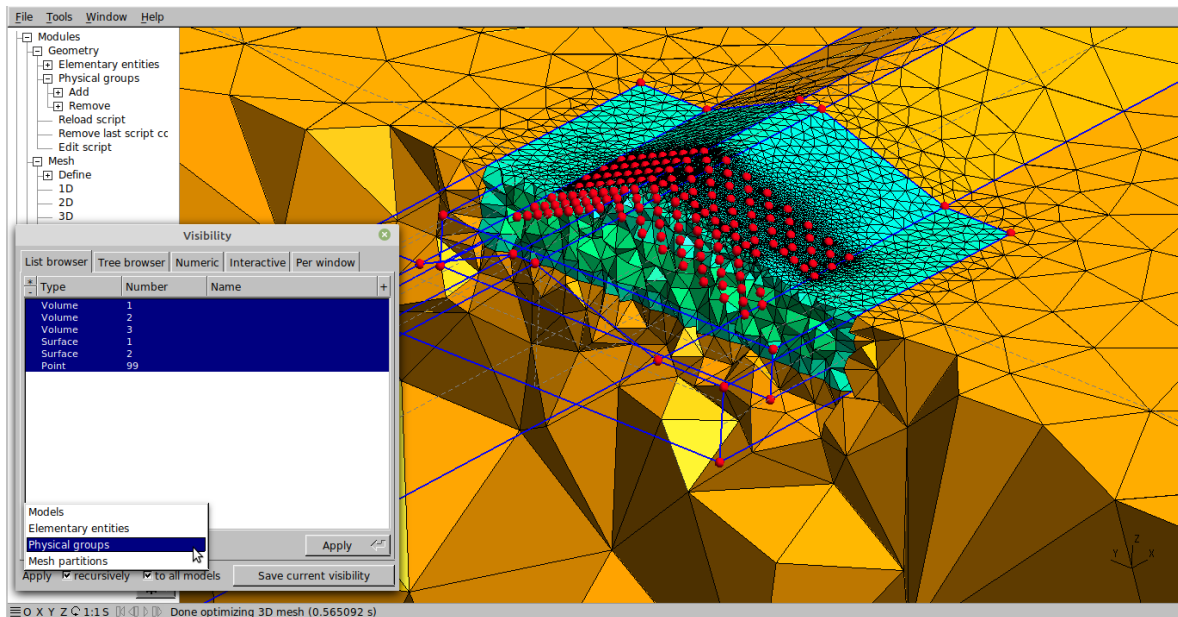


Figure C-2: ERT modeling mesh. Red dots are geometry points, as well as the electrode grid in the middle of the dike.

The quadruples used in this tutorial are dipole-dipole measurements in lines across the dike. The BERT file can be created by running:

```

14 # Write to BERT/pyGIMLi unified data format .dat file
15 ne = len(pos) # number of electrodes
16 scheme = pd.read_excel(filename, sheet_name='ERT_scheme')
17 BERT_dat = open('BERT.dat', 'w')
18 BERT_dat.write(f'{ne}\n' + '# x y z\n')
19 for i, xyz in pos.iterrows():
20     BERT_dat.write(f'%.3f %.3f %.3f\n' % (xyz['x'], xyz['y'], xyz['z']))
21 BERT_dat.write(f'{scheme.shape[0]}\n')
22 BERT_dat.write('# a b m n\n')
23 for i, abmn in scheme.iterrows():
24     BERT_dat.write('%d %d %d %d\n' % (abmn['A'], abmn['B'], abmn['M'], abmn[
25         'N']))
26 BERT_dat.write('0')
27 BERT_dat.close()

```

Subsequently running the lines of code below, creates another BERT file in unified data format. This time with apparent resistivities, that resulted from ERT modeling.

```

27 import pygimli.meshtools as mt
28 import pybert as pb
29 #Read Gmsh .msh model mesh and model ERT
30 msh_nm = 'Dike_ERT_mod'
31 mesh_mod = mt.readGmsh(msh_nm + ".msh", verbose=True)
32 # Read electrode positions and ERT scheme from BERT file
33 BERT = pb.importData('BERT.dat')
34 # Initiate pyBERT ERT object
35 ert = pb.ERTManager()
36 # Model ERT
37 rhomap = [[1, 10.], [2, 10.], [3, 300.]]

```

```

38 data_mod = ert.simulate(mesh_mod, res=rhomap, scheme=BERT)
39 data_mod.save('BERT_mod.dat')

```

The modeled data can then be inverted by running:

```

40 #Read Gmsh .msh
41 msh_nm = 'Dike_ERT_inv'
42 mesh_inv = mt.readGmsh(msh_nm + ".msh", verbose=True)
43 # Initiate pyBERT ERT object
44 ert = pb.ERTManager()
45 # Import the modeled data
46 data = pb.importData('BERT_mod.dat')
47 # Invert modeled data,
48 ert.invert(data, mesh=mesh_inv, lam=15)
49 # Write inversion outcome to .vtk to visualize in paraview
50 paradomain = ert.paradomain
51 paradomain.addData('Resistivity [Ohm.m]', ert.resistivity)
52 paradomain.addData('log10(sensitivity)', ert.coverageDC())
53 paradomain.exportVTK('invResult.vtk')

```

The inversion optimized the resistivity inside the inversion region. In BERT the inversion region is called the parameter domain. Lines 50-53 export the inversion result, so the resistivity model and sensitivity distribution inside the parameter domain, to a .vtk file. A .vtk file is a Visualization Toolkit file, which can be opened [ParaView](#), which is a flexible visualization toolkit. The resulting resistivity model, visualized in ParaView, looks like this:

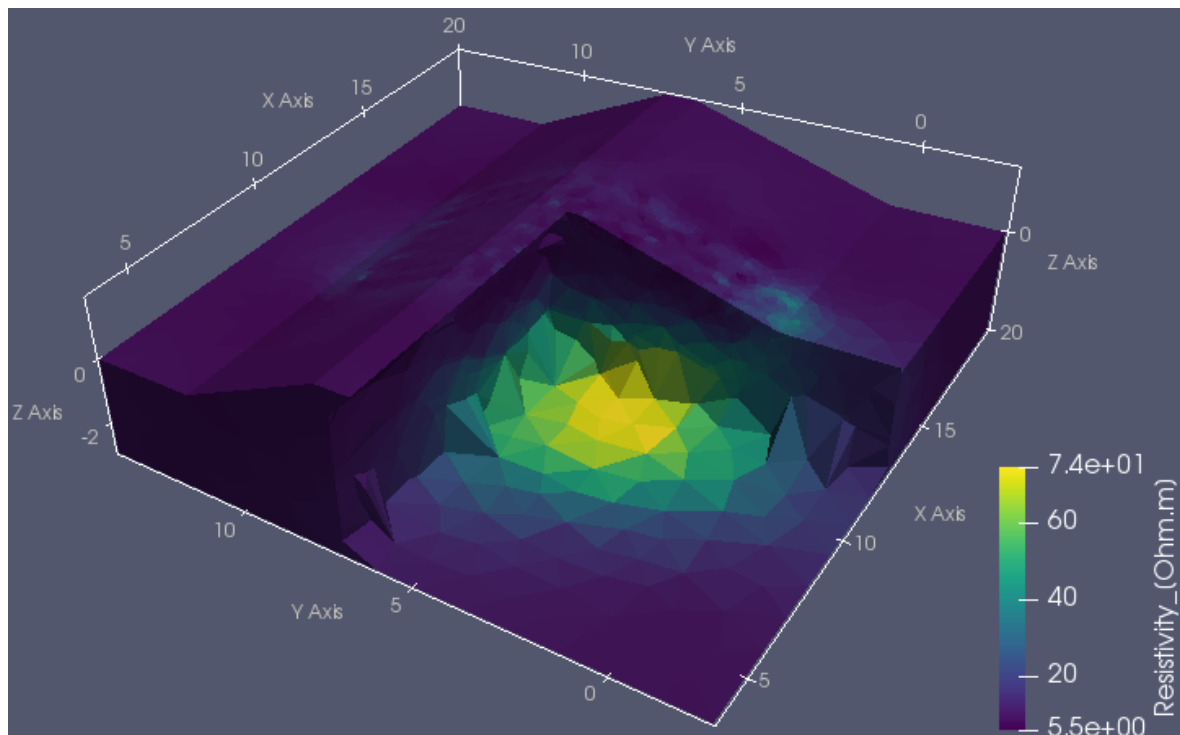


Figure C-3: Paraview visualization of the resistivity model that results from the inversion of the modeled ERT data.